# A Micropower Ultra-Wideband RADAR Profiling System

Yu-Ming Alvin Chang

A dissertation submitted to the Department of Electrical Engineering,
University of Cape Town, in fulfilment of the requirements
for the degree of Master of Science in Applied Science.

Cape Town, August 2006

# Declaration

I declare that this dissertation is my own, unaided work. It is being submitted for the degree of Master of Science in Applied Science in the University of Cape Town. It has not been submitted before for any degree or examination in any other university.

Signature of Author ..... Signed by candidate Signature Removed .....

Cape Town

31 August 2006

# Abstract

Ultra-wideband (UWB) technology can be used in many applications, including radar, communications, and geo-location. In this dissertation, UWB technology is utilized to directly generate sub-nanosecond pulses with more than 1 GHz bandwidth to implement radio detection and ranging (RADAR) for distances up to 5 or 10 metres.

This low-cost, micropower radiation, short-range radar profiling system consists of the radar circuitry, the data-acquisition subsystem, the signal processing subsystem and the graphical user interface. Additional modules such as a front-end RF amplifier can be integrated into the complete system. The performance was analysed, particularly the circuitry performance and system performance. The capability for detecting metal objects was demonstrated, along with discussion of preliminary *"seeing-through-wall"* experiments.

Thanking my parents

# Acknowledgments

This research would not have been possible without the financial assistance from the CSIR and the NRF. It also would not have been possible without the research facilities and equipments provided by the University. Foremost, it would not have been possible without the guidance and supervision from Dr. Andrew J. Wilkinson.

I thank you all.

# Contents

**Declaration** i

**Abstract** ii

**Acknowledgements** iv

**List of Symbols** xiv

**Nomenclature** xv

**1 Introduction** 1

1.1 Purposes . . . . . 1

1.2 Structure of The Thesis . . . . . 2

1.3 Literature Review . . . . . 3

1.3.1 UWB Technology for Radar . . . . . 3

1.3.2 Wideband Antennas Suitable for UWB Technology . . . . . 3

**2 Short Pulse UWB Principles and Implementation Architecture** 5

2.1 Conventional Pulse Radar . . . . . 5

2.2 Operation of UWB Radar . . . . . 6

2.3 Signal Model for an UWB Radar . . . . . 7

**3 Signal Processing** 12

3.1 Background Removal (Difference Imaging) . . . . . 12

3.2 Out-of-Band Signal Nulling . . . . . 12

3.3 Matched Filter (Correlator) . . . . . 12

3.4 Deconvolution Filter . . . . . 13

3.5 Window Functions . . . . . 13

**4 Circuits Simulation and Implementation** 16

4.1 PRF Signal Generator . . . . . 17

4.2 Transmitter . . . . . 17
4.3 Manual Delay Line and Fast Sampler-Averager . . . . . 21
4.4 Computer-Controlled Variable Delay Line and Fast Sampler-Averager . . 23
4.5 Post-Sampler Amplifier . . . . . 31

**5 System Integration** **34**
5.1 RADAR Circuit . . . . . 34
5.2 NI-DAQ Card . . . . . 35
5.3 Front-End RF Amplifier . . . . . 36
5.4 Antennas . . . . . 39
5.4.1 Bow-Tie Antennas . . . . . 39
5.4.2 Grid Antennas . . . . . 41

**6 Software System** **42**
6.1 Software Design . . . . . 42
6.2 Software Implementation . . . . . 42
6.2.1 Graphical User Interface . . . . . 42
6.2.2 Digital Signal Processing . . . . . 44
6.3 Software Operation . . . . . 45
6.3.1 Distance Conversion and an Example . . . . . 46

**7 Results and Performance** **50**
7.1 Achievable Pulse Bandwidth . . . . . 50
7.2 Limitations of Simple Antenna Structures . . . . . 50
7.3 Processed Bandwidth . . . . . 51
7.4 Peak Power Radiated . . . . . 51
7.4.1 Simulation . . . . . 51
7.4.2 Oscilloscope Measurement . . . . . 52
7.5 Averaged Power Radiated . . . . . 52
7.6 Limitation of Indoor Measurements . . . . . 53
7.7 Capability for Detecting Metal Objects . . . . . 53
7.7.1 Performance Without RF Amplifier . . . . . 55
7.7.2 Performance With RF Amplifier . . . . . 57
7.8 Detection through Obstacles . . . . . 57
7.8.1 Detection through Wooden Partition . . . . . 61
7.8.2 Detection through Cement Wall . . . . . 64
7.9 Noise Performance . . . . . 64
7.10 Achievable Maximum Sweeping Rate and Maximum Speed Detectable . 65

**8 Conclusions and Future Work** 67

**A Software Source Code** 68

**Bibliography** 71

# List of Figures


2.1 Block diagram of an elementary radar system, and some abbreviations commonly used [27]. . . . . 6

2.2 The UWB radar scheme[47]. . . . . 8

2.3 Operation of the "fast sampler" with a fixed delay. . . . . 8

2.4 UCT UWB radar scheme (Mono-static). . . . . 9

2.5 UCT UWB radar scheme (Bi-static). . . . . 9

3.1 Hanning window; $W[k+1] = 0.5\left(1 - \cos\left(2\pi\frac{k}{n-1}\right)\right), k = 0, \cdots, n-1$. 14

3.2 Hamming window; $W[k+1] = 0.54 - 0.46\cos\left(2\pi\frac{k}{n-1}\right), k = 0, \cdots, n-1$. . . . . 14

3.3 Blackman window; $W[k+1] = 0.42 - 0.5\cos\left(2\pi\frac{k}{n-1}\right) + 0.08\cos\left(4\pi\frac{k}{n-1}\right), k = 0, \cdots, n-1$. . . . . 15

4.1 Agilent Infinium 54833A DSO . . . . . 16

4.2 The noise modulated pulse generator used in [47, 30, 1]. . . . . 17

4.3 The simulated output voltage at node "out" (in Figure 4.2) is plotted as a function of time. The period is approximately 360 ns. . . . . 18

4.4 The measured output voltage at node "out" (in Figure 4.2) is plotted as a function of time. The period is approximately 420 ns.
Vertical (voltage) scale 1.00 V / Offset 2.46V.
Horizontal (time) scale 200 ns. . . . . 18

4.5 Noise generated from the left-half of the circuit shown in Figure 4.2. . . . 19

4.6 The measured noise generated from left-half of the circuit shown in Figure 4.2.
Vertical (voltage) scale 500 mV / Offset 1.629V.
Horizontal (time) scale 200 ns. . . . . 19

4.7 The transmitter used in [47]. . . . . 20

4.8 UCT UWB Radar Transmitter . . . . . 20

4.9 Equivalent SPICE circuit for a dipole antenna [17]. . . . . 21

4.10 The simulated waveform at node C4-R10-U5. . . . . 22

4.11 The measured waveform at C4-R10-U5 (lower waveform) with reference to the master clock (upper waveform).
Vertical (voltage) scale 2.0 V
Offset -1.47 V (master clock) / Offset 4.81 V (C4-R10-U5).
Horizontal (time) scale 200 ns. . . . . 22
4.12 Wave form at node C5-R11-Q4 feeding into the base of the transistor Q4. 23
4.13 Simulated pulse using 2N5109 transistor across 50Ω load. . . . . 24
4.14 The measured waveform generated by 2N5109.
Vertical (voltage) scale 500 mV / Offset 0.
Horizontal (time) scale 2 ns. . . . . 24
4.15 Simulated pulse using BFR91A transistor across 50Ω load. . . . . 25
4.16 The measured waveform generated by BFR91A.
Vertical (voltage) scale 500 mV / Offset 0.
Horizontal (time) scale 2 ns. . . . . 25
4.17 The measured waveform generated by BFR91A with DFT analysis beneath.
Vertical (voltage) scale 500 mV / Offset -379 mV.
DFT (wattage) scale 20 dBm / Offset -15 dBm.
Horizontal (time) scale 50 ns.
DFT (frequency) scale 200 MHz / Position 1 GHz. . . . . 26
4.18 The delay line and the fast sampler connected to a balanced dipole antenna used in [47]. . . . . 26
4.19 UCT UWB Radar Delay Line and Fast Sampler-Averager . . . . . 27
4.20 Reverse voltage v.s. capacitance of MV104. . . . . 28
4.21 Voltage vs. Delay . . . . . 28
4.22 Sub-circuits CIRCUIT1 and CIRCUIT2. . . . . 29
4.23 Thevenin equivalent circuits of CIRCUIT1 and CIRCUIT2. . . . . 29
4.24 Discharging circuits. . . . . 30
4.25 Thevenin equivalent circuits for the discharging circuits in Figure 4.24. . . 30
4.26 Post-Sampler Amplifier used in [47]. . . . . 31
4.27 UCT UWB Post-Sampler Amplifier . . . . . 32
4.28 Simplified Schematic of AD620 reproduced from [2]. . . . . 33

5.1 UCT UWB radar prototype (Mono-static) . . . . . 34
5.2 NI-DAQ . . . . . 35
5.3 Front-End RF Amplifier . . . . . 36
5.4 Two-Stage Amplification . . . . . 36
5.5 Gain vs Frequency Response
(Gain in dB) . . . . . 37

5.6 Noise Figure vs Frequency . . . . . 37
5.7 Gain vs Frequency Response (Gain in ratio) . . . . . 38
5.8 Noise Figure vs Frequency ($T_e$ in Kelvin) . . . . . 38
5.9 GPR Antenna (50 - 400 MHz) . . . . . 39
5.10 Twin-bowtie Antenna #1 (1 - 2 GHz) with a flare angle smaller than 40°made by [45]. . . . . 40
5.11 Twin-bowtie Antenna #2 (1 - 2 GHz) with a flare angle wider than 40°made by [45]. . . . . 40
5.12 Plot of measured gain vs. frequency of the twin-bowtie antenna with a flare angle smaller than 40°as measured by [45]. . . . . 40
5.13 Plot of measured gain vs. frequency of the twin-bowtie antenna with a flare angle wider than 40°as measured by [45]. . . . . 40

6.1 Software design. . . . . 43
6.2 Software Interface . . . . . 44
6.3 Background snapshot . . . . . 47
6.4 Echo from calibration target used to create deconvolution filter . . . . . 47
6.5 Unprocessed echo from a plate reflector . . . . . 48
6.6 Match filtered with no windowing applied . . . . . 48
6.7 Deconvolution filtered with no windowing applied . . . . . 49
6.8 Deconvolved and Hanning windowed . . . . . 49

7.1 Instantaneous power of the simulated waveform of Figure 4.15. . . . . 52
7.2 Instantaneous power across 50Ω of the pulse waveform captured in Figure 4.16. $P(t) = \frac{V(t)^2}{R}$. . . . . 53
7.3 Experiment Setup . . . . . 55
7.4 Target at 50cm without RF amplifier.X-axis: Sample (spans from -2.33m to 9.35m).Y-axis: Voltage (V). . . . . 56
7.5 Target at 80cm without RF amplifier.X-axis: Sample (spans from -2.33m to 9.35m).Y-axis: Voltage (V). . . . . 56
7.6 No Target with RF amplifier. . . . . 57
7.7 Target at 1.0m with RF amplifier. . . . . 58
7.8 Target at 1.5m with RF amplifier. . . . . 58
7.9 Target at 2.0m with RF amplifier. . . . . 59
7.10 Target at 2.5m with RF amplifier. . . . . 59
7.11 Target at 3.0m with RF amplifier. . . . . 60

7.12 Targets at 1.0m and 2.5m with RF amplifier. . . . . 60
7.13 Partition at 1.0m. . . . . 61
7.14 Target at 1.5m. (The partition located at 1.0m is not visible after background subtraction.) . . . . . 62
7.15 Target at 2.0m. (The partition located at 1.0m is not visible after background subtraction.) . . . . . 62
7.16 Target at 2.5m. (The partition located at 1.0m is not visible after background subtraction.) . . . . . 63
7.17 Target at 3.0m. (The partition located at 1.0m is not visible after background subtraction.) . . . . . 63

# List of Tables

5.1 Grid Antennas . . . . . 41

7.1 Metal Objects Tested . . . . . 54
7.2 Decrease due to the placement of the partition. . . . . 61
7.3 Signal-to-Noise ratio at different ranges. . . . . 64

# List of Symbols

| | | |
|---|---|---|
| $b(t)$ | — | Background snapshot |
| $B$ | — | Bandwidth-limited impulse |
| $c$ | — | Speed of light |
| $f_{max}$ | — | Maximum sweep rate |
| $f_{PRF}$ | — | Pulse repetition frequency |
| $f_c$ | — | Cut-off frequency |
| $f_H$ | — | Highest frequency component |
| $f_L$ | — | Lowest frequency component |
| $T_{sweep}$ | — | Sweep period |
| $f(t)$ | — | Filter snapshot/template |
| $f_{A/D}$ | — | A/D sampling frequency |
| $f_{D/A}$ | — | D/A sampling frequency |
| $h(t)$ | — | Impulse response |
| $H_{TX}(\omega)$ | — | Impulse response of the TX antenna |
| $H_{RX}(\omega)$ | — | Impulse response of the RX antenna |
| $r(t)$ | — | Raw echo |
| $R$ | — | Range of interest |
| $Ra$ | — | Antenna load |
| $R_{far-field}$ | — | Far-field distance |
| $R_O$ | — | Maximum operating range |
| $R_{max}$ | — | Maximum unambiguous range |
| $t$ | — | Delay of interest |
| $t_{PRI}$ | — | Pulse repetition interval |
| $t_\delta$ | — | Total delay range |
| $T_e$ | — | Noise temperature |
| $v_{max}$ | — | Maximum speed detectable |
| $v(t)$ | — | Returned echo without the background |
| $W(\omega)$ | — | Windowing function |
| $\beta$ | — | Band of interest |
| $\delta(t)$ | — | Dirac delta |
| $\zeta(t)$ | — | Impulse response of the scene |
| $\tau_{Charge}$ | — | Active charge time |
| $\tau_{Discharge}$ | — | Passive discharge time |

# Nomenclature

**A/D**—Analogue to digital converter.

**Bandwidth**—Also called **"occupied bandwidth"** is the frequency range within which some specified fraction, say 90 or 99 percent, of the total signal energy lies. This may be defined for a single pulse, if all pulses are the same, or for a group of pulses that are processed together to yield a single decision. The upper limit of this range is denoted here by $f_H$ and the lower limit by $f_L$.

**Beamwidth**—The angular width of a slice through the main-lobe of the radiation pattern of an antenna in the horizontal, vertical or other plane.

**Bistatic radar**—A kind of radar utilizing two separate antennas - one for transmitting and another for receiving RF signals.

**Centre frequency**—A frequency calculated as $\frac{f_H - f_L}{2}$.

**D/A**—Digital to analogue converter.

**DAQ**—Data acquisition.

**DSO**—Digital storage oscilloscope.

**DSP**—Digital signal processing.

**Fractional bandwidth**—A ratio between bandwidth and centre frequency denoted as $\frac{2(f_H - f_L)}{f_H + f_L}$.

**GPR**—Ground penetrating radar.

**GUI**—Graphical user interface.

**IO**—Input and output.

**I/O**—Input or output.

**Maximum unambiguous range**—The maximum distance up to where targets can be unambiguously detected.

**Monostatic radar**—A kind of radar utilizing a single antenna for both transmitting and receiving RF signals.

**Monolithic**—Single-ended.

**PLL**—Phase-locked loop.

**PRF**—Pulse repetition frequency.

**Range**—The radial distance from a radar to a target.

**RF**—Acronym of *Radio Frequency*.

**RX**—Receiver/received.

**Simulation Program with Integrated Circuits Emphasis (SPICE)**—A general purpose analog circuit simulator. Various circuit simulators, such as Protel, OrCAD, and Switcher CAD III (LTspice) are based on SPICE.

**T-R switch**—A switch that activates either TX or RX circuits at any given time, but not both.

**TX**—Transmitter/transmitted.

**Ultra-Wideband (UWB)**—A term used to describe RF signals with fractional bandwidth $\geq$20%.

# Chapter 1

# Introduction

Ultra-wideband (UWB) technology by definition refers to radio-frequency (RF) systems utilizing signals with a fractional bandwidth $\geq$20% of the centre frequency [12]. Direct generation of base-band pulses is the simplest method of generating such signals. Recently UWB technology has drawn considerable attention in the radar context [38, 46, 49, 53]. Such radar systems typically generate short pulses of duration less than 1 ns at high pulse repetition rates of several MHz, depending on the desired unambiguous operating range. Several UWB pulsed designs have been reported in the literature with bandwidths exceeding 1 GHz, which suggests that UWB technology can be used to produce a low cost, high resolution radar for short-range applications. Applications of UWB pulsed technology include radar, communication systems and geo-location.

UWB radar and communications systems are of particular interest in military applications as they have the benefit of low probability of interception and detection, a consequence of extremely low spectral power density (Watts per Hz). Narrow-band communication links may be more easily detected, although the information streams can be encrypted.

Short-range UWB radar finds application in vehicle piloting, ground penetrating radar, detection of motion through walls, and detection of weapons [38, 46, 49, 53]. Extremely simple architectures have been developed, which result in compact, low power consumption devices for short range applications.

Geo-location (tagging) is also one of the uses of UWB pulse technology for the reasons such as low production cost due to simple architecture e.g. asset control [8]. The wide bandwidth allows precise location of tagged objects.

## 1.1 Purposes

The purposes of this study are as follows:

1. To analyse and implement an ultra-wideband (UWB) pulse transmitter and receiver *sub-system* published by [47]. Its pulse repetition frequency (PRF) is roughly

2.4 MHz, and can be potentially used in short-range applications such as ground-penetrating radar (GPR) or through-wall imaging/detection (TWI/D).

2. Based on the sub-system, to build a complete UWB pulse radar profiling system for short range radar applications by integrating the sub-system mentioned above with computerized control and data acquisition systems.

3. To design and implement the necessary software to

   (a) control the system in 2 to acquire the raw signal from close vicinity;

   (b) process the raw signal to generate down-range profiles.

4. To identify antennas suitable for use with the prototype, and to evaluate the performance of the system under various conditions.

## 1.2 Structure of The Thesis

This dissertation is organized as follows:

- The rest of this chapter provides a brief literature review of UWB pulse technology.
- Chapter 2 gives an analysis of the principles of short pulse UWB radar and the architecture involved; it also shows the reference design by [47], and our design with modifications and additions.
- Chapter 3 provides a list of signal processing steps required to manipulate captured raw data to produce down-range profiles.
- Chapter 4 describes the simulation and implementation of the circuits involved.
- Chapter 5 explains the interfacing of various hardware circuits and modules with a computer system to capture raw data.
- Chapter 6 presents software designed to provide an interface between the user and the profiling system, and how signal processing codes are implemented.
- Chapter 7 presents results from various testing conditions.
- Chapter 8 concludes this project and identifies possible future research.

## 1.3 Literature Review

The root of UWB radar technology dates back to World War II when pulse radars were first used to facilitate remote sensing. However, modern UWB radar technology has only started rapid developing since 1990 after Fullerton, L.W patented an easy method to generate base-band pulses [15] and an implementation of an "UWB Radar Motion Sensor" patented in 1994 by [30].

This section presents a brief literature survey of UWB technologies found in radar applications, and suitable antenna designs for these applications.

### 1.3.1 UWB Technology for Radar

Pulsed radar is not a new technology, having been around since World War II. Advances in semiconductor electronics, have led to the development of short pulse *ultra-wideband* (UWB) radar technology [21, 23, 50]. UWB pulse systems emit short pulses with extremely wide bandwidths, which can exceed 1 GHz, offering considerably finer resolution than most conventional pulsed radars.

Today, cheap, easily constructed UWB radar designs have become available which eliminate the need for linear power amplifiers, transmit filters, mixers, PLL, reference oscillator and other components [47]. High/Ultra-high resolution radars which can image with sub-centimetre precision have been implemented [19, 31]. Vehicular radars are now available which scan surroundings to provide collision detection/avoidance, to adjust damping reactions according to road surfaces ahead, and to pilot the vehicle without human intervention [25].

Ground-penetrating radar (GPR) technology has long been developed [19]. One approach is called *stepped frequency continuous wave* radar which involves transmitting sinusoidal signals with a range of discrete frequencies [19]. This contrasts with a pulsed UWB radar which transmits signals covering the desired frequency range in one pulse by direct pulse generation [26, 55].

There is an increasing interest in through-wall imaging/detection (TWI/D) systems. Using a frequency range of 1~3.5 GHz, moving people can be detected through cement walls to aid police in hostile situations, and rescue workers and firefighters to locate victims buried under collapsed buildings or trapped beneath snow [56].

### 1.3.2 Wideband Antennas Suitable for UWB Technology

In order to make effective use of the wide bandwidth generated by the UWB pulses, pulses must be able to radiate and be received by antennas operating at the corresponding frequency range. In practice, antennas are almost always the limiting factor in terms of bandwidth because simple electronic circuits can generate pulses with bandwidths which far exceed the operating frequency range of the antennas to which they are coupled with.

Several UWB-specific antenna references are available such as [14, 24, 41, 42, 43] including both microwave antennas and magnetic antennas. Simulation of the conventional dipole for UWB applications[17] and designs of UWB resistively-loaded sensors [32] are also available. The antennas used in this project are mainly those developed in house in various student projects [45], others developed as part of a research project [5], as well as commercial TV antennas operating in VHF and UHF bands (shown in Table 5.1 in Chapter 4).

# Chapter 2

# Short Pulse UWB Principles and Implementation Architecture

Ultra-wideband pulsed radar systems operate by transmitting short pulses instead of sinusoidal wave pulses used in conventional radar systems [24]. UWB technology has the advantage of simpler hardware and higher fractional bandwidth, compared to conventional technology. This chapter gives an overview of the UWB system design including the operating principles of conventional pulse radar and UWB radar, and an introduction to the signal processing techniques involved.

## 2.1 Conventional Pulse Radar

A conventional pulsed radar operates by sending and receiving pulses. It is often necessary to translate the signal up in frequency to gain better directionality and to fulfil other requirements. A typical cycle would consists of two phases: transmitting phase and receiving phase. In the transmitting phase, a pulse is generated and transmitted, after a short delay cause by the T-R switch, the radar switches into receiving phase and acquires the returned echoes over a period of time. Then after another short delay caused by the T-R switch, the system switches into the transmitting phase and the cycle repeats. Figure 2.1 from [27] shows the block diagram of an elementary radar system and some abbreviations commonly used.

The duration of one cycle is called "*Pulse Repetition Interval*" (PRI), $t_{PRI}$ in second, which can be converted to "*Pulse Repetition Frequency*" (PRF) $f_{PRF} = \frac{1}{t_{PRI}}$ in Hz. Since electromagnetic waves travel at the speed of light $c \approx 3 * 10^8 m/s$, the PRI/PRF determines the maximum unambiguous range (the maximum range from which a transmitted radar pulse can be reflected and received before the next pulse is transmitted) denoted by $R_{max} = \frac{ct_{PRI}}{2} = \frac{c}{2f_{PRF}}$ which is equivalent to $f_{PRF} = \frac{c}{2R_{max}}$. E.g. maximum PRF values are 500 Hz for 300km range, and 15 kHz for 1km range. However, due to other constraints, typically pulse repetition frequencies vary from several hundred Hertz for a

long range radar (several hundred km in range) to hundreds of kHz for short range radars (up to 1 km in range).

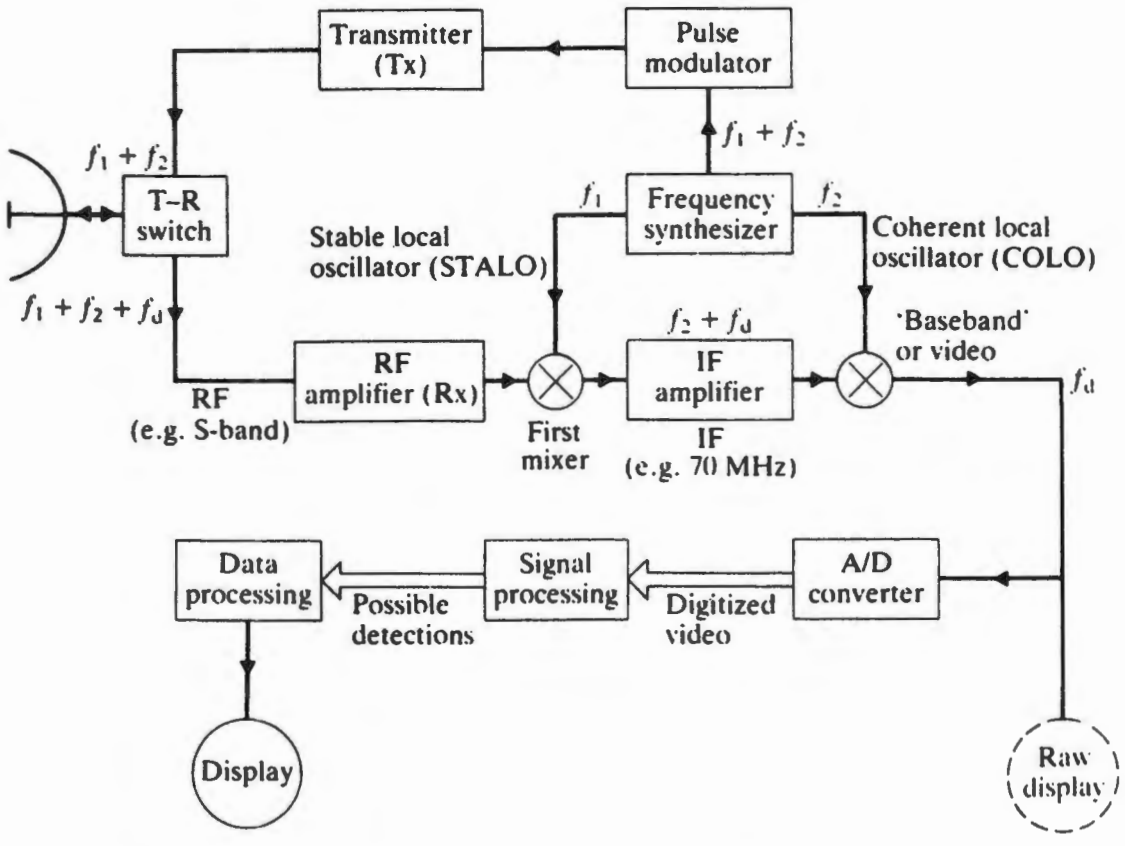


Figure 2.1: Block diagram of an elementary radar system, and some abbreviations commonly used [27].

## 2.2 Operation of UWB Radar

The UWB radar prototype implemented is based on a sub-system published by Enrico M. Staderini [47]. The actual electronic circuits presented in [47] are mainly based on what was disclosed in a few US patents by L. W. Fullerton [15], and T. E. McEwan [30], along with experiences of the author himself. Figure 2.2 shows the architecture as it appeared in [47]. The block labeled "pulse generator" generates a clock at a frequency of approximately 2.4 MHz. The pulse train is then fed into two blocks: (1) the "transmitter" block, which generates short (sub nanosecond) pulses, driving the antenna; and (2) the "nanosecond delay line", which triggers the sampler. The delayed signal acts as a time-dependent trigger to the "fast sampler" which performs "sample-and-integrate" of the return echoes at a specific range. Figure 2.3 illustrates the operation of the "fast sampler" with a fixed delay of $28.548\mu s$.

The integration time of the fast-sampler is determined by the resistor-capacitor combination used. It is discussed in detail in section 4.3 of Chapter 4. By deploying the fast-sampler, operating at PRF $f_{PRF}$= 2.0 MHz, typically it needs $1ms$ to $10ms$ to integrate

enough returned echoes at one fixed delay. This, in turn, limits the maximum sweeping rate $f_{max}$and maximum speed $v_{max}$ at which a moving target can be detected because the scene must be *stationary* within the integration time to produce an accurate reading. Further discussion of the maximum sweeping rate and maximum speed detectable can be found in Section 7.10 of Chapter 7.

Albeit the limitations, the advantage of such an architecture is largely-reduced direct-sampling requirements of RF signals, i.e. twice the highest frequency component. For a radar operating at the frequency band up to 2 GHz, if one is to sample directly from the antennas, the minimum A/D sampling requirement is 4 GHz as required by Nyquist theorem. Instead, UCT UWB radar profiling system requires an A/D sampling of a few kHz; depending on the rate at which the delay is swept from near the nearest to the farthest range.

To improve the signal to noise ratio, the output of the fast sampler is fed to the "averager", which effectively integrates the returns from several hundred pulses. The prototype described in [47] is a very basic implementation, in which the delay line is manually adjusted, to provide a detection at a fixed range.

The UCT UWB radar profiling system developed in this MSc project is a complete system and capable of providing a real-time down-range profile display updated at two profiles per second. Figure 2.4 shows a block diagram of the UCT UWB radar profiling system using the same antenna for both transmission and reception. It operates by sliding the range gate (varying the delay) with the variable delay circuit whilst sampling the output of the instrumentation amplifier. A down-range profile is acquired as the range gate is moved from near to far range. A second block diagram, Figure 2.5, shows the configuration used for bi-static radar mode in which the transmitter and receiver are connected to separate antennas. The bi-static mode allowed incorporation of a front-end RF amplifier module made by [59] into the fast sampler-averager without additional input circuit protection because the transmitted pulses are never fed into it.

The minimum step of which the delay circuit can increment achievable by this system is 15ps with the current data acquisition hardware. However, smaller steps such as 1ps can be achieved by using better data acquisition hardware. The implementation and limitations of the variable delay line is discussed in detail in Subsection 4.4 of Chapter 4.

## 2.3 Signal Model for an UWB Radar

A radar may be modelled as a linear system. For any linear system, the output $y(t)$ may be related to the input $x(t)$ by convolving the input signal with the impulse response of the system, i.e.

$$y(t) = x(t) \otimes h(t) = \int_{-\infty}^{+\infty} x(\tau)h(t-\tau)d\tau \tag{2.1}$$

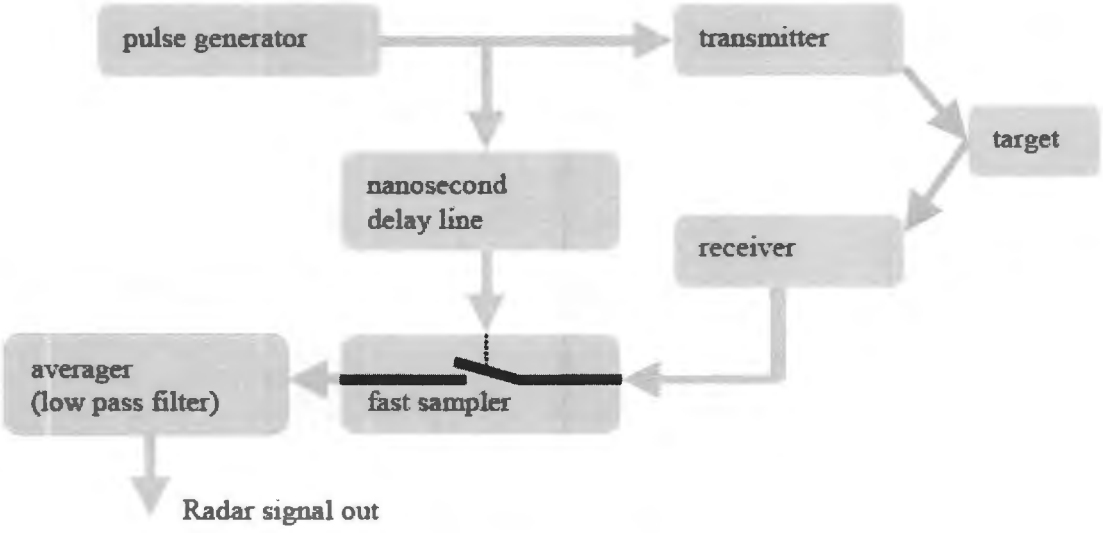


Figure 2.2: The UWB radar scheme[47].

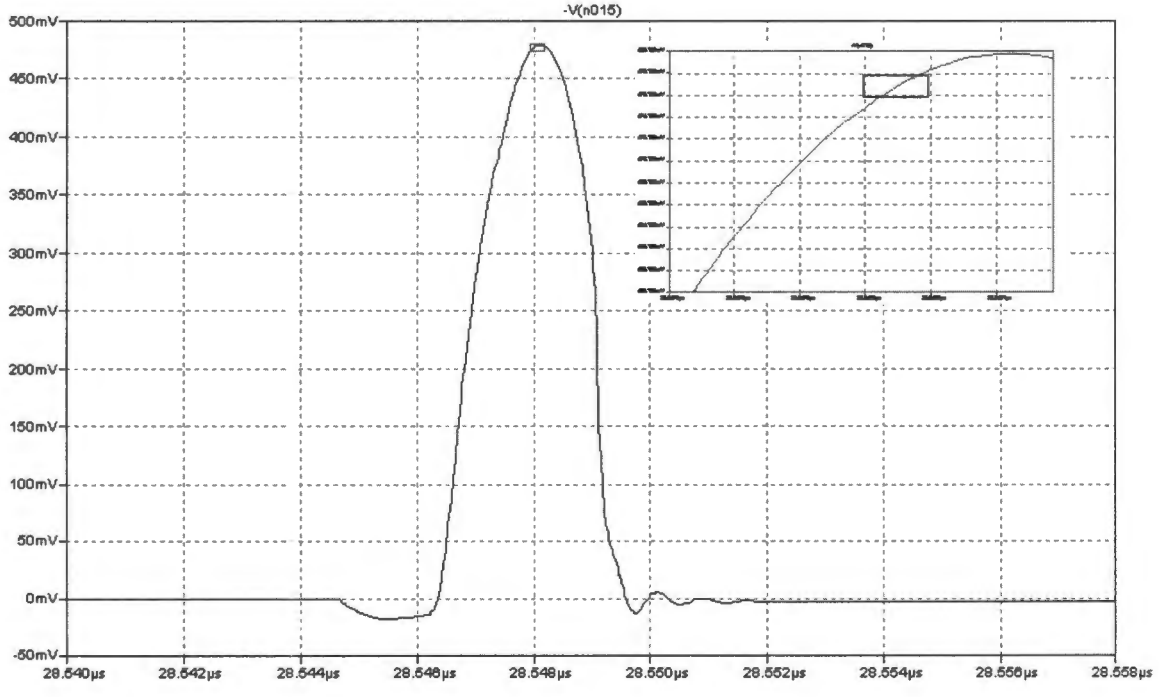


Figure 2.3: Operation of the "fast sampler" with a fixed delay.

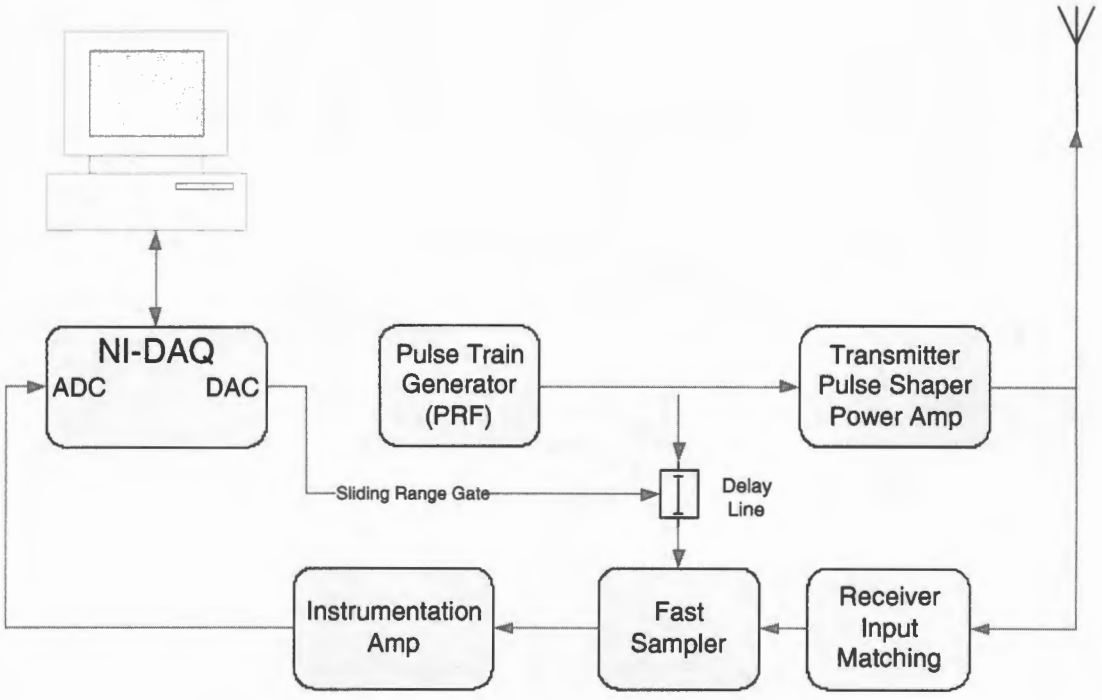


Figure 2.4: UCT UWB radar scheme (Mono-static).

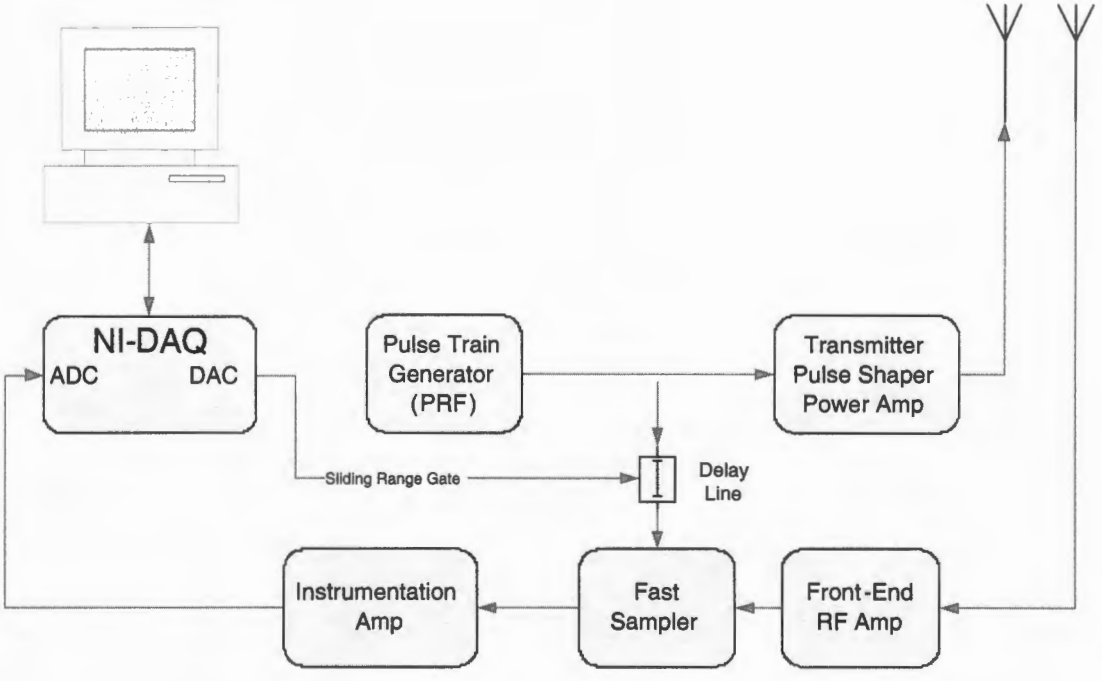


Figure 2.5: UCT UWB radar scheme (Bi-static).

where $h(t)$ is the response of the linear system to a Dirac delta $\delta(t)$ , which is termed *"impulse response"* [60]. In the case of radar transmitting a Dirac impulse, the received echo is the impulse response of the system. It can be derived by substituting $x(t)$ with $\delta(t)$ in Equation 2.1:

$$y(t) = \delta(t) \otimes h(t) = \int_{-\infty}^{+\infty} \delta(\tau)h(t-\tau)d\tau = [h(t-\tau)]^{\tau=0} = h(t) \quad (2.2)$$

In practice, it is not possible to generate a Dirac impulse, but a band-limited version of it. Equation 2.1 can be represented in the frequency domain as

$$Y(f) = X(f)H(f) = \int_{-\infty}^{+\infty} x(t)e^{-j2\pi ft}dt \int_{-\infty}^{+\infty} h(t)e^{-j2\pi ft}dt \quad (2.3)$$

and with a band-limited version of Dirac impulses of bandwidth $B$ the followings can be derived using inverse Fourier transform:

$$y(t) = f^{-1}Y(f) = f^{-1}\left[\int_{-B}^{B} X(f)e^{j2\pi ft}df \int_{-B}^{B} H(f)e^{j2\pi ft}df\right] \quad (2.4)$$

The impulse response at the antenna terminals can be represented as

$$H(f) = H_{TX}(f)\zeta(f)H_{RX}(f)$$

where $H_{TX}$ denotes the impulse response of the transmitting antenna, $H_{RX}$ denotes the impulse response of the receiving antenna, and $\zeta(f)$ denotes the impulse response of the scene. Let $V_{TX}(f)$ be the pulse fed into the transmitting antenna terminal, the received signal at the receiving antenna terminal can then be defined as

$$V_{RX}(f) = V_{TX}(f)H(f)$$

Therefore, the signal fed into the "fast sampler" can be defined as

$$V_{RX}(f) = V_{TX}(f)H(f)H_{Rec}(f) = V_{TX}(f)H_{TX}(f)\zeta(f)H_{RX}(f)H_{Rec}(f)$$

where $H_{Rec}(f)$ denotes the impulse response of the front-end RF amplifier.

One of the challenges in UWB systems is to be able to extract the response of the scene over a very wide frequency band because received echoes are comprised of multiple frequencies which not only carry information of the target location, but also the characteristics of the target. This phenomenon can be explained by decomposing the wideband pulse $V_{TX}(f)$ into $n$ narrow-band pulses in frequency domain where $V_{TX}(f) = \sum_{k=1}^{n} V_{TX}^{k}(f)$. If the target has a geometric size $a$, and each $V_{TX}^{i\in 1\ldots n}(f)$ has wavelength $\lambda_{i\in 1\ldots n}$, *"for wavelengths $\lambda_i \ll a$, responses are said to be of a high frequency or optical nature; for*

*$\lambda_i \approx a$, they are called resonance responses and for $\lambda_i \gg a$ they are low frequency or Rayleigh responses"* [3].

# Chapter 3

# Signal Processing

Since received echoes will consist of, possibly the target of interest, usually the background clutter, definitely noise, and perhaps interferences from other sources, some methodologies must be used to extract the response of the target of interest from the received echoes. This chapter discusses these signal processing techniques utilized in the operation of the system to achieve such an objective.

## 3.1 Background Removal (Difference Imaging)

In order to remove the background clutter, a background snapshot $b(t)$ would have been taken prior to the operation of the system. This snapshot will be subtracted in all the processes that follow. Let $r(t)$ denote the raw echo as a function of time $t$, its background-removed version is $v(t) = r(t) - b(t)$ .

## 3.2 Out-of-Band Signal Nulling

By nulling all out-of-band noise introduced by the front-end RF amplifier and post-sampler amplifier, one can minimize their interferences at the cost of reduced bandwidth. If $\beta$ is the band of interest, and $V(\omega)$ is the returned echo (both in frequency domain), nulling can be done by making $V(\omega) = 0 \quad \forall \omega \notin \beta$. This technique is best applied right after transforming time-domain signals to frequency domain because it eliminates unnecessary calculations that would have been carried out if nulling is to be done later.

## 3.3 Matched Filter (Correlator)

A matched filter is obtained by correlating a known signal (filter template), with an unknown signal (returned echo) to detect the presence of the filter template in the unknown signal. This is equivalent to convolving the unknown signal with a time-reversed version of the filter template. The matched filter is the optimal linear filter for maximizing the

signal to noise ratio (SNR) in the presence of additive stochastic noise [48]. Let the filter template be $f(t)$. A matched filter can be applied to the returned echo $v(t)$ by using the discrete Fourier transform (DFT) as follows:

$$V(\omega) = fft(v(t))$$

$$F(\omega) = fft(f(t))$$

$$V_E(\omega) = V(\omega)F^*(\omega)$$

$$v_E(t) = ifft(V_E(\omega))$$

where $v_E(t)$ is the filtered echo.

## 3.4 Deconvolution Filter

A deconvolution filter is very similar to a matched filter, with the only difference that instead of applying $F^*(\omega)$, the inverse filter $\frac{1}{F(\omega)}$ is used over a finite bandwidth. The effect is that the resulting signal have a flat-top in the frequency domain, which is a *"Sa"* or *"sinc"* function in the time domain [60]. Let the filter template be $f(t)$, we can process the returned echo $v(t)$ as follows:

$$F(\omega) = fft(f(t))$$

$$V(\omega) = fft(v(t))$$

$$V_E(\omega) = \frac{V(\omega)}{F(\omega)}$$

$$v_E(t) = ifft(V_E(\omega))$$

where $v_E(t)$ is the filtered echo.

## 3.5 Window Functions

One of several windowing functions can used to decrease side-lobes at cost of widening the main-lobe. Let the filter template be $f(t)$, it can be applied in conjunction with either matched filter or deconvolution filter to the returned echo $v(t)$ as follows:

$$F(\omega) = fft(f(t))$$

$$V(\omega) = fft(v(t))$$

$V_E(\omega) = V(\omega)F^*(\omega)W(\omega)$ for matched filter or $V_E(\omega) = \frac{V(\omega)}{F(\omega)}W(\omega)$ for deconvolution filter.

where $W(\omega)$ is the windowing function of choice.

$$v_E(t) = ifft(V_E(\omega))$$

where $v_E(t)$ is the filtered echo.

The implemented windowing functions are Hanning, Hamming and Blackman windowing functions as shown in Figure 3.2, 3.2, and 3.3.

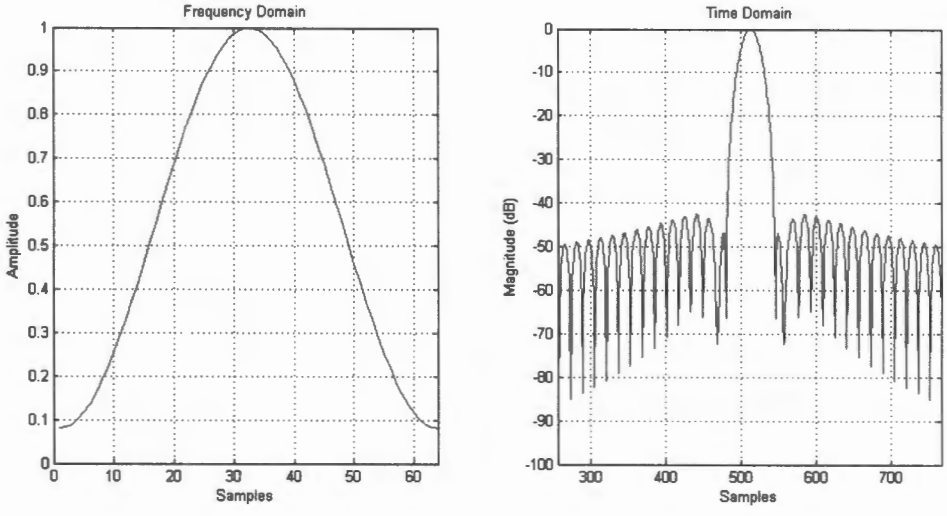


Figure 3.1: Hanning window; $W[k+1] = 0.5\left(1 - \cos\left(2\pi\frac{k}{n-1}\right)\right), k = 0, \cdots, n-1.$

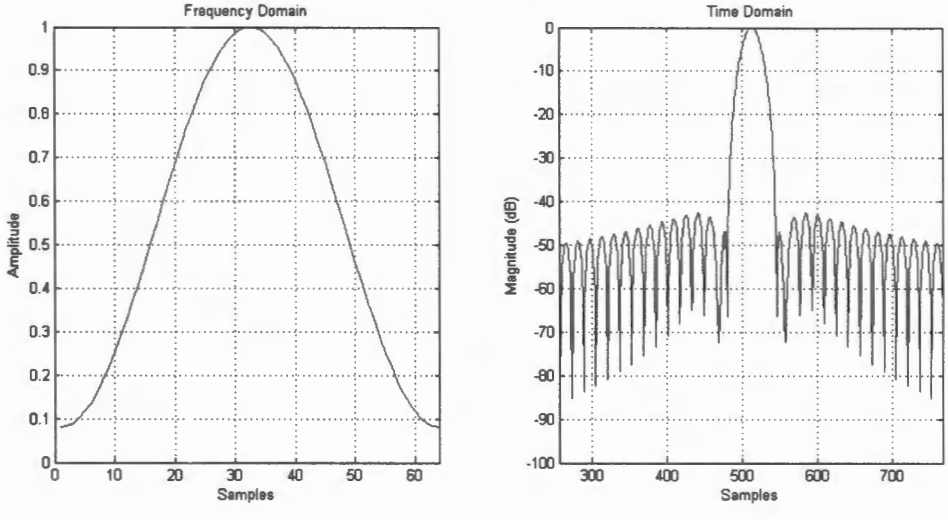


Figure 3.2: Hamming window; $W[k+1] = 0.54 - 0.46\cos\left(2\pi\frac{k}{n-1}\right), k = 0, \cdots, n-1.$

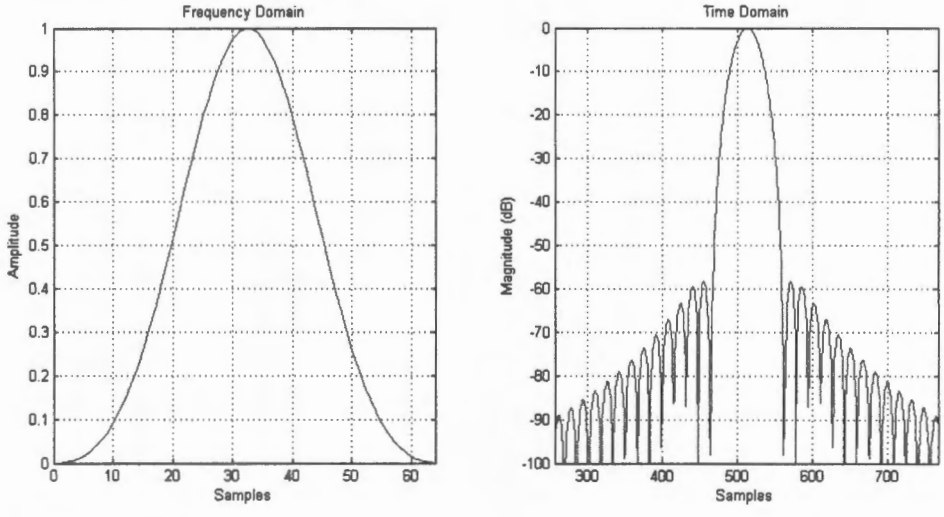


Figure 3.3: Blackman window; $W[k+1] = 0.42 - 0.5\cos\left(2\pi\frac{k}{n-1}\right) + 0.08\cos\left(4\pi\frac{k}{n-1}\right), k = 0, \cdots, n-1.$

# Chapter 4

# Circuits Simulation and Implementation

This chapter discusses circuits simulations using SwitcherCAD III©(LTspice) [28] and implementations of the various blocks shown in Figure 2.2 with improvements and additional circuits built in order to complete the UCT UWB radar design shown in Figure 2.4 and 2.5.

All the measurements were taken with Agilent Infinium 54833A DSO as shown in Figure 4.1. The DSO is capable of sampling 4 GS/sec with 1 GHz bandwidth. This means signals with more than 1 GHz bandwidth would be band-limited.

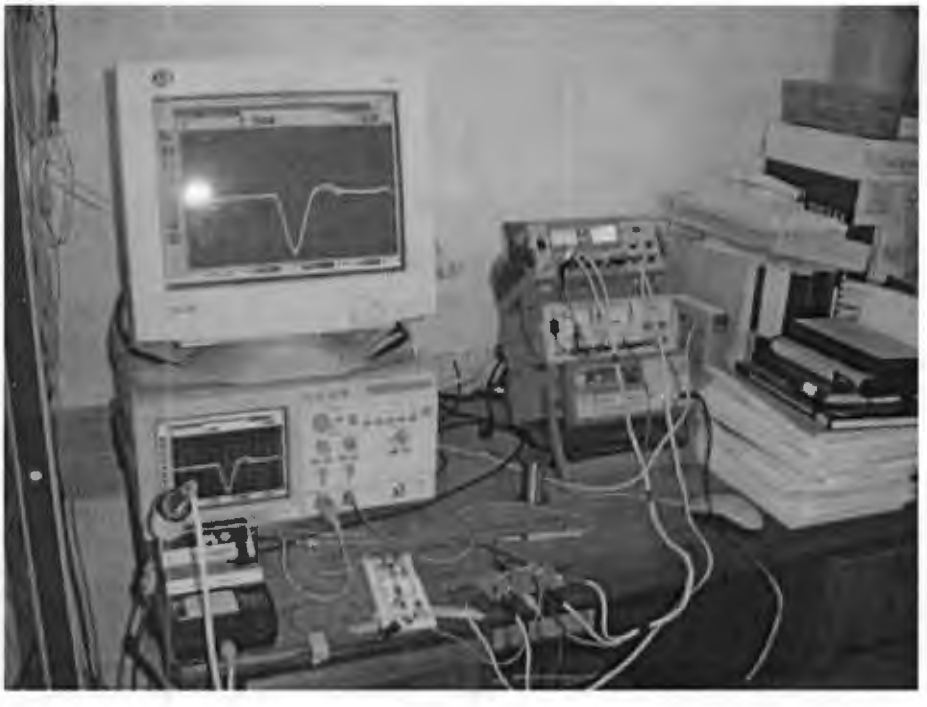

Figure 4.1: Agilent Infinium 54833A DSO

## 4.1 PRF Signal Generator

The PRF signal generator is the master clock of the system and triggers the generation of the transmitted pulses. Figure 4.2 shows a design by [47, 30, 1] which generates a time-jittered narrow pulse (90% duty cycle) train at the terminal marked **"out"** in Figure 4.2 with an averaged PRF of 2.4 MHz as in Figure 4.4. It operates by injecting thermal noise from the left half of the circuit (shown in Figure 4.6) to the right half in Figure 4.2.

The right half of the circuit (3/4 74HC04) is an astable that alone generates a 2.8 MHz pulse train. Figure 4.3 shows the simulated waveform. Figure 4.5 is the coupling of the oscillation of the right part of the circuit back into the left part.

Jittering smears the spectral components so that there are no distinct (and easily detectable) spectral harmonics. We have, however, opted for using a 50% duty-cycle square wave signal generator with adjustable frequency to gain greater control of the system. A PRF of 2.0 MHz was typically used, corresponding to a maximum unambiguous range of $R_{max} = \frac{c}{2*PRF} = \frac{3*10^8 m/s}{2*(2*10^6)Hz} = 75m$ which is more than sufficient for indoor testing.

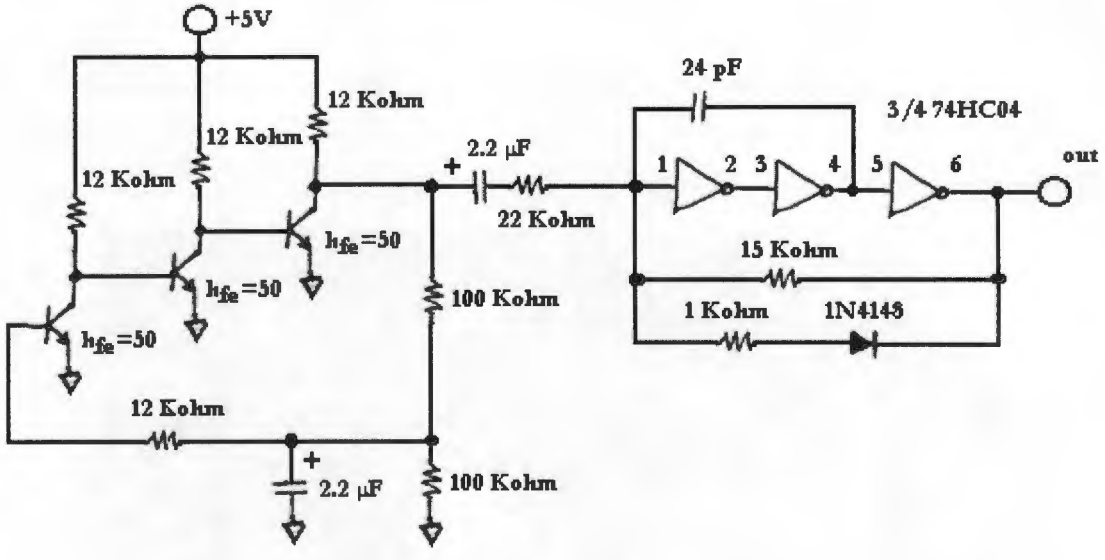


Figure 4.2: The noise modulated pulse generator used in [47, 30, 1].

## 4.2 Transmitter

The transmitter circuit by [47, 1, 30, 15] reproduced in Figure 4.7 was designed to drive a balanced dipole antenna. Monolithic base-band pulses are emitted whenever the base of the transistor in Figure 4.7 is triggered by the PRF waveform [47]. The design was modified to drive an antenna via (unbalanced) coaxial cables as shown in Figure 4.8. This allowed more freedom in experimenting with available antennas. After some initial experimentation, the original 2N5109 transistor (with a gain-bandwidth product of 1.2 GHz) was replaced with a BFR91A transistor (with a gain-bandwidth product of 6.0 GHz).

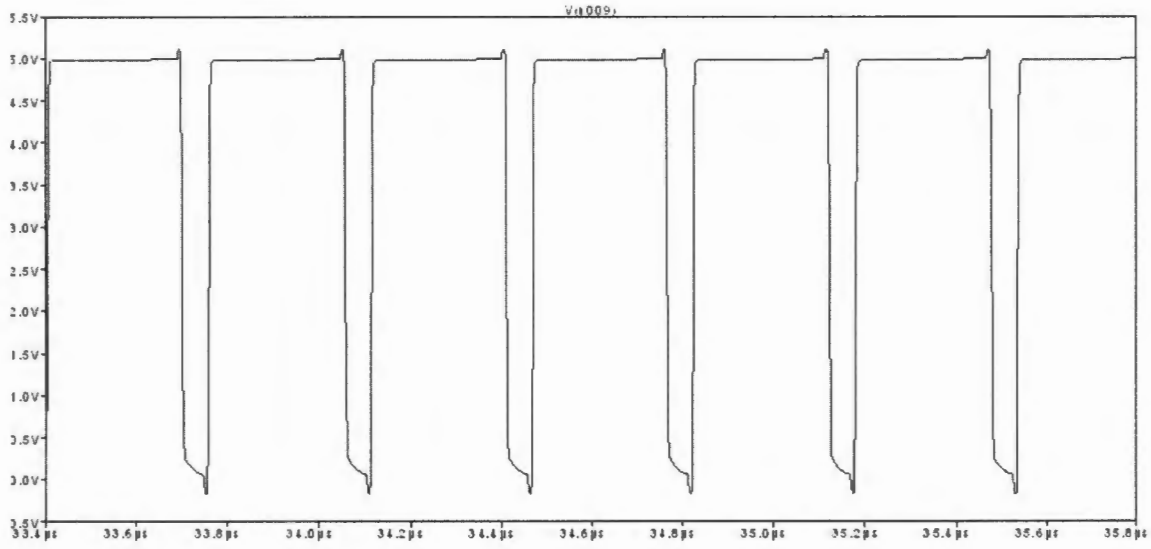

Figure 4.3: The simulated output voltage at node "out" (in Figure 4.2) is plotted as a function of time. The period is approximately 360 ns.

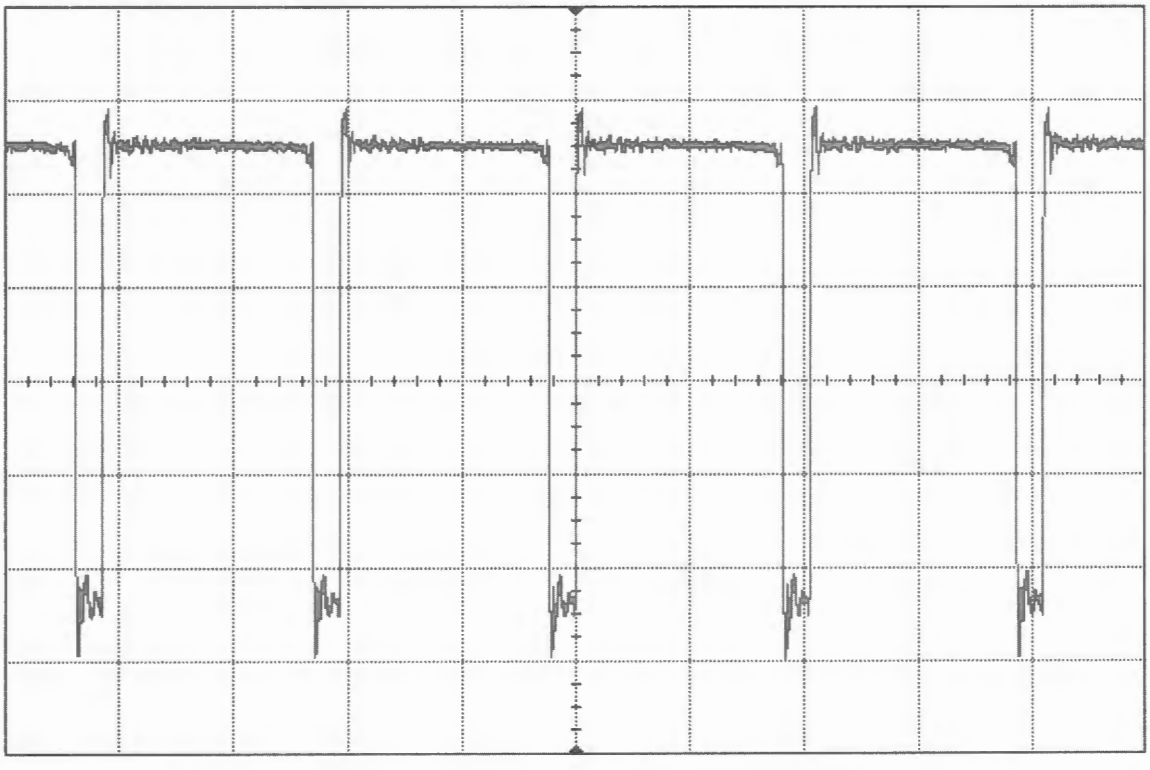

Figure 4.4: The measured output voltage at node "out" (in Figure 4.2) is plotted as a function of time. The period is approximately 420 ns.
Vertical (voltage) scale 1.00 V / Offset 2.46V.
Horizontal (time) scale 200 ns.

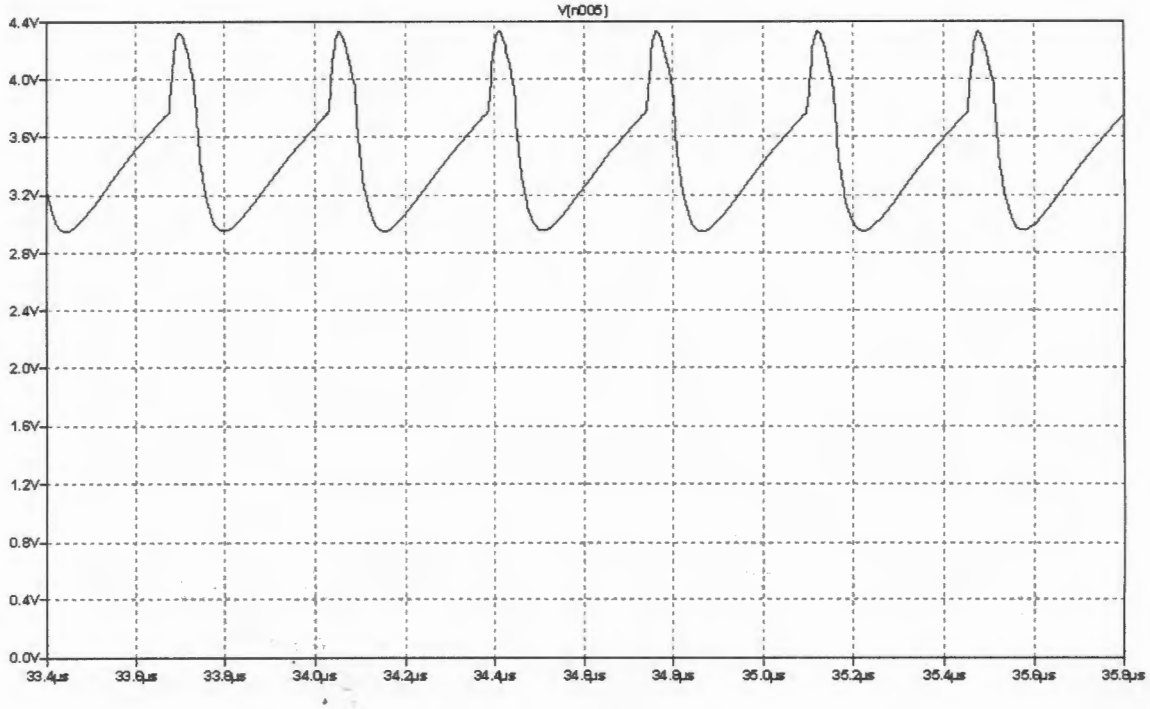


Figure 4.5: Noise generated from the left-half of the circuit shown in Figure 4.2.

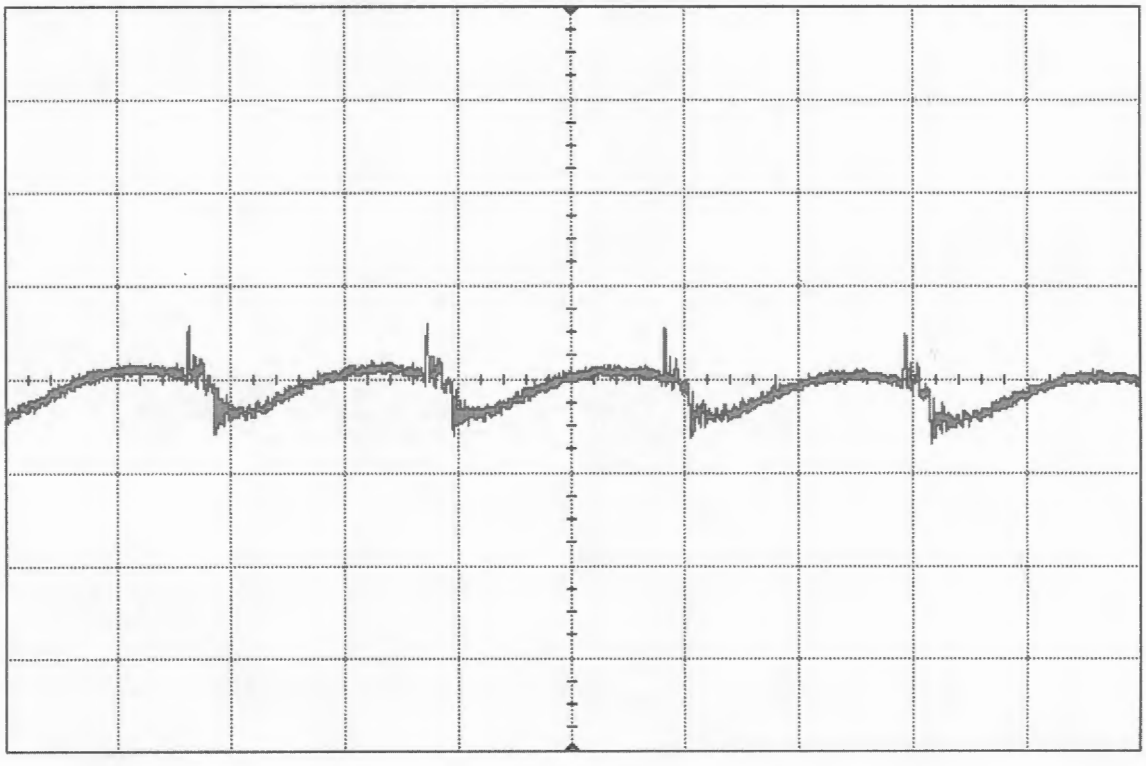

Figure 4.6: The measured noise generated from left-half of the circuit shown in Figure 4.2.
Vertical (voltage) scale 500 mV / Offset 1.629V.
Horizontal (time) scale 200 ns.

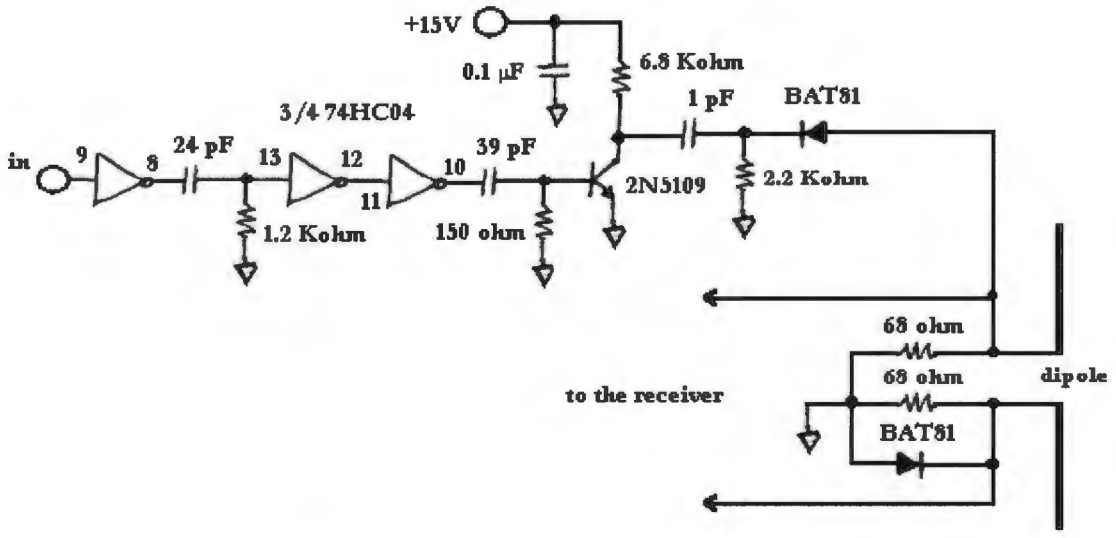


Figure 4.7: The transmitter used in [47].

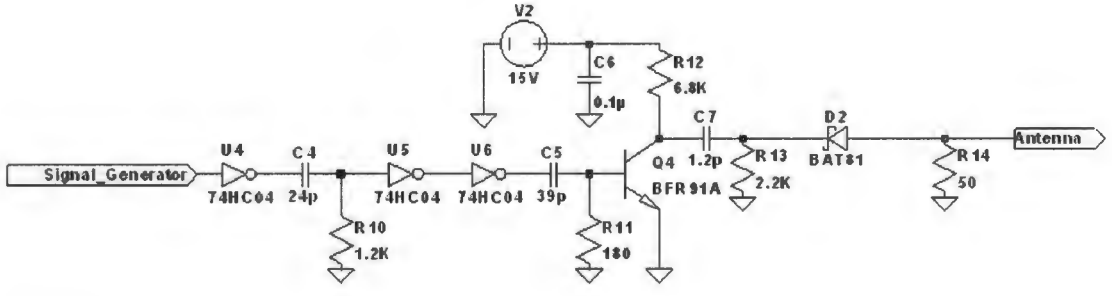


Figure 4.8: UCT UWB Radar Transmitter

The master clock is a 50% duty-cycle square wave with PRF of 2.0 MHz (the upper waveform in Figure 4.11). It triggers the emission of the pulses by the falling edges. When it is injected into the input labelled "Signal_Generator" in Figure 4.8: during the non-triggering phase, the circuit is charging capacitor C7 via the loop G–>V2–>R12–>C7–>R13–>G; during the triggering phase, capacitor C7 is rapidly discharged via the loop G–>R14–>D2–>C7–>Q4–>G. The function of the diode D2 is to prevent capacitor C7 being charged via the antennas which means unintended emission by the antennas.

The simulated waveform at node C4-R10-U5 is shown in Figure 4.10 while the lower waveform in Figure 4.11 is captured by the DSO. Since placing the oscilloscope probe at the node C5-R11-Q4 (which feeds into the base of the transistor Q4) will affect the waveform observed, only waveform generated by simulation is available as shown in Figure 4.12. The simulated pulses emitted at the antenna terminals using the circuits in Figure 4.7 and Figure 4.8 are shown in Figure 4.13 and Figure 4.15 respectively. The dipole antenna is simulated using the equivalent SPICE circuit in Figure 4.9 published by [17].

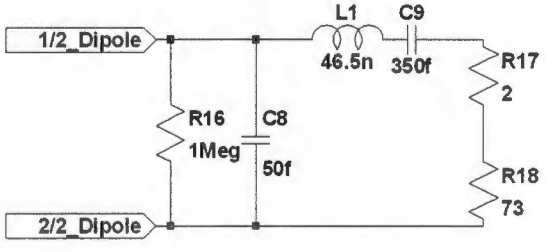


Figure 4.9: Equivalent SPICE circuit for a dipole antenna [17].

The simulated pulse shown in Figure 4.15 has a 3dB bandwidth, measured at the point voltage drops by $\frac{1}{\sqrt{2}}$ from the peak value, equal to 1.35GHz. Pulses captured by directly feeding the transmitter to the oscilloscope with input impedance of 50Ω are shown in Figure 4.14 and 4.16 using 2N5109 and BFR91A transistors respectively. The BFR91A transistor provided shorter pulses than those generated by the original 2N5109 transistor. The pulses generated by the BFR91A have usable spectral components from DC to 2 GHz as shown in Figure 4.17 while its measured 3dB bandwidth is 1.0GHz. Since the DSO has only 1 GHz bandwidth, the waveform observed in Figure 4.16 is band-limited by the scope, i.e. the pulse width and peak height are probably better than displayed.

## 4.3 Manual Delay Line and Fast Sampler-Averager

Figure 4.18 shows the fast sampler and integrator used in [47, 1, 30, 15]. A delay is generated according to the RC constant (obtained from the 1 kΩ fixed resistor in parallel with the 1 kΩ variable resistor coupled with the 47pF capacitor to ground) between PIN

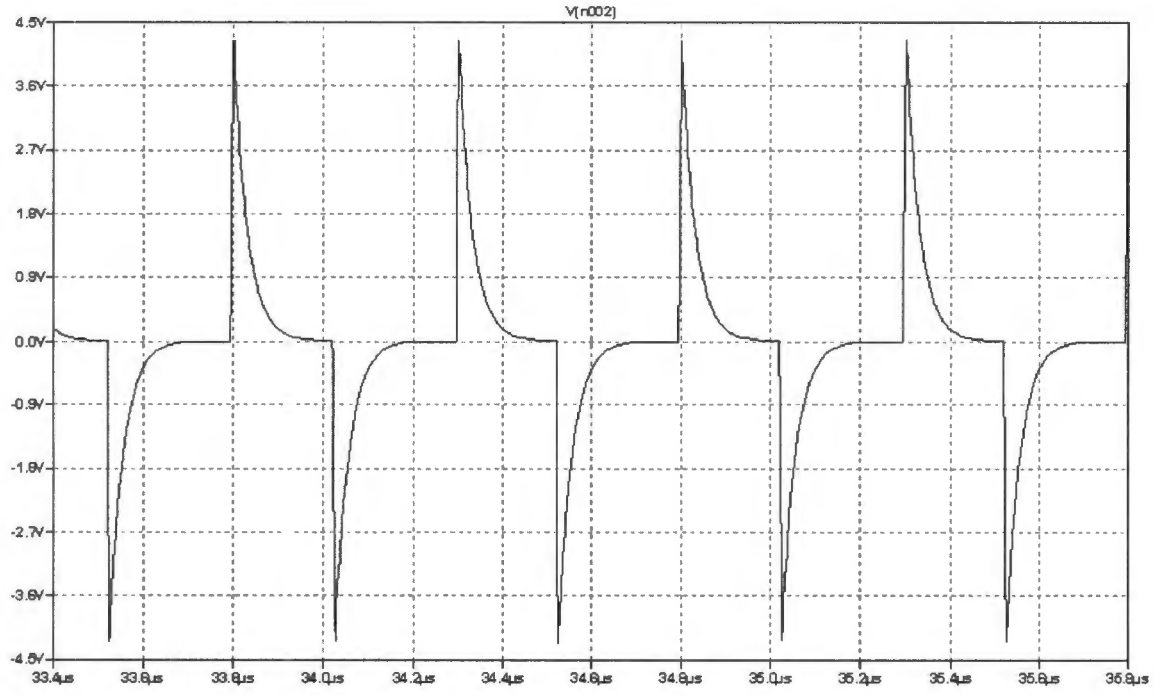


Figure 4.10: The simulated waveform at node C4-R10-U5.

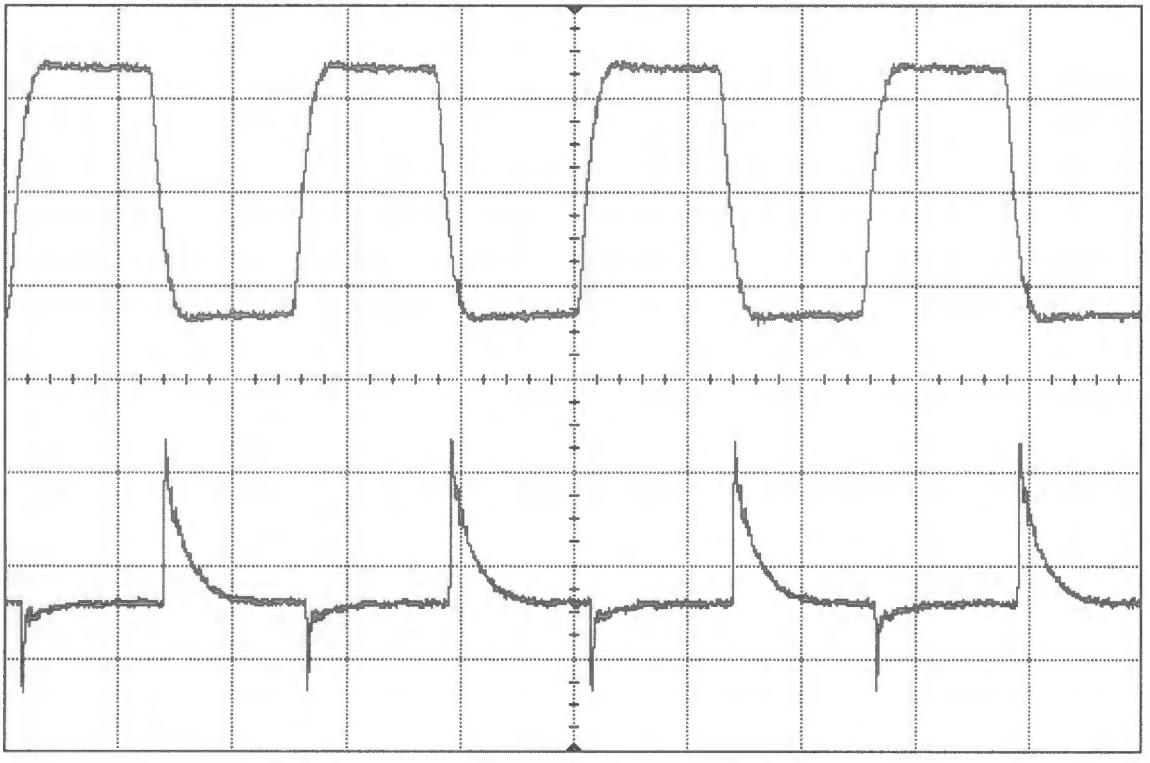

Figure 4.11: The measured waveform at C4-R10-U5 (lower waveform) with reference to the master clock (upper waveform).
Vertical (voltage) scale 2.0 V
Offset -1.47 V (master clock) / Offset 4.81 V (C4-R10-U5).
Horizontal (time) scale 200 ns.

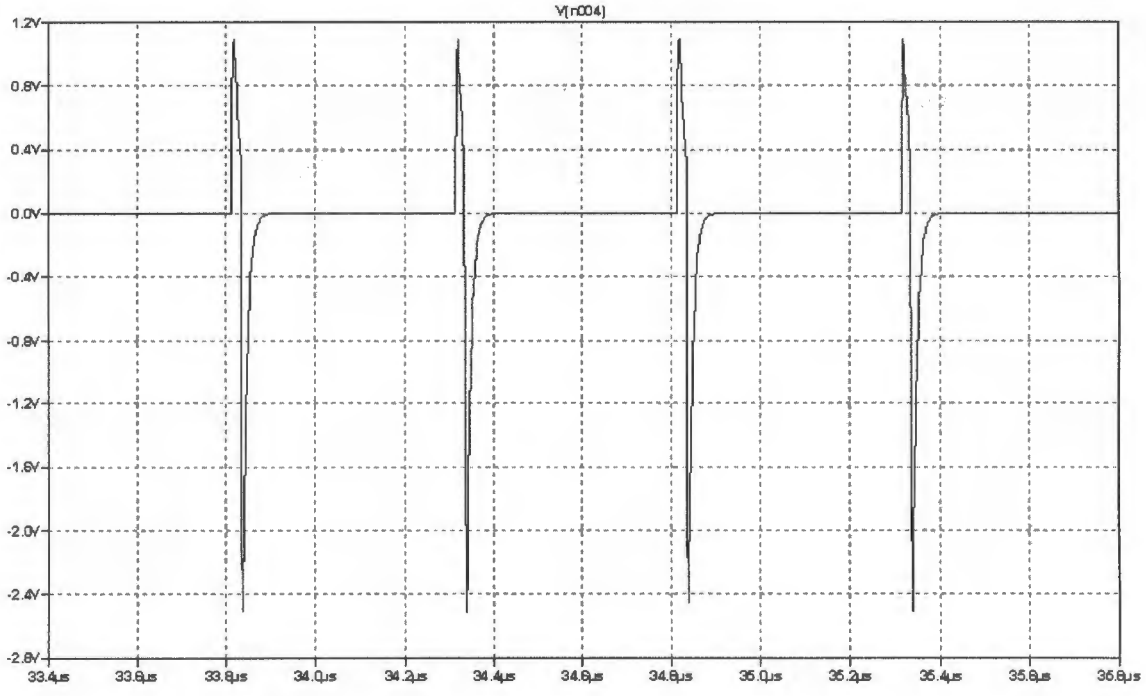


Figure 4.12: Wave form at node C5-R11-Q4 feeding into the base of the transistor Q4.

2 and PIN 3 of the inverter shown in Figure 4.18 as in [47]. However, in order to acquire a complete down-range profile, a variable delay line must be implemented. Our early prototypes used a fixed capacitor coupled with a variable resistor which enabled operators to adjust the delay by manually turning the variable resistor.

The fast sampler-averager is comprised of two integrating single-ended samplers [55], i.e. they sample the RF signals from the antenna terminals and accumulate DC voltages on the capacitors from sampled signals. It should be noted that several modifications (such as removing the Vref (virtual ground) and swapping the 4.7 MΩ resistors as in [47] with a different value) have been made to it in the UCT implementation in order to provide faster response time for near real-time operations as shown in Figure 4.19. The inner working of fast sampler-averager is discussed in section 4.4 and its performance and limitations are discussed in section 7.10 of Chapter 7.

## 4.4 Computer-Controlled Variable Delay Line and Fast Sampler-Averager

In order to vary the delay with a computer, a computer-controlled variable delay line was designed as shown in Figure 4.19. It is implemented by using a fixed resistor of 47Ω coupled with a varicap diode in the place of the manually adjustable delay line (between PIN 2 and PIN 3 in Figure 4.18). The capacitance of the varicap diode varies according to the reverse voltage across it, and for the MV104 device used, can vary between about 15pF (at 30V) to about to 80pF (at 0.3V). The response is, however, not linear; being that the capacitance varies quite a lot at the lower voltage and varies very little at voltages

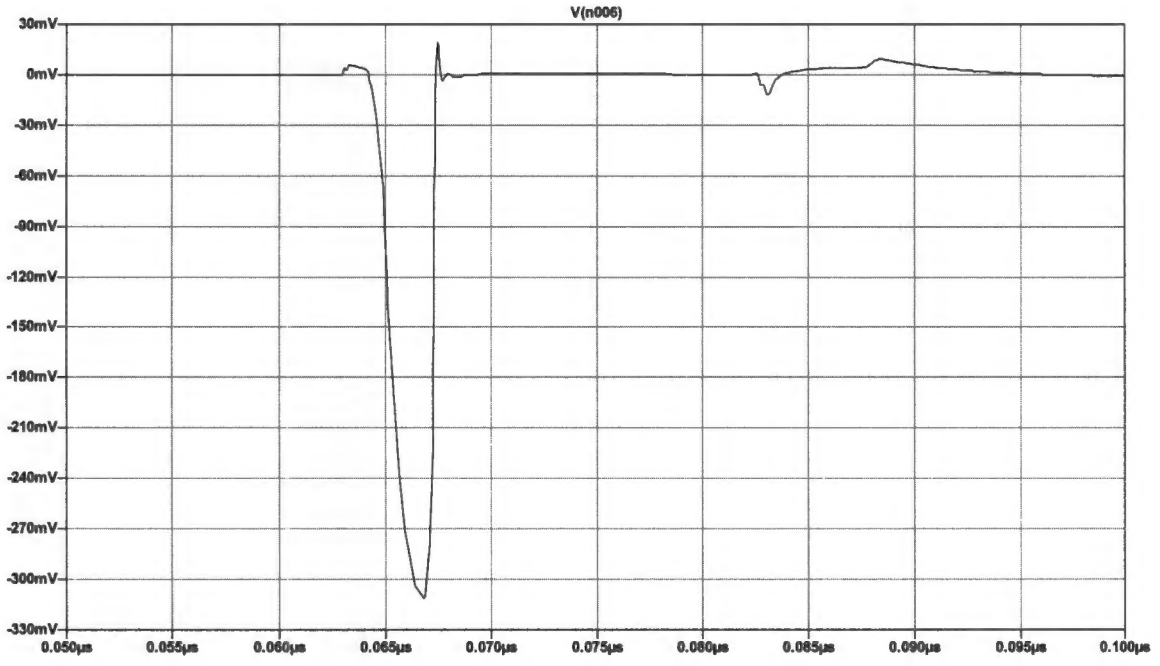


Figure 4.13: Simulated pulse using 2N5109 transistor across 50Ω load.

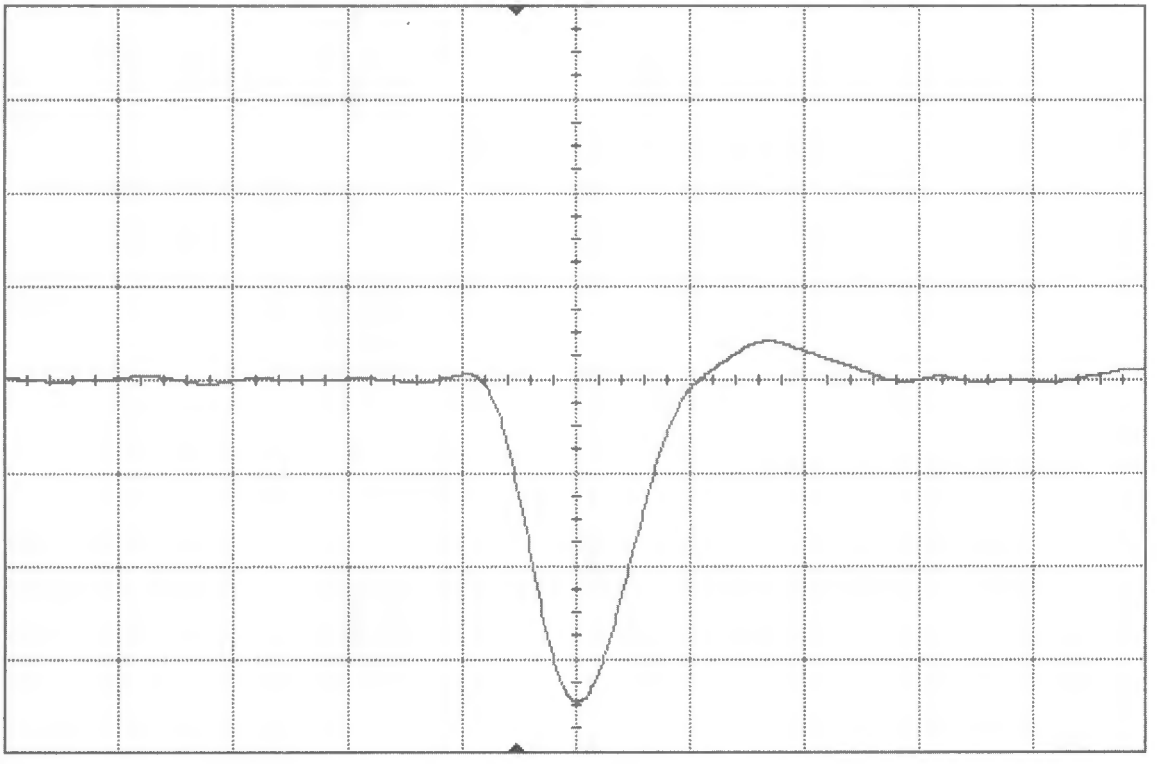

Figure 4.14: The measured waveform generated by 2N5109.
Vertical (voltage) scale 500 mV / Offset 0.
Horizontal (time) scale 2 ns.

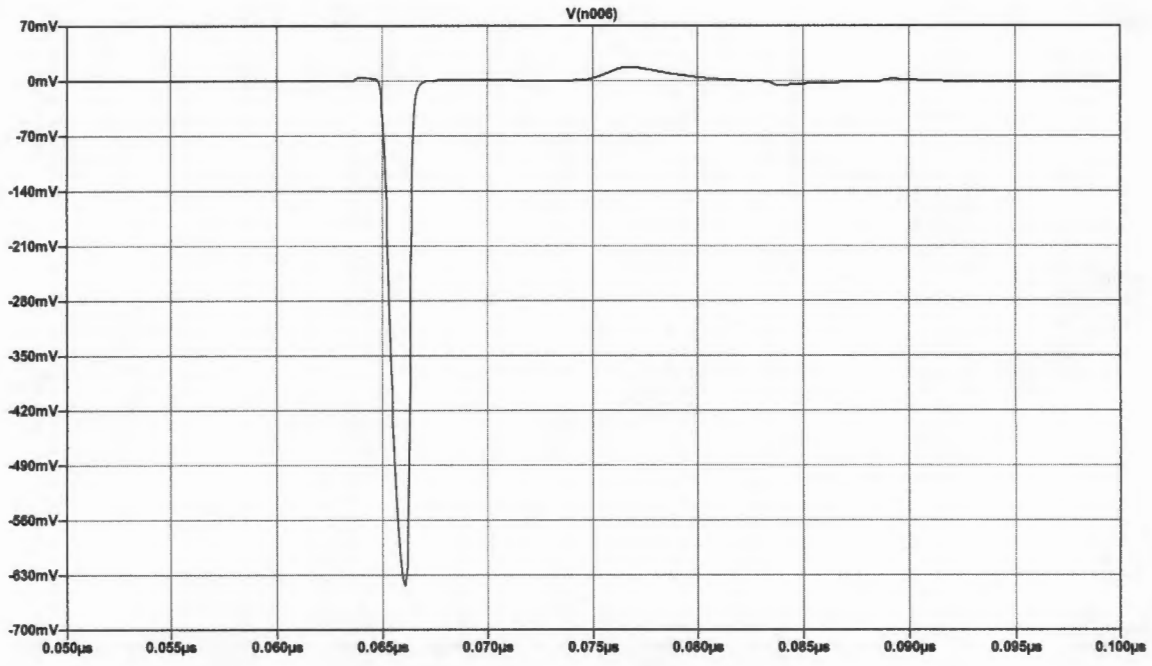


Figure 4.15: Simulated pulse using BFR91A transistor across 50Ω load.

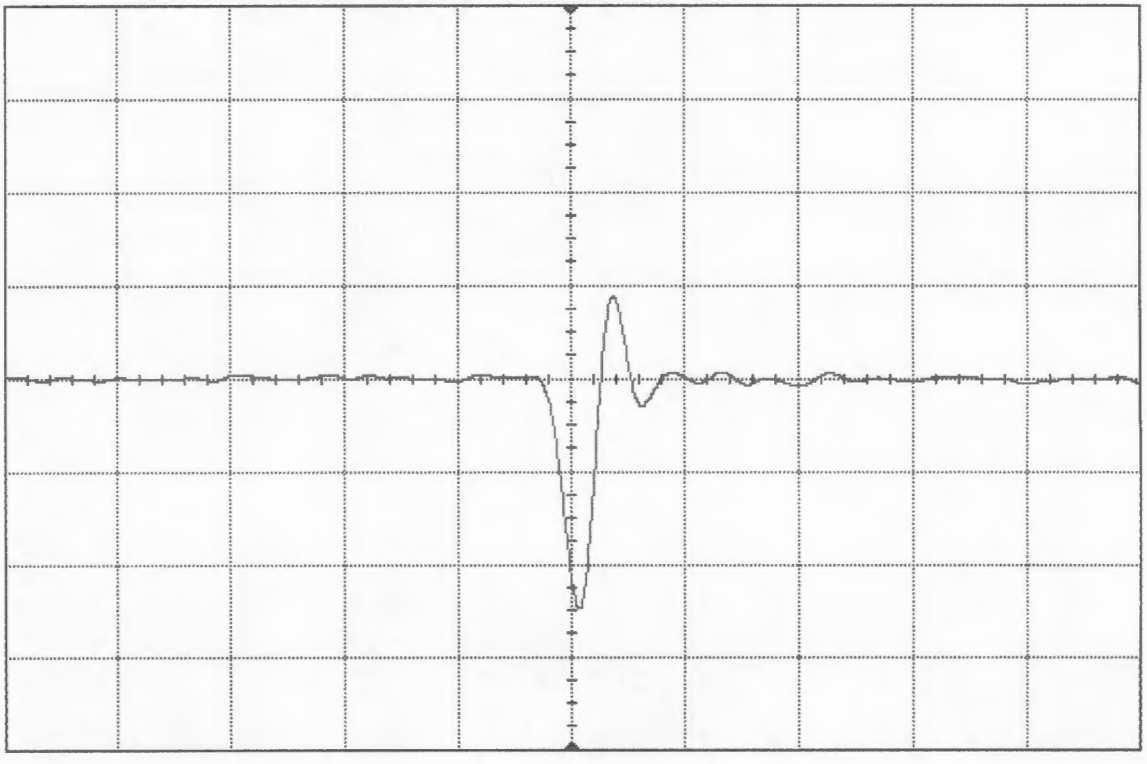

Figure 4.16: The measured waveform generated by BFR91A.
Vertical (voltage) scale 500 mV / Offset 0.
Horizontal (time) scale 2 ns.

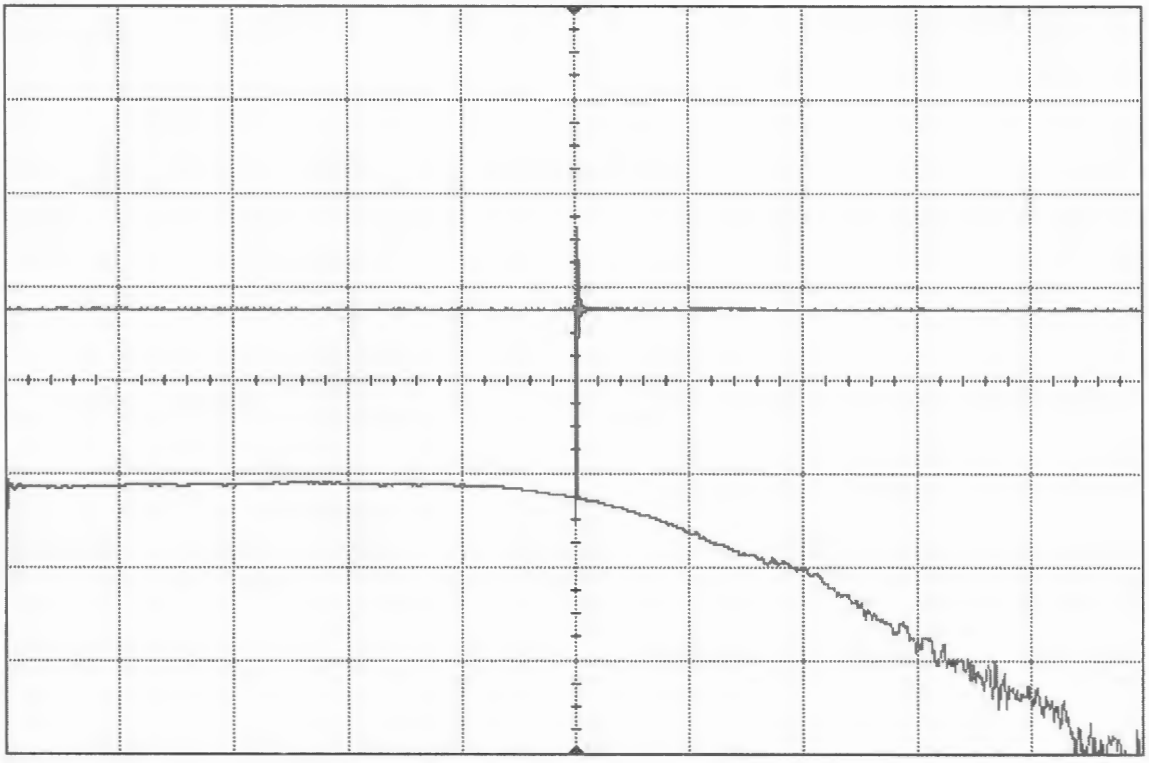

Figure 4.17: The measured waveform generated by BFR91A with DFT analysis beneath.
Vertical (voltage) scale 500 mV / Offset -379 mV.
DFT (wattage) scale 20 dBm / Offset -15 dBm.
Horizontal (time) scale 50 ns.
DFT (frequency) scale 200 MHz / Position 1 GHz.

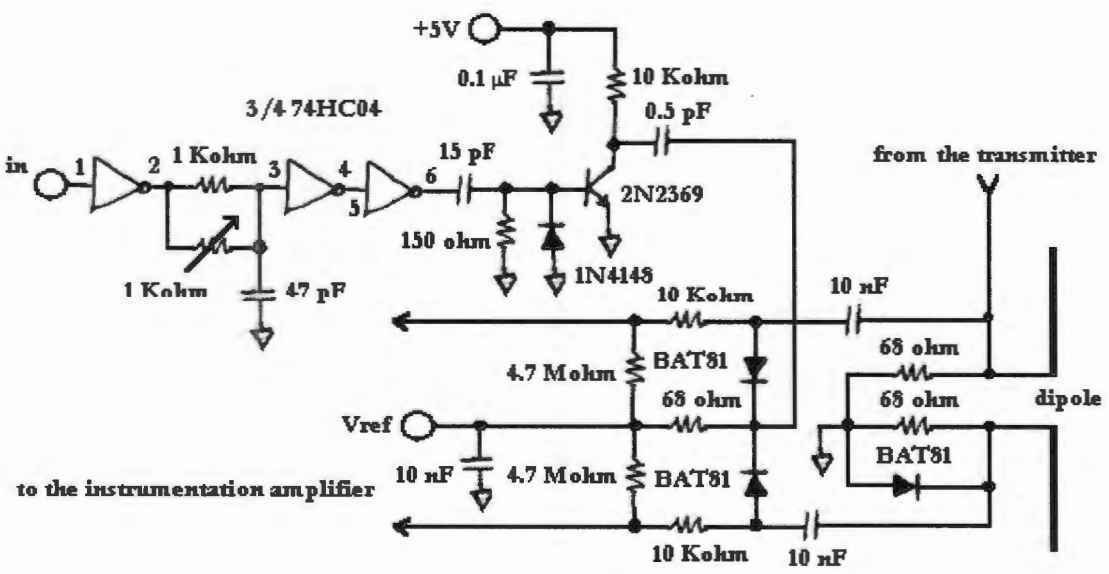


Figure 4.18: The delay line and the fast sampler connected to a balanced dipole antenna used in [47].

close to 30V as shown in the graph in Figure 4.20. The MV104 varicap diode has a typical diode capacitance temperature coefficient of 280ppm/°C which means the delay may be affected due to variations of the ambient temperature. This would be discussed further in section 7.9 of Chapter 7.

A DAC voltage output from the NI-DAQ card is connected to the varicap diode via an inductor (AC choke) at the point labelled "*V1*" in Figure 4.19. Voltage V1 is varied in the range of 0.3V to 10V which provides a capacitance varying from 80pF to 25pF. Figure 4.21 shows a plot of the reverse voltages across the diode versus delay achieved for the computer-controlled variable delay line circuit. The delay ranges from 15.82ns (at 10V) to 93.73ns (at 0.3V) by measuring the phase difference between the input of U7 (the master clock) and the output of U8 in Figure 4.19. This total delay range $t_\delta = 93.73ns - 15.82ns = 77.91ns$ corresponds to the maximum operating range $R_O = \frac{ct_\delta}{2} = 11.68$ metres of the radar. The delay was measured using the Agilent Infinium 54833A oscilloscope.

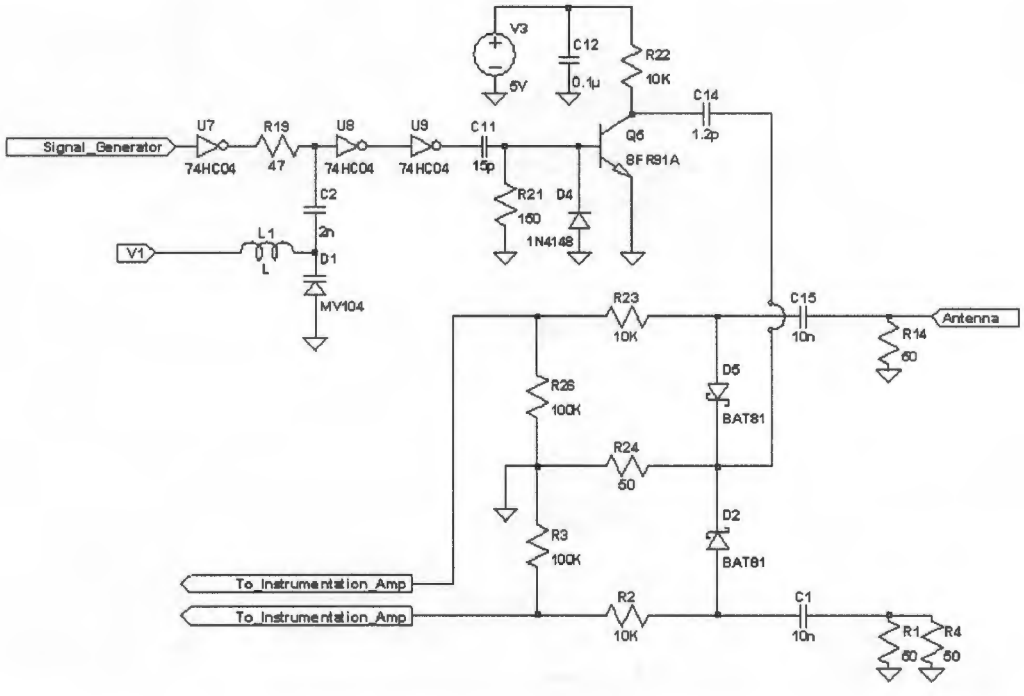


Figure 4.19: UCT UWB Radar Delay Line and Fast Sampler-Averager

The fast sampler-averager is triggered by the falling edge of a delayed negatively going pulse at node C14-D5-D2-R24 at the rate of the PRF. To explain the operation of the fast sampler-averager, each PRI can be decomposed into two phases: *triggered* (i.e. charging of capacitor C15 & C1), and *non-triggered* (i.e. discharging of C15 & C1). With reference to Figure 4.19, after the transmitted pulse is emitted, the triggered phase begins according to the delay being set, and it lasts a very short duration determined by $\tau_1 = R_{Sample}C = (Ra \parallel R14 \parallel R24 \parallel R1 \parallel R4) * C14 = 10\Omega * 1.2pF = 12ps$ where $Ra$ models the antenna load. Therefore, whenever the base of the transistor Q5 is triggered, a negatively going pulse pulls the node C14-D5-D2-R24 to -5V, which forces those two Schottky diodes D5 and D2 into conduction mode and produces -4.7V at nodes C15-D5-

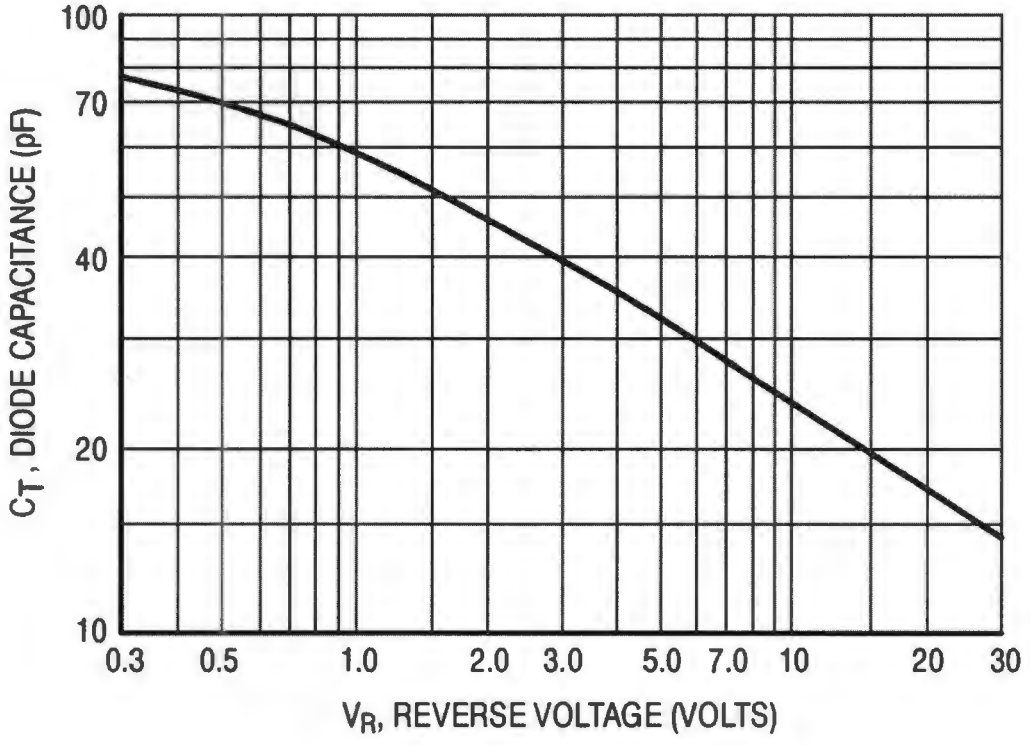


Figure 4.20: Reverse voltage v.s. capacitance of MV104.

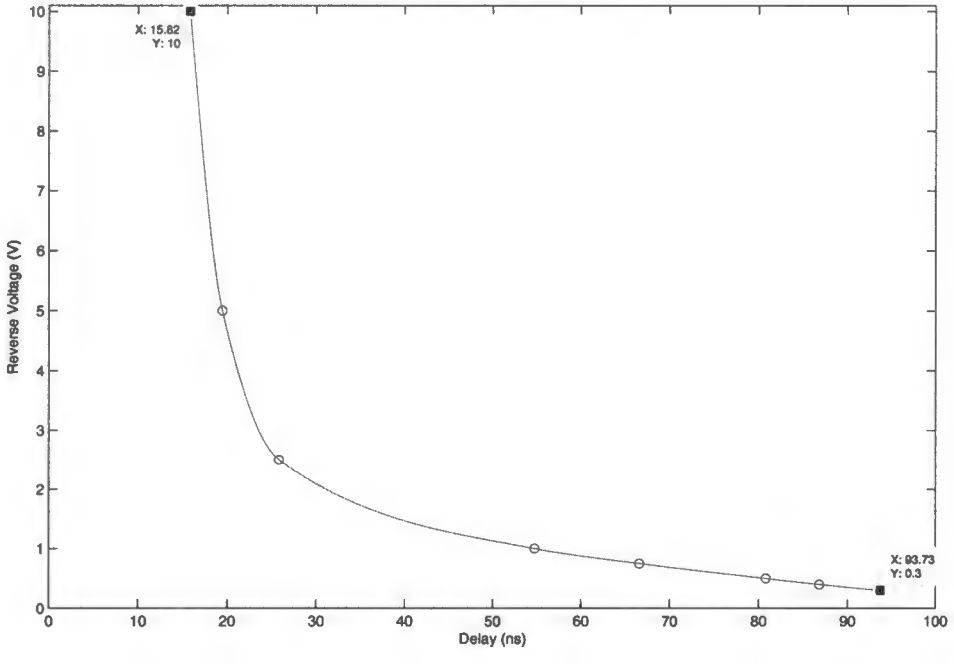


Figure 4.21: Voltage vs. Delay

R23 and C1-D2-R2. This, in turn, completes two sub-circuits CIRCUIT1 and CIRCUIT2 as shown in Figure 4.22 with their Thevenin equivalent circuits in Figure 4.23.

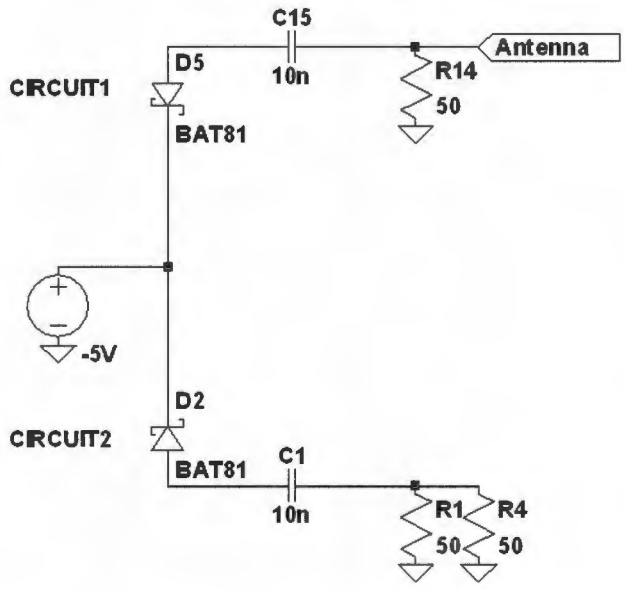


Figure 4.22: Sub-circuits CIRCUIT1 and CIRCUIT2.

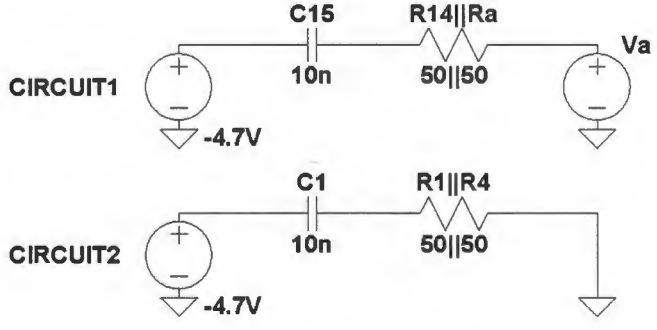


Figure 4.23: Thevenin equivalent circuits of CIRCUIT1 and CIRCUIT2.

In order for the fast sampler-averager to work correctly, it is assumed that voltages of the returned echoes are always higher than -4.7V which is always the case; being that voltages of the returned echoes are always in the mV range.

For the triggered phase, capacitor C15 is charged with potential difference between the antenna terminal and -4.7V as shown in CIRCUIT1 above. The current would flow from the antenna terminal towards -4.7V because the voltages of the returned echoes are more positive. The time constant for the capacitor to be charged to ≈63% full is $\tau_2 = R_{Charge}C = (50\Omega \parallel 50\Omega) * 10nF = 250ns$. Therefore it takes $\tau_2 \div \tau_1 \approx 20000$ pulses to do so. At PRI=500ns, $\tau_{Charge} = PRI * 20000 = 10ms$. This means that if voltage on the antenna terminal Va increases by $\Delta v$, the charge time constant for the capacitor is 10ms. We can call this the *active charge time*. Similarly, for CIRCUIT2, capacitor C1

will be charged to -4.7V after the *initial* active charge time has elapsed because $\triangle v$ in this case is always nil.

The rest of the PRI is the non-triggered phase, the diodes prevent currents from flowing through them thus they are considered open circuits, and capacitors C15 and C1 are discharged in the circuits shown in Figure 4.24 with their approximate Thevenin equivalent circuits in Figure 4.25 for computing capacitor discharge time.

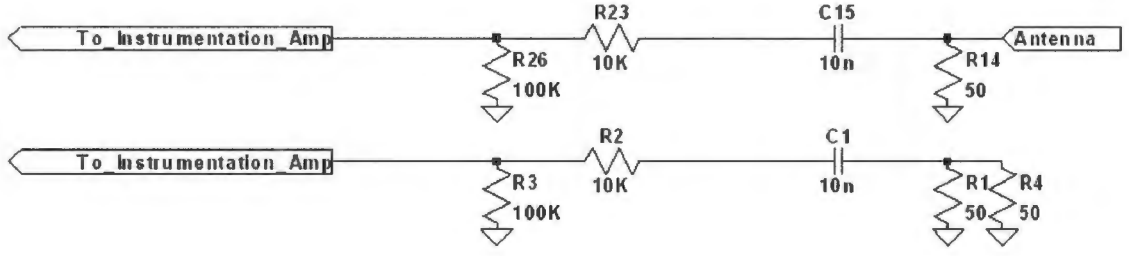


Figure 4.24: Discharging circuits.

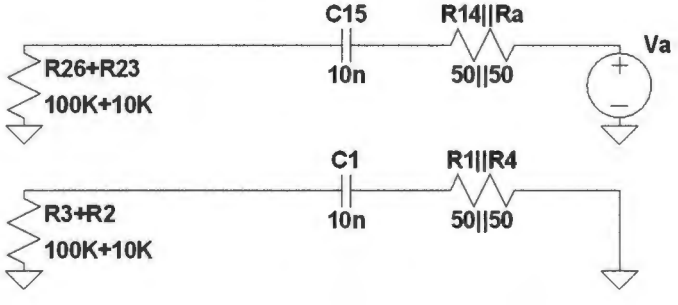


Figure 4.25: Thevenin equivalent circuits for the discharging circuits in Figure 4.24.

For the discharging circuits, the time constant $\tau_{Discharge} = [R26 + R23 + (R_{Antenna} \parallel R1)] * C1 = [100k\Omega + 10k\Omega + (50\Omega \parallel 50\Omega)] * 10nF \approx 1ms$. This means that if Va decreases by $\Delta v$, the discharge time constant for capacitor C15 is roughly 1ms. The time taken is called the *passive discharge time*. Capacitor C1 will not be discharged because there is no voltage difference across it. It will hold -4.7V which was charged during the triggered phase (active charging phase).

Therefore, the voltage fed into the instrumentation amplifier will be $-4.7V + V_{C15} \approx -5V + Va(t)$ and -4.7V for the upper and lower circuits respectively with $t$ being the delay set corresponding to the range $R$ where $R = \frac{ct}{2}$.

## 4.5 Post-Sampler Amplifier

In the circuits described in [47], the outputs of the fast sampler-averager in Figure 4.18 were connected to a back-end AC amplifier. It was designed as a motion detecting circuit for an alarm. A classic 3-op-amp instrumentation amplifier amplifies the difference signal (i.e. sampled antenna voltages). The resulting signal is then fed into a nulling circuit to remove effects from the stationary clutter. Lastly it is amplified by the final stage inverting amplifier. The design by [47] was a single-rail design with a virtual ground that equals half the supply voltage.

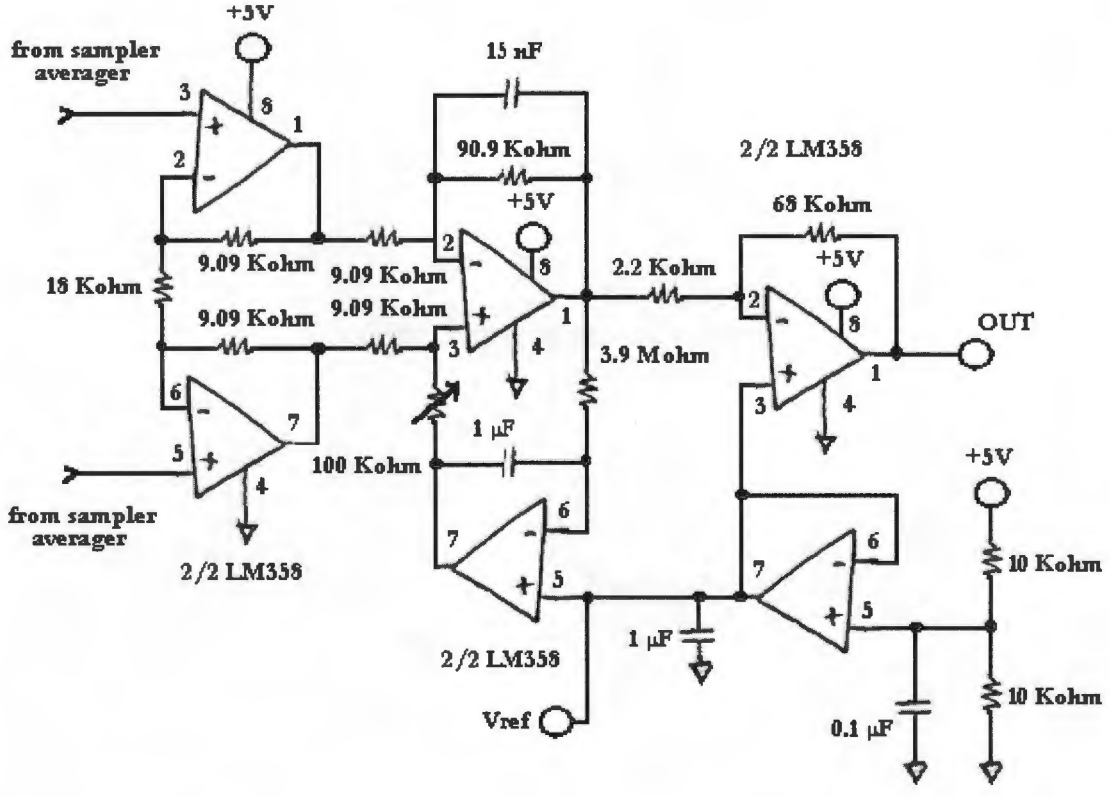


Figure 4.26: Post-Sampler Amplifier used in [47].

It is noted that according to [47], the rationale behind using three op-amp's, instead of a single instrumentation amplifier is due to cost. For our purposes of range profiling, we have a dual-rail design that uses a single precision instrumentation amplifier (AD620) with adjustable gain (1 to 1000) set by the variable resistor as shown in Figure 4.27. The simplified schematic of AD620 is shown in Figure 4.28 reproduced from the data sheet [2].

Low-pass filters made from the combinations of 1MΩ resistors and 1nF capacitors in

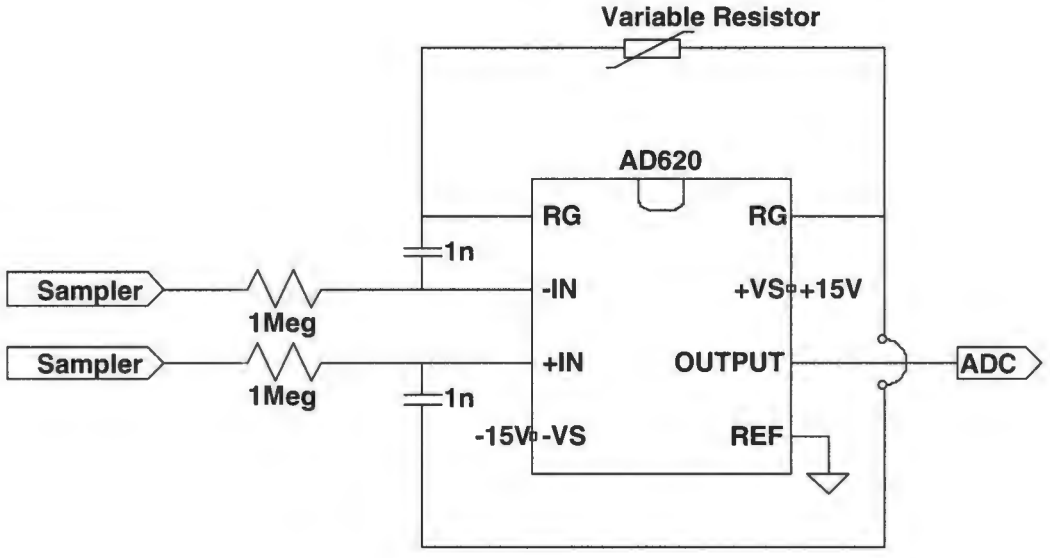


Figure 4.27: UCT UWB Post-Sampler Amplifier

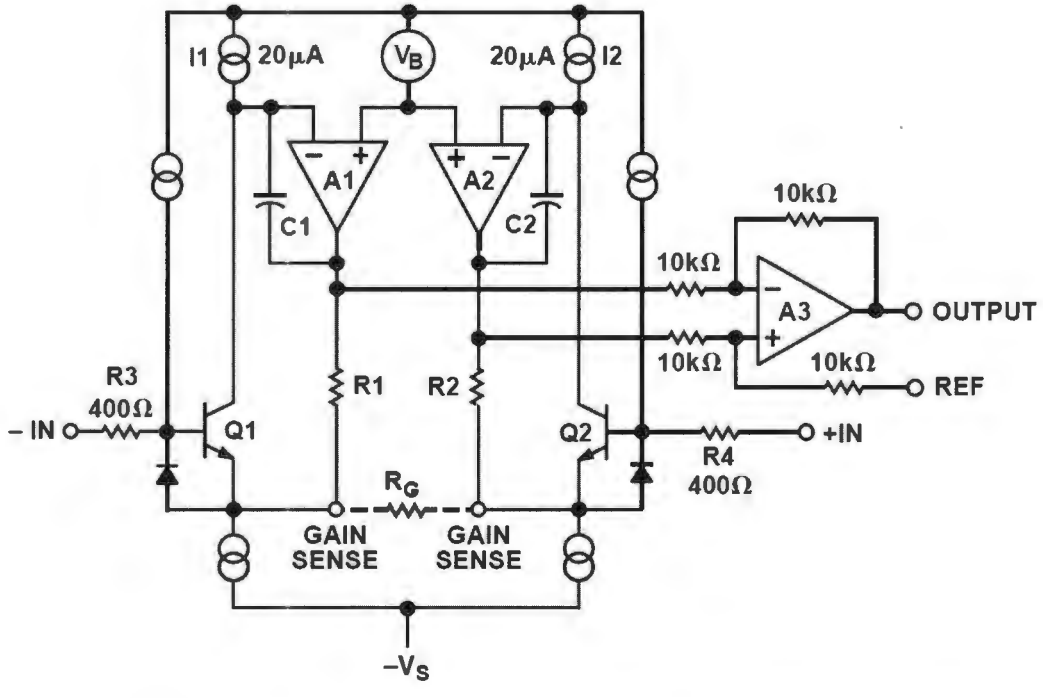


Figure 4.28: Simplified Schematic of AD620 reproduced from [2].

Figure 4.27 remove all RF components from the sampled signals that are fed into the instrumentation amplifier. With the values shown in the figure, the cut-off frequency is $f_c = \frac{1}{2\pi RC} = \frac{1}{2\pi * 1Meg\Omega * 1nF} \approx 160Hz$. They are also limiting the maximum sweeping rate which is discussed in section 7.10 of Chapter 7.

# Chapter 5

# System Integration

This section describes aspects the hardware modules that were used to implement the mono-static and bi-static UWB radar designs depicted in Figures 2.4 and 2.5 and how they are integrated into a computer system to produce down-range profiles.

## 5.1 RADAR Circuit

Figure 5.1 is a picture of the UCT UWB radar prototype (mono-static), containing the short pulse generator, the computer-controlled variable delay line, the integrating single-ended samplers and the low noise instrumentation amplifier. The components were soldered onto a PCB of size 7cm by 10 cm, with a ground plane on the top surface. The 2.0 MHz PRF signal generator and RF amplifiers were separate modules.

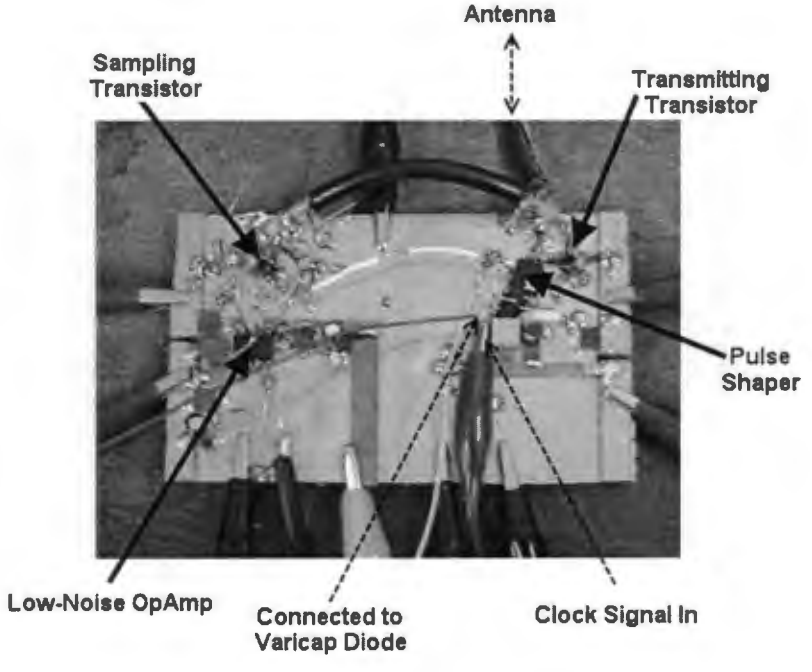


Figure 5.1: UCT UWB radar prototype (Mono-static)

## 5.2 NI-DAQ Card

The National Instrument Data Acquisition (NI-DAQ) card PCI-MIO-16E-1 (PCI-6070E) in Figure 5.2 provides an interface between the computer and the radar circuit. It is a 12-bit, 1.25 MS/s (mega samples per second) input sampling rate, 16-single-ended-analogue-input (or 8-differential-analogue-input), 2-analogue-output at 1.0 MS/s, 8 digital-I/O, Multifunction DAQ. It provides varying voltages used to slide the range gate shown in Figure 2.4, while at the same time it also samples the voltage generated by the instrumentation amplifier which forms the down-range profile. The voltage range for both I/O is $\pm$10V.

According to the Nyquist theorem, if the highest frequency component $f_H = 2.0$ GHz, then the sample spacing of $\frac{c}{2f_H} = \frac{3*10^8 m}{2(2.0*10^9)} = 0.075m$ is required in the downrange profile [60]. For a maximum range of 5 metres, the down-range profile would contain 5/0.075=67 samples. Therefore, if we wish to sweep the whole range every 0.5 second, we would need sampling rate of at least 134 samples/sec. This is also the minimum output sampling rate; being that each D/A output voltage corresponds to a specific range bin. The NI-DAQ card easily fulfils this requirements. Although the required sampling rate is merely 134 samples/sec in both I/O, in the experiments conducted, both I/O were set to $f_{A/D} = f_{D/A} = 10$ KS/s. Setting the IO sampling rate to be identical may simplify the operation of the hardware simultaneous triggering of both IO.

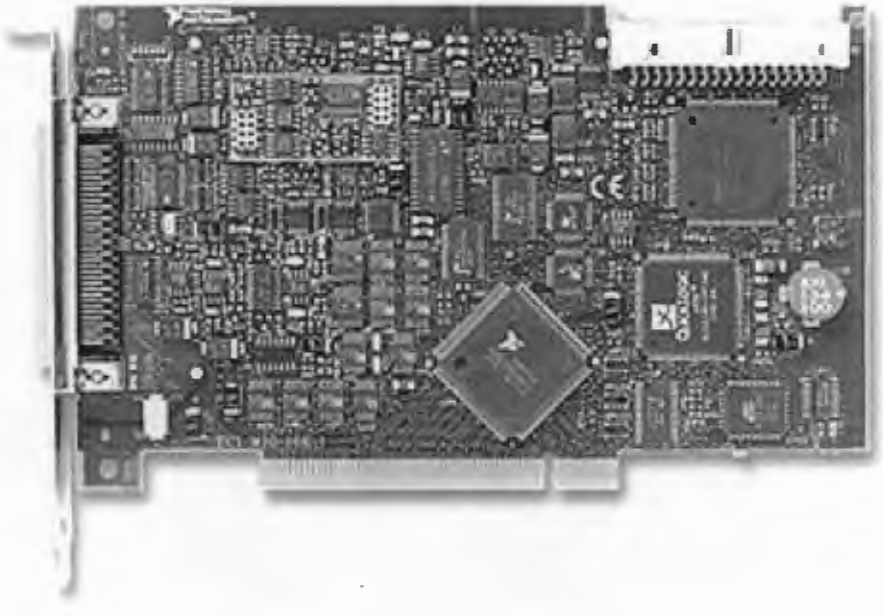

Figure 5.2: NI-DAQ

## 5.3 Front-End RF Amplifier

A front-end RF amplifier shown in Figure 5.3 which was developed by [59] can be fitted at the front end prior to the receiver in the bi-static configuration of Figure 2.5. It utilizes two stage amplification as shown in Figure 5.4. Its key characteristics are gain of 25dB at 1.5GHz with noise temperature $T_e \approx 400K$. Figure 5.5 and 5.7 shows its gain versus frequency range; Figure 5.6 and 5.8 shows its noise temperature versus frequency range. The amplifier was not ideal for this application as the gain response was not flat, and rolled off from about 600 MHz. It did however improve the SNR quite significantly in all experiments, and could be replaced by a more suitable amplifier module in the future.

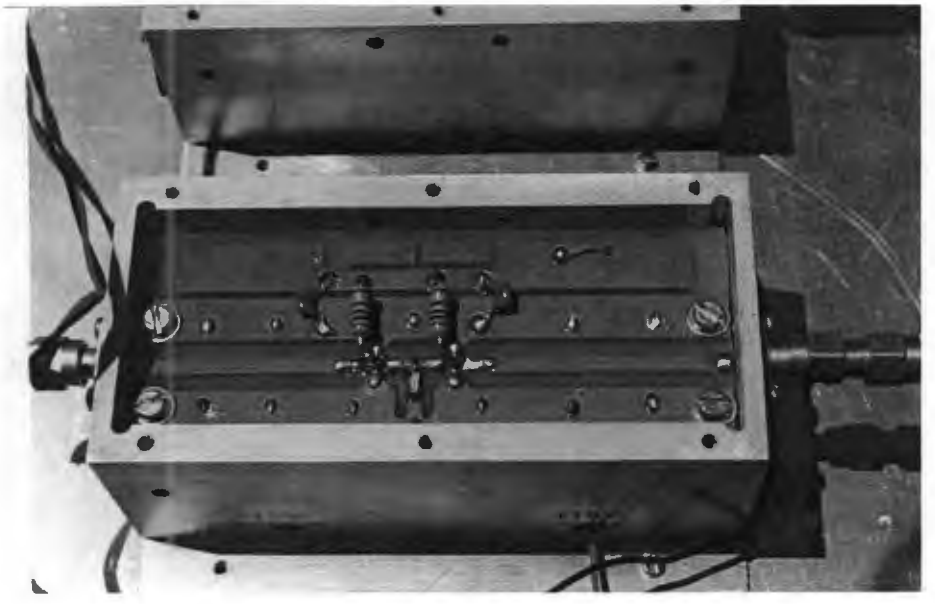

Figure 5.3: Front-End RF Amplifier

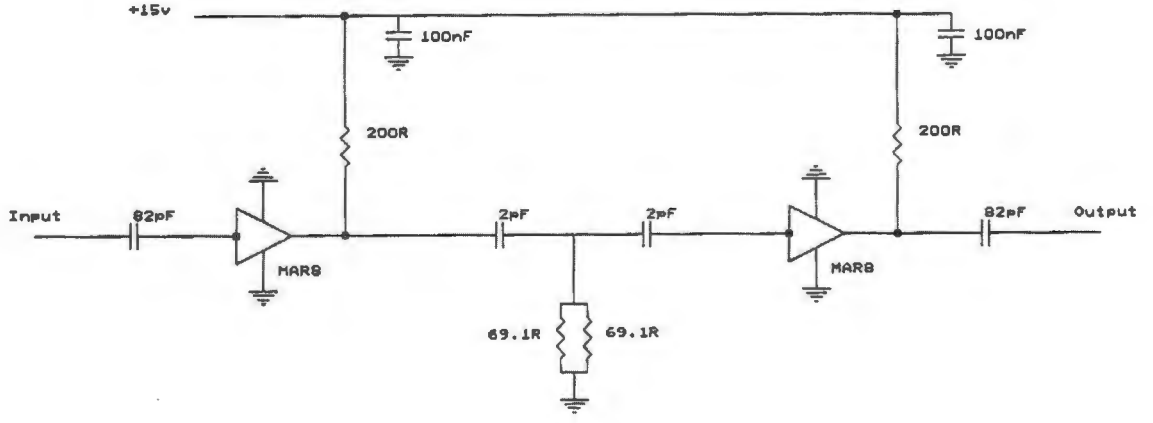


Figure 5.4: Two-Stage Amplification

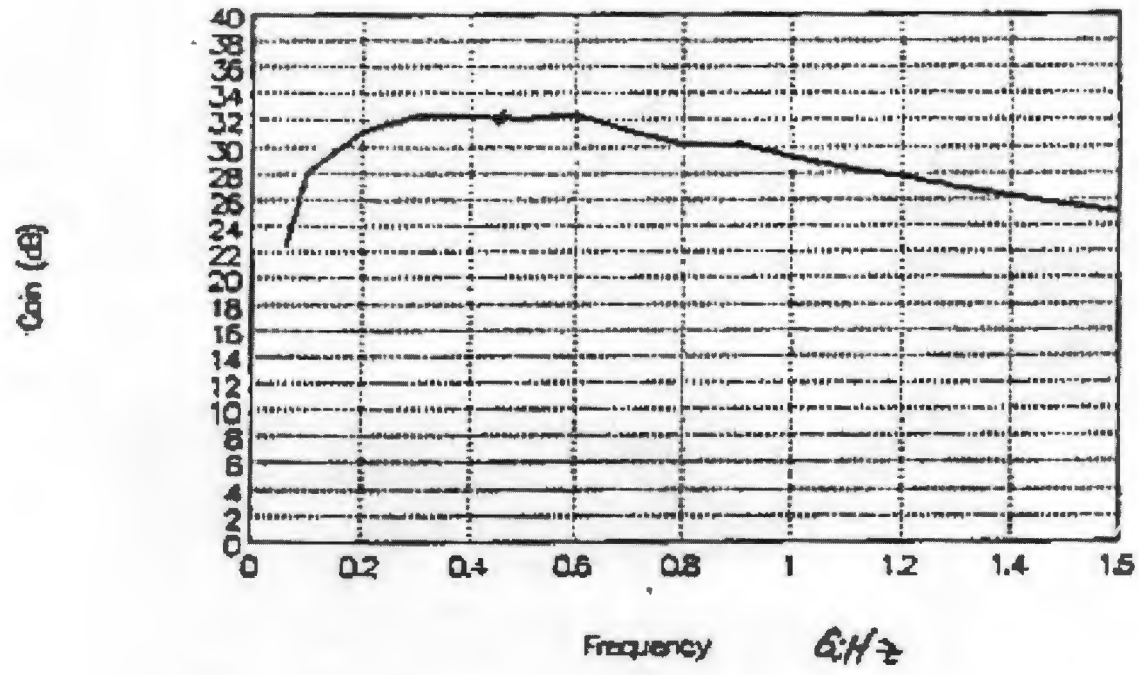


Figure 5.5: Gain vs Frequency Response(Gain in dB)

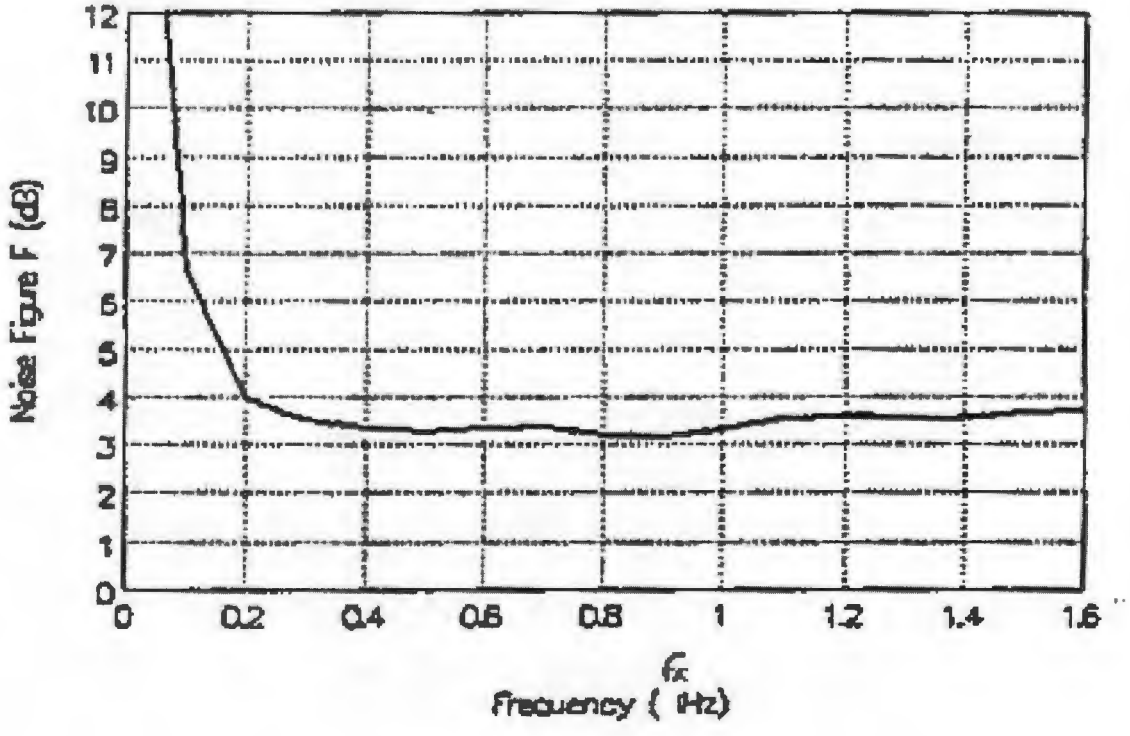


Figure 5.6: Noise Figure vs Frequency

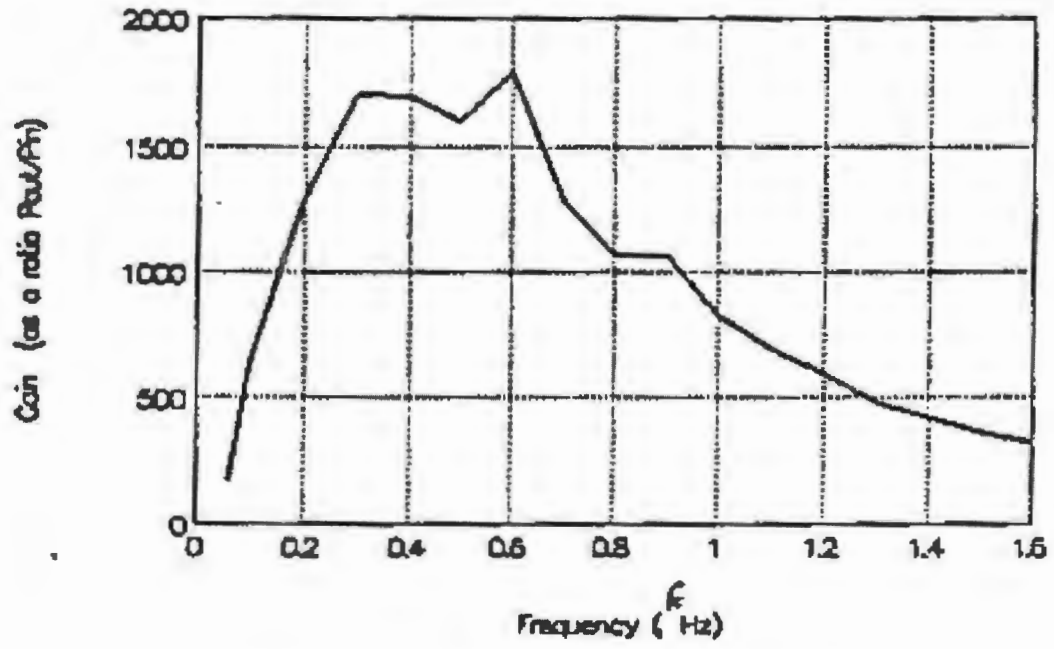


Figure 5.7: Gain vs Frequency Response(Gain in ratio)

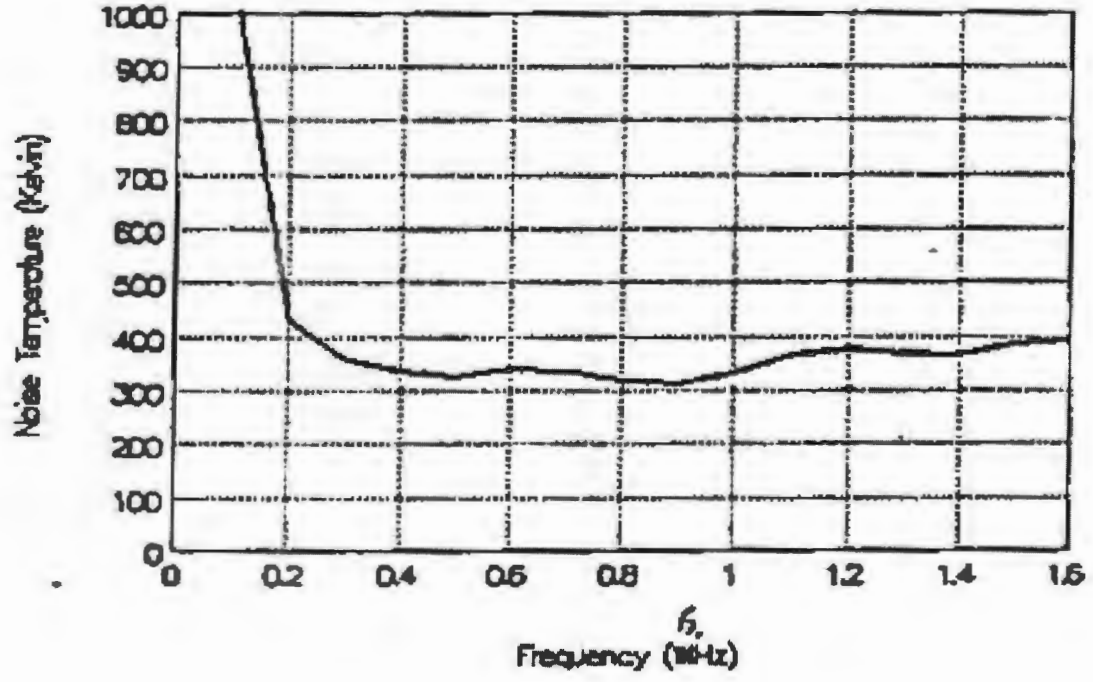


Figure 5.8: Noise Figure vs Frequency($T_e$ in Kelvin)

## 5.4 Antennas

Different kinds of antennas were examined. They are bow-tie antennas and grid antennas.These were not designed specifically for this project, but were readily available and offered broadband operation.

### 5.4.1 Bow-Tie Antennas

Experiments were carried out using bowtie antennas operating in two different frequency ranges:

- A GPR antenna made by [5] (see Figure 5.9). Its stated operating frequency is 50 - 400 MHz, corresponding to a fractional bandwidth off 155%.
- Two twin-bowtie antennas [45], designed to operate in L-band frequency range between 1 - 2 GHz. These are shown in Figures 5.10 and 5.11. These were built by an undergraduate thesis student in 2004, who reported the gain vs frequency characteristic, which we plotted in Figure 5.12 (for the twin-bowtie antenna with a flare angle smaller than 40°) and Figure 5.13 (for the twin-bowtie antenna with a flare angle wider than 40°). It is noted that the antennas resonates at 1.53 GHz as reported by [45].


Figure 5.9: GPR Antenna (50 - 400 MHz)

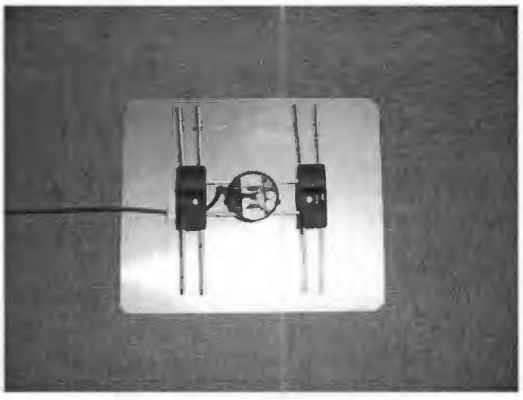

Figure 5.10: Twin-bowtie Antenna #1 (1 - 2 GHz) with a flare angle smaller than 40°made by [45].

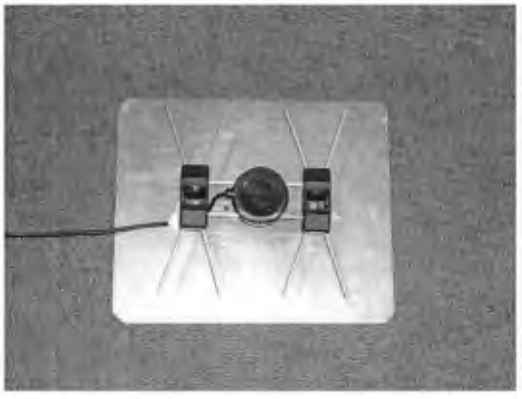

Figure 5.11: Twin-bowtie Antenna #2 (1 - 2 GHz) with a flare angle wider than 40°made by [45].

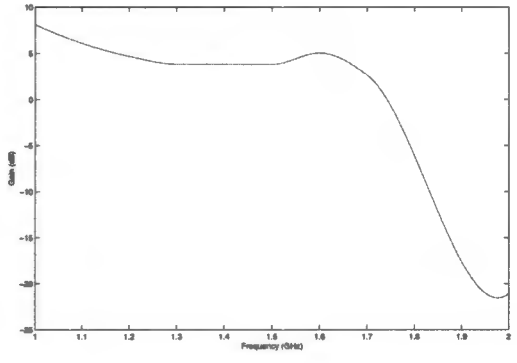

Figure 5.12: Plot of measured gain vs. frequency of the twin-bowtie antenna with a flare angle smaller than 40°as measured by [45].

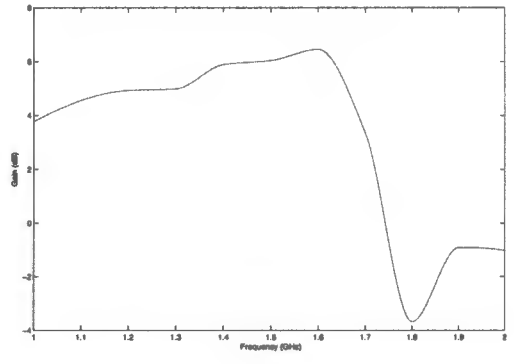

Figure 5.13: Plot of measured gain vs. frequency of the twin-bowtie antenna with a flare angle wider than 40°as measured by [45].

### 5.4.2 Grid Antennas

Three different TV grid antennas manufactured by Ellies Electronics were also tested [9, 10, 11]. Their specifications are shown in Table 5.1.

| Name | Freq. Range (MHz) | $\frac{2(f_H - f_L)}{f_H + f_L}$ | Gain (dB) | H. Beamwidth |
|---|---|---|---|---|
| Small Grid Aerial | 512 - 800 | 43.9% | 8 - 11 | 35° |
| Grid Aerial Red / Yellow | 512 - 704 | 31.6% | 12 - 14 | 30° |
| Grid Aerial | 512 - 800 | 43.9% | 10 - 13 | 32° |

(a) Small Grid Aerial

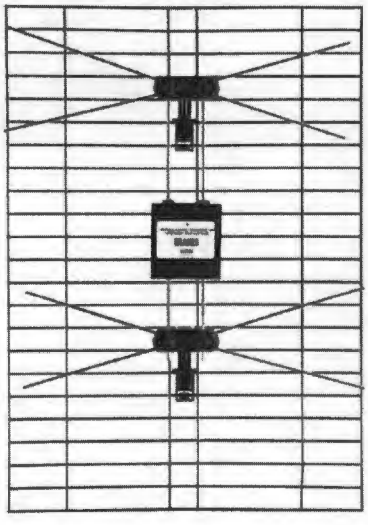

(b) Grid Aerial Red / Yellow

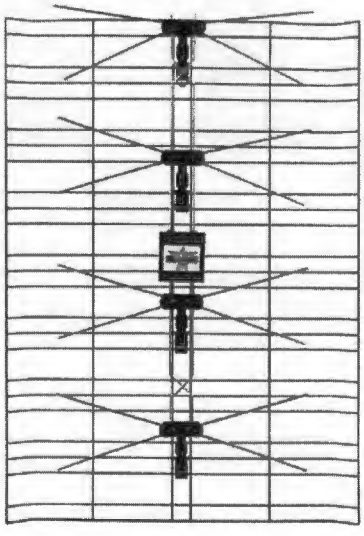

(c) Grid Aerial

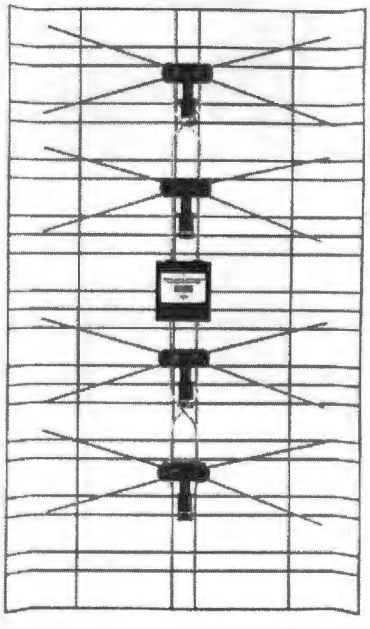

Table 5.1: Grid Antennas

# Chapter 6

# Software System

This chapter outlines the software aspects of the UCT UWB radar system including design, implementation and operation of the software. The software was built using MATLAB™Release 14 with the DAQ toolbox running on Windows XP™. An excerpt of the software code is included in Appendix A. Formula used to convert from sample space to distance (range) in metres is presented in the example of operating the radar included in this chapter.

## 6.1 Software Design

Figure 6.1 shows a block diagram of the software system and interfacing components. From the block diagram, two sub-systems are within the scope of this section, namely the Graphical-User-Interface (GUI) and the Digital-Signal-Processing (DSP) unit. The GUI is responsible of accepting user inputs to control the delay in the radar circuits via the data-acquisition system and feeding user-defined values to the DSP block. The DSP is responsible of processing the acquired data with user-defined values, and displaying results in the Display.

## 6.2 Software Implementation

A multi-threaded system is needed for displaying the down-range profile in real time. Fortunately the NI-DAQ card used in this project is capable of not only simultaneous operations of its inputs and outputs modules; simultaneous triggering (a hardware feature) of input and output ensures that data is captured synchronously with varying the output voltage to control the delay line.

### 6.2.1 Graphical User Interface

An interface built in MATLAB's GUI development environment (GUIDE™) is shown in Figure 6.2. It consists of a main display which displays current range profile data with its

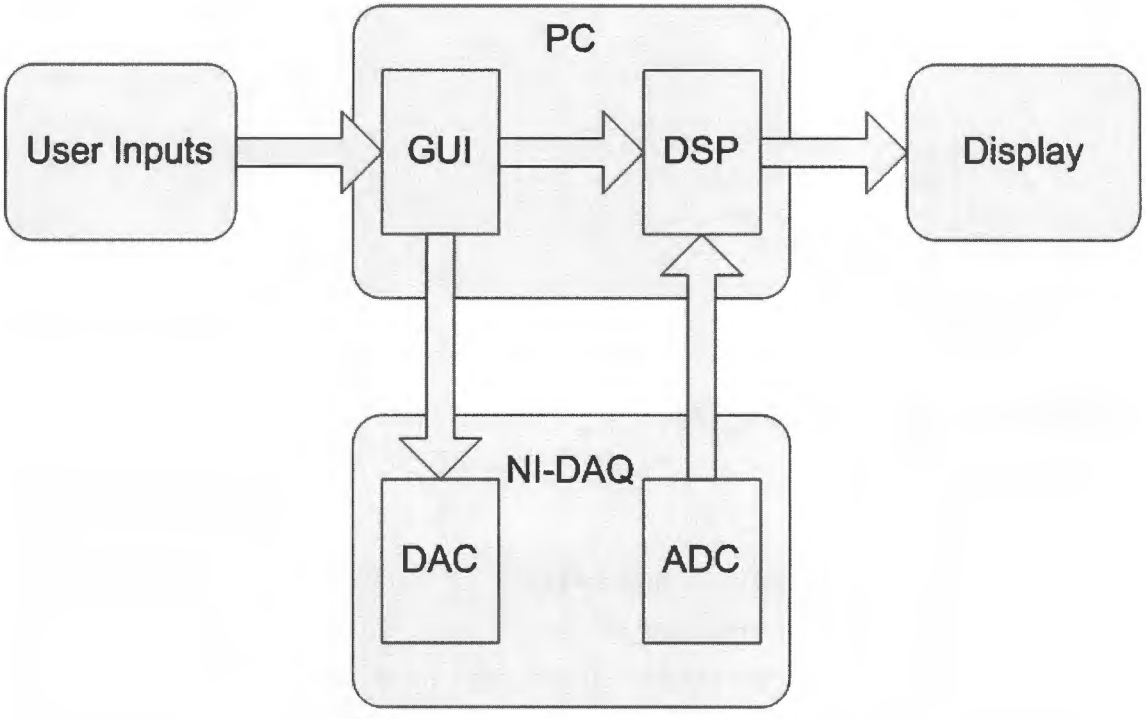


Figure 6.1: Software design.

FFT analysis beneath it.

The following GUI functionality were identified and implemented:

1. User controls:
   (a) Start the system.
   (b) Stop the system.
   (c) Take a background snapshot.
   (d) Take a filter snapshot.
   (e) Save the current plot displayed.
2. User-defined values:
   (a) Sweeping period/rate.
   (b) PRF (Pulse-Repetition-Frequency).
   (c) Band of interests - minimum and maximum frequency range.
   (d) Display scale -minimum and maximum voltage displayed.
3. User choices:
   (a) Display mode.
   (b) Filter type.

The controls for these features can be seen on the right-hand side of Figure 6.2.

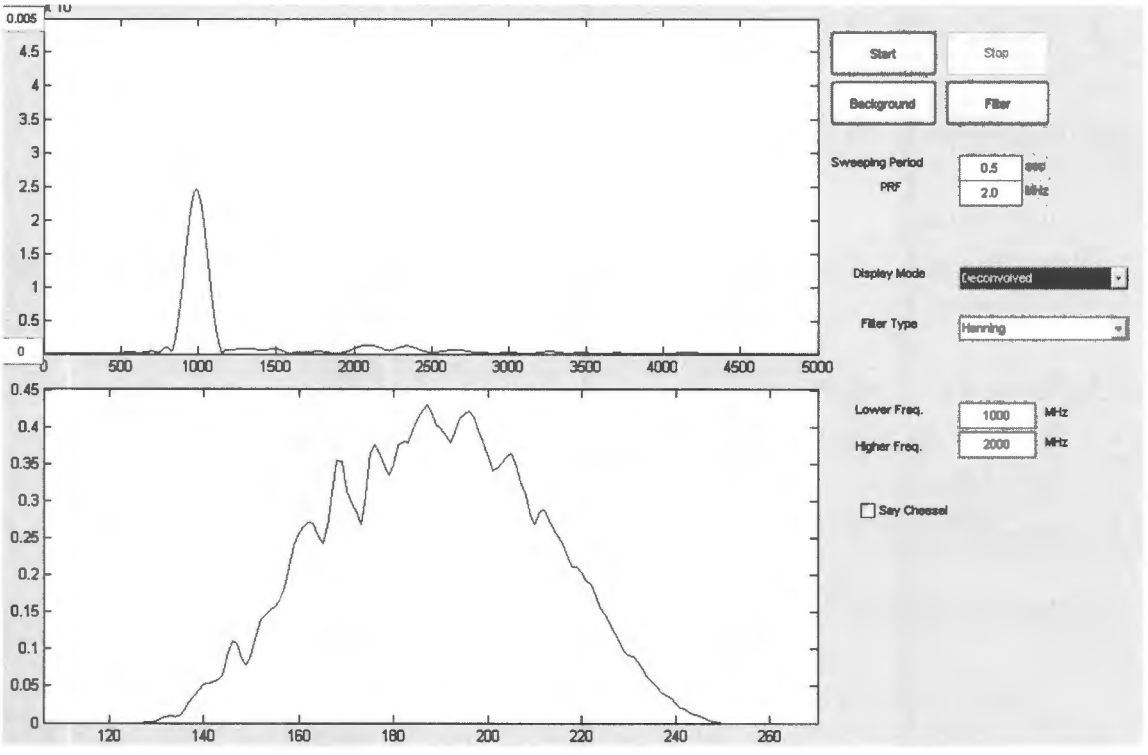


Figure 6.2: Software Interface

### 6.2.2 Digital Signal Processing

Corresponding to different displaying modes and window filter type (for range side-lobes suppression discussed in Chapter 3) selectable by the user, the following options are provided:

1. Display mode:
   (a) Raw - unprocessed captured data.
   (b) Background - snapshot taken with a stationary scene.
   (c) Difference - current captured data minus the background.
   (d) Filter - snapshot taken with a point-like target with background removed.
   (e) Matched - current captured data with background removed and passed through a matched filter.
   (f) Deconvolved - current captured data with background removed and deconvolved with the filter snapshot.
   (g) Envelope - current captured data with background removed and passed through an envelope detector.
2. Filter type:
   (a) Hanning window.
   (b) Hamming window.
   (c) Blackman window.

## 6.3 Software Operation

Operating the UCT UWB radar system involves:

1. Initial set-up:
   The user must choose the sweep period $T_{sweep}$ (seconds per sweep) prior to operation. The default value is 0.5 second per sweep.

2. Background clutter acquisition:
   The user sets up a stationary scene in front of the radar, then clicks on **Background** button. Ten down-range profiles are averaged to generate the source of background-removal.

3. Point-target calibration:

   (a) The user places a calibration target (several reflectors are shown in Table 7.1 of Chapter 7) in the scene at approximately 1.0 m in front of the radar, then clicks on **Filter** button to capture the scene's response with the background removed to generate the source of filtering.

   (b) Alternatively, the user can place the antennas about 2.0 m apart facing each other, then click on the **Filter** button to capture a perfect system response (as would be received from a perfect point target at range 1.0 m).

4. Real-time displaying of the down-range profile:
   The user can activate a real-time display of the down-range profile by clicking on the **Start** button. It will display different information according to the display mode chosen below.

5. Choosing the display mode:

   (a) **Raw**: In this mode, the down-range profile including the background clutter is displayed.

   (b) **Background**: Display a static down-range profile of the background clutter taken in Step 2.

   (c) **Difference**: Also known as background removal. It displays the current down-range profile with the background removed.

   (d) **Filter**: Display a static down-range profile of the point-target response recorded in Step 3.

   (e) **Matched**: In this mode, the matched filter is applied to the current down-range profile.

   (f) **Deconvolved**: The deconvolution filter is applied to the current down-range profile.

6. Choosing the filter type:

   (a) **None**.

   (b) **Hanning**.

   (c) **Hamming**.

   (d) **Blackman**.

7. Setting the band of interests:
   The user can choose a frequency band of interest by adjusting the **Lower Frequency** and **Higher Frequency** values.

### 6.3.1 Distance Conversion and an Example

In the following example, distance (range) has been converted from sample space to metres by using the formula $R = \frac{n}{T_{sweep} * f_{A/D}} * \frac{ct_\delta}{2} = \frac{n}{5000} * \frac{c*77.91ns}{2}$ where n denotes the number of the $n^{th}$ samples. A series of signal processing techniques [60] is applied to the raw returned echo to produce a set of results which can be usefully interpreted. The series is outlined as follows:

1. Figure 6.3 shows a background snapshot taken without any targets in the scene. This background will be subtracted in all the processes that follow.

2. Figure 6.4 shows a filter snapshot $f(t)$ taken when a calibration target (plate reflector *"Small Grid"* in Table 7.1) was placed at 1.0 m in front of the antennas (with background removed). The length of the captured filter response is set to 1000 samples in time (2.34 m in space). The rest of the samples are zero-padded.

3. Figure 6.5 shows the echo $v(t)$ (with background removed) from the same calibration target, which now is used as the intended target.

4. Figure 6.6 shows the echo $v(t)$ being filtered by matched filter with band of interest $\beta = 1.0 \sim 2.0$ GHz.

5. Figure 6.7 shows the echo $v(t)$ being filtered by deconvolution filter with band of interest $\beta$.

6. The final result in Figure 6.8 is obtained by applying a Hanning window to Figure 6.7.

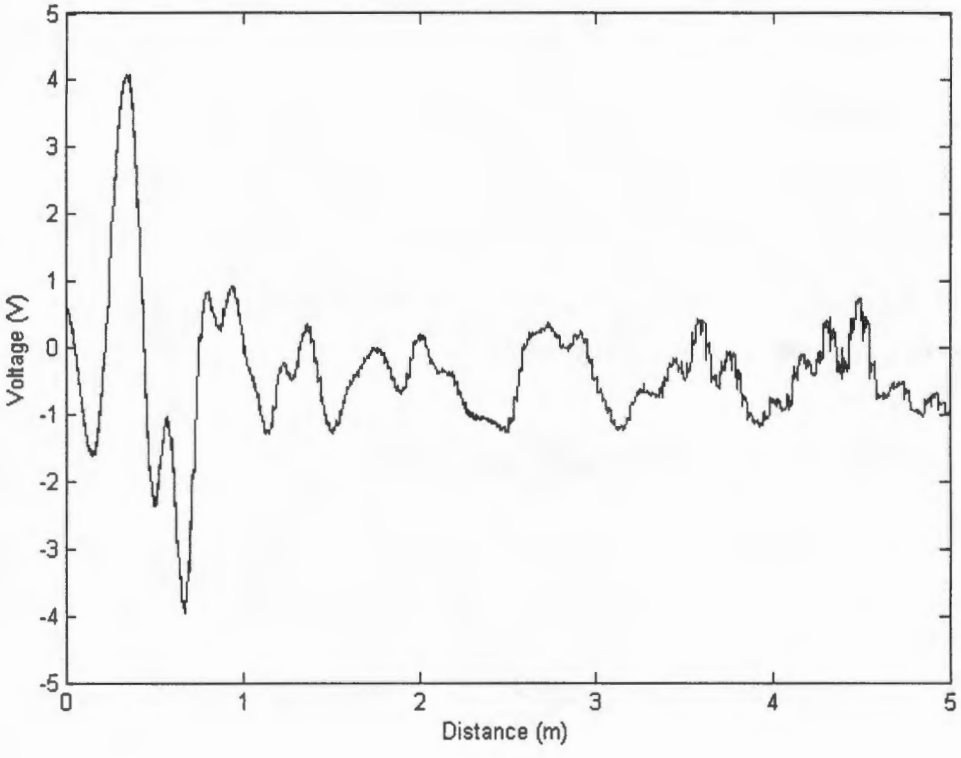


Figure 6.3: Background snapshot

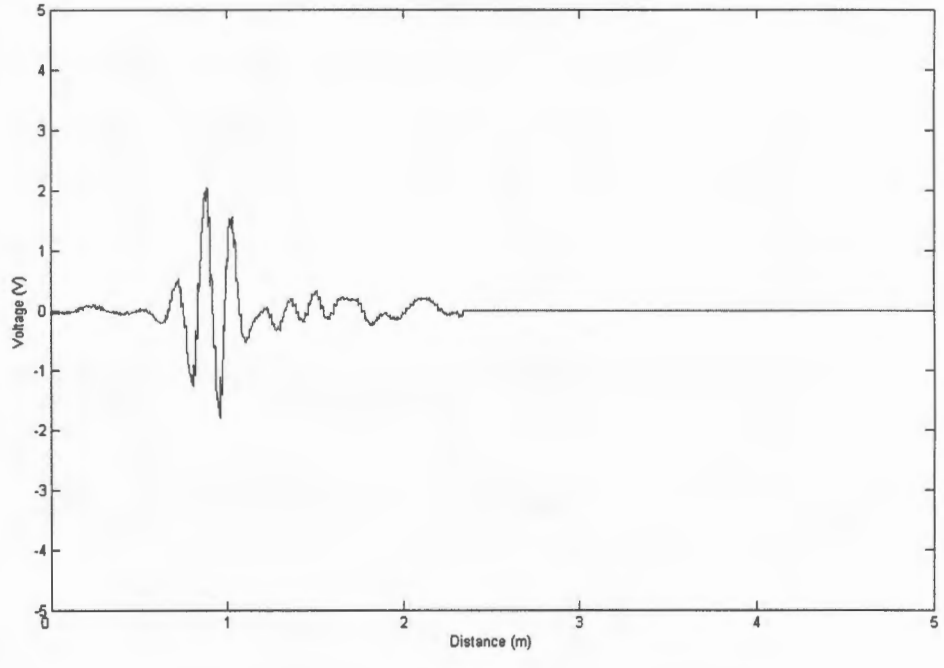


Figure 6.4: Echo from calibration target used to create deconvolution filter

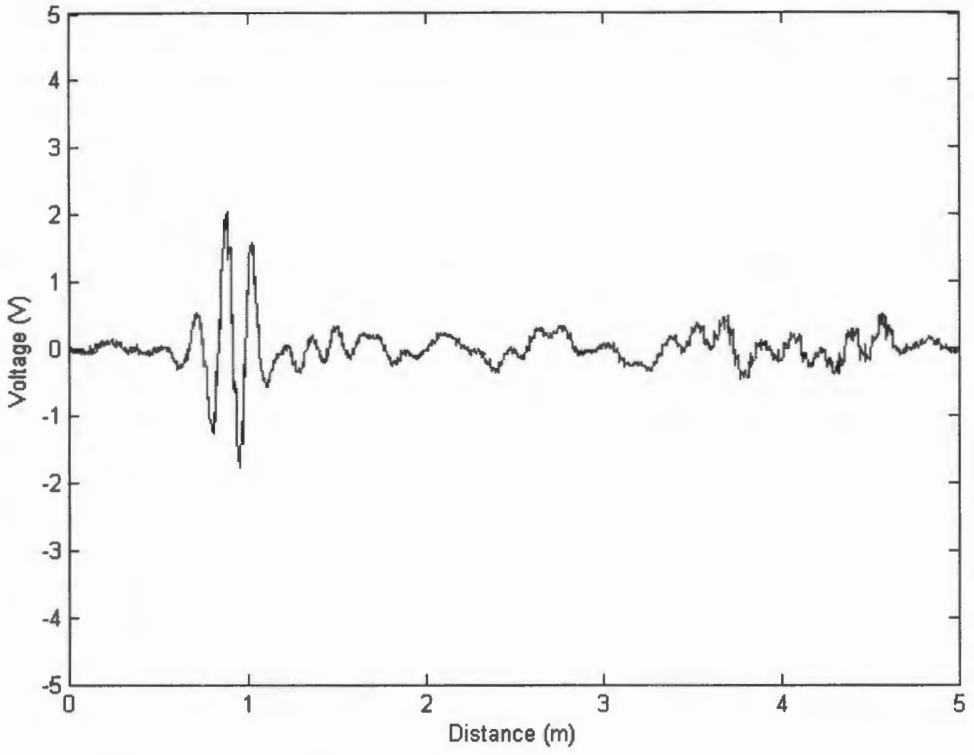


Figure 6.5: Unprocessed echo from a plate reflector

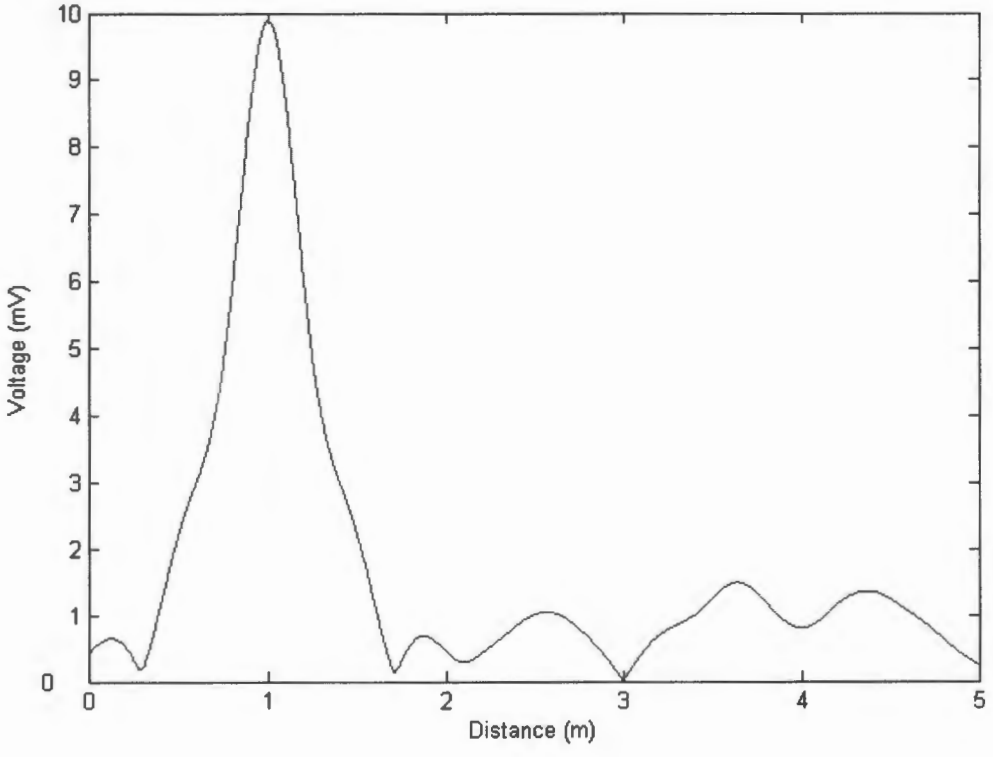


Figure 6.6: Match filtered with no windowing applied

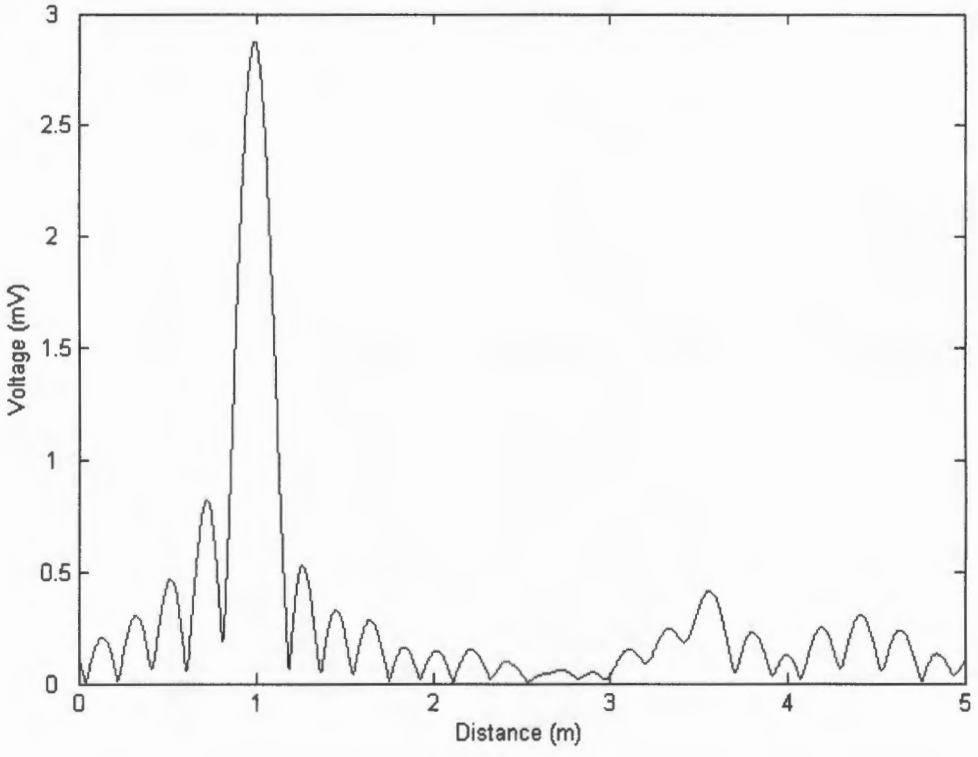


Figure 6.7: Deconvolution filtered with no windowing applied

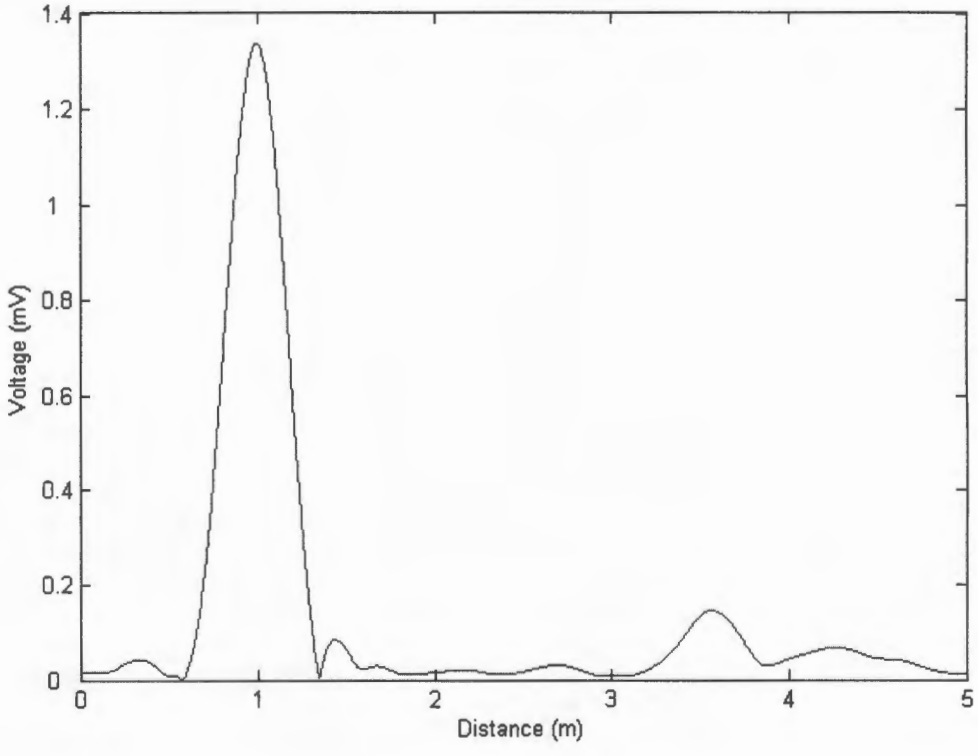


Figure 6.8: Deconvolved and Hanning windowed

# Chapter 7

# Results and Performance

This chapter discusses the performance of the UCT UWB radar system for range profiling. First the circuit performance is characterised, particularly achievable pulse width and bandwidth. Second the radiated bandwidth is discussed by characterizing the antennas used. Third the processed bandwidth, in other words the portion of the received bandwidth which is processed, and is directly related to the resolution presented to the users. Fourth the power radiated is discussed, centred on peak power and averaged power; followed by discussion on miniaturization of the circuit. Following that, the laboratory environment where the experiments took place is surveyed. Next various targets were placed in the scene to produce down-range profiles to demonstrate the capabilities of the system for detecting metal objects with and without obstacles. According to those down-range profiles, signal-to-noise ratios at different ranges are calculated and discussed. Last the maximum sweep rate achievable and maximum speed detectable by the system are discussed.

## 7.1 Achievable Pulse Bandwidth

The achievable pulse bandwidth of the UCT UWB radar system is estimated and verified by simulation using Switcher CAD III, direct measurements using the Agilent Infinium 54833A digital oscilloscope.

- The simulated pulse shown in Figure 4.15 has a 3dB bandwidth equal to 1.35GHz.
- Pulses captured by directly feeding the transmitter to the oscilloscope with input impedance of 50Ω shown in Figure 4.16 have usable spectral components from DC to 2 GHz as shown in Figure 4.17 while its measured 3dB bandwidth is 1.0GHz.

## 7.2 Limitations of Simple Antenna Structures

The performance is primarily determined by the antenna used because the antennas act as bandpass filters in the system; provided the pulse generated has spectral components

which cover the operating frequency band of the antenna. Testing was carried out with the various antennas described in section 5.4.

According to [5], the bowtie antenna functions over 50-400MHz band which is equivalent to 350MHz bandwidth. Therefore a 3dB range resolution of 42.86cm is expected.

With Ellies UHF grid antennas with a stated bandwidth of 288MHz, the best 3dB range resolution achievable is 53.08cm.

For UCT twin-bowtie antennas, whose operating frequency range is 1.0GHz-2.0GHz, the 3dB range resolution is 15cm since its bandwidth is 1GHz.

## 7.3 Processed Bandwidth

The processed bandwidth is the difference of the higher frequency $f_H$ and lower frequency $f_L$ values entered in the GUI discussed in section 6.2.1 of Chapter 6. It is common to set those values within the operating frequency range of the antennas used because of the gain provided by the antennas used. However, this processed bandwidth can be larger than the designed operating frequency range of the antennas used.

By observing the down-range profile in Figure 6.7, a 3dB bandwidth of 917MHz is calculated. After applying Hanning window, the resulted down-range profile in Figure 6.8 has a 3dB bandwidth of 558MHz. This decrease of bandwidth due to the windowing is expected.

## 7.4 Peak Power Radiated

In theory, the peak instantaneous power may be computed from $P = \frac{V_0^2}{R}$ , where $V_0$ is the peak voltage driving an ideal antenna of with an input resistance of $R$ Ohms. With a supply voltage of 15V, $V_0 \approx 14.7V$ (the voltage to which the output 1.2 pf capacitor is charged, minus diode drop), and assuming an ideal antenna impedance of $R = 50\Omega$, the calculated peak transmitting power is 4.32W. In practice, this peak value would be diminished as a result of finite switching time, component losses and current limiting by the output transistor.

### 7.4.1 Simulation

Although in theory the peak transmitting power can be as large as 4.32W, because of the current limiting nature of the components built into the transistor model, the simulated peak power is merely 8.0mW calculated by observing the peak value in Figure 7.1.

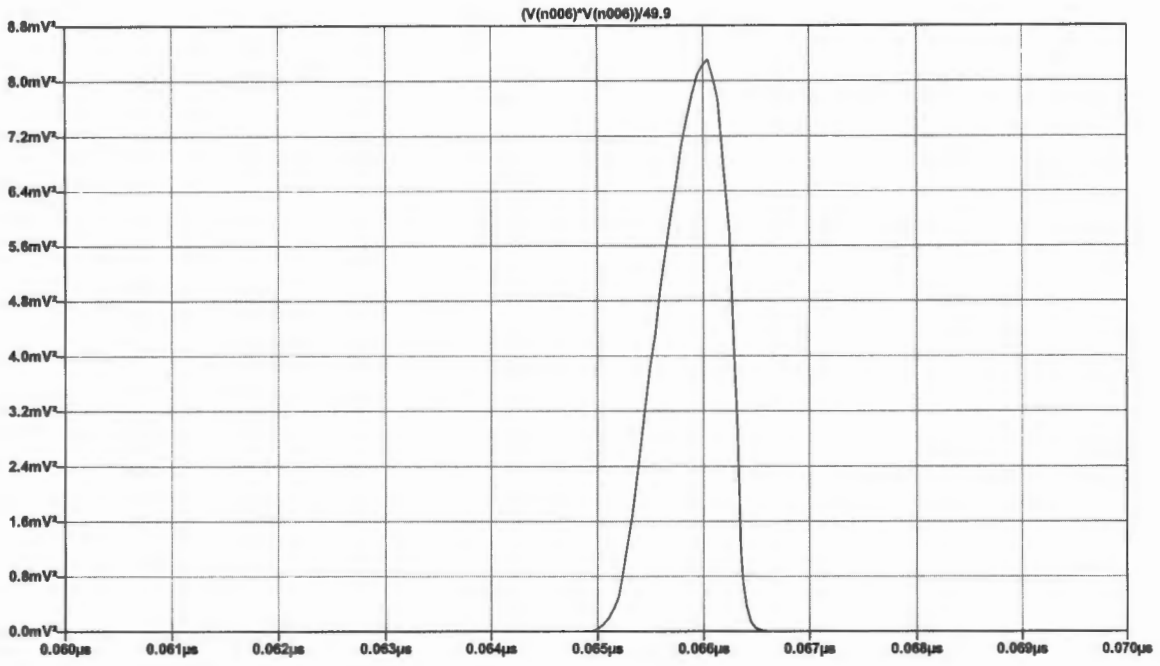


Figure 7.1: Instantaneous power of the simulated waveform of Figure 4.15.

### 7.4.2 Oscilloscope Measurement

The Agilent Infinium 54833A digital oscilloscope was used to observe the output voltage waveform, as developed across a 50Ω load. The resulting peak power of 31.9mW was observed from the peak value in Figure 7.2, again well below the theoretical maximum of 4.32W. It is however stressed that this is not a reliable method of measurement, as the rated bandwidth of the oscilloscope is only 1.0 GHz, which will limit the rise and fall time, and hence the observed peak is expected to be lower that which in fact is developed across a 50Ω load. Fourier analysis of the echoes captured by the prototype UWB radar showed significant spectral components beyond 2.0 GHz.

## 7.5 Averaged Power Radiated

The total power per pulse is calculated by integrating the area underneath the instantaneous power curve shown in Figure 7.2. The integration yields a value of 16.75pJ per pulse. With PRF of 2.0 MHz, the averaged power is then 16.75pJ * 2.0MHz = 33.5$\mu$W. Hence the title of this dissertation - *"A **Micropower** Ultra-Wideband RADAR Profiling System."*

It is stressed, however, that this is not an accurate measure of the power because of the bandwidth limitation of the oscilloscope.

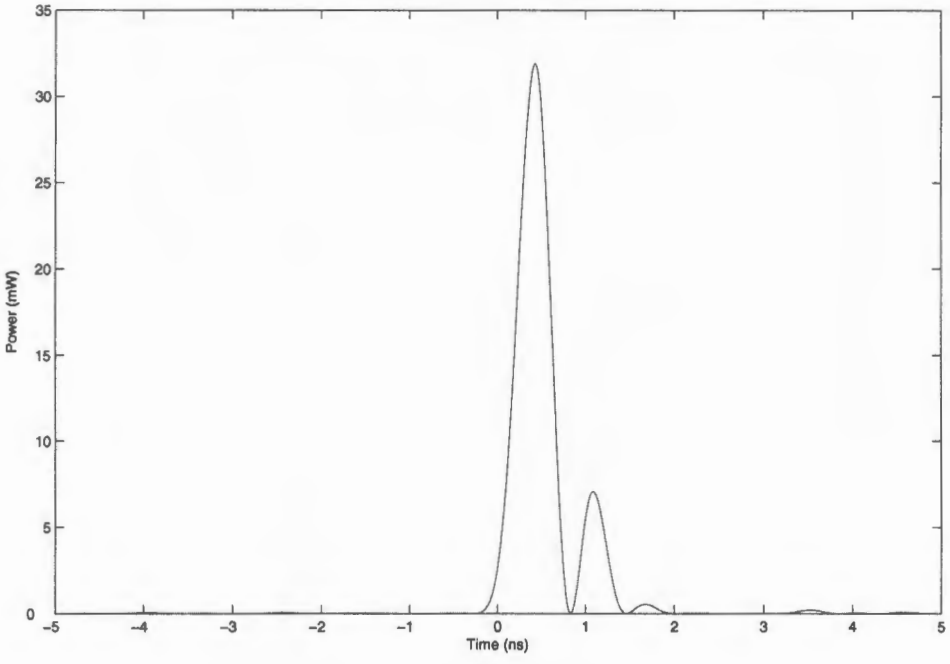


Figure 7.2: Instantaneous power across 50Ω of the pulse waveform captured in Figure 4.16. $P(t) = \frac{V(t)^2}{R}$.

## 7.6 Limitation of Indoor Measurements

Experiments were carried out in an laboratory shown in Figure 7.3. The twin-bowtie antennas can be seen aimed at a grid reflector. There exists a back wall at approximately 4.7 metres from the antennas and in front of the back wall, there are some furniture at 3.7 metres. They are all part of the background clutter. As one can notice in Figure 6.8, at 3.7 metres there exist some low-profiled targets; please note that these are not noise, but the effect due to the background clutter. The reason for this phenomenon is because the background clutter forms part of the background snapshot, therefore, when there is a target present, the background clutter will "appear" since the target now shields part of it. In the figures presented in section 7.7.2, as the target moves away from the antenna, this background clutter will gradually "sink" into the background as a target positioned further away shields a smaller portion of the background.

## 7.7 Capability for Detecting Metal Objects

The metal objects we tested are listed in Table 7.1.

Experiments were carried out using the the UCT UWB radar prototype in bi-static mode (as in Figure 2.5) with the UCT twin-bowtie antennas (shown in Figure 7.3). The antenna with the "V-shaped" elements (aligned at 40°) (as shown in Figure 5.11, and positioned on the left in Figure 7.3) was used for transmitting, while the other antenna with elements

| with a flare angle smaller than 40 | Photo | RCS Shape | Dimensions (mm) |
|---|---|---|---|
| Fan Mesh | 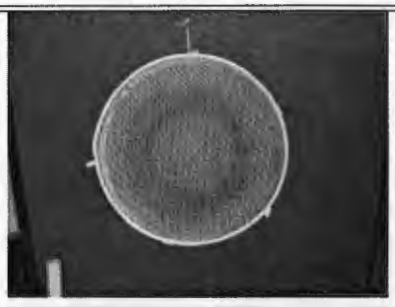 | Circle | 440 in Diameter |
| Small Grid |  | Rectangle | 550x390 |
| Large Grid | 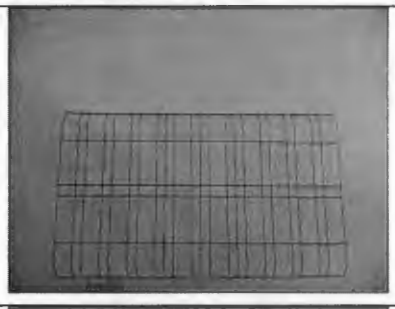 | Rectangle | 830x485 |
| Ball | 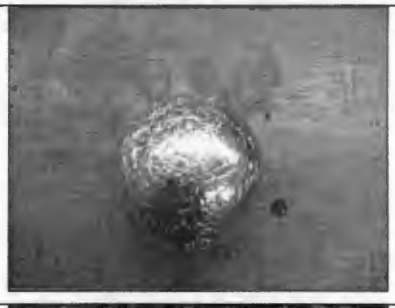 | Sphere | 55 in Radius |
| Corner Reflector |  | Pyramid | 500 per Side |

Table 7.1: Metal Objects Tested

Figure 7.3: Experiment Setup

aligned in parallel (as in Figure 5.10, and positioned on the right in Figure 7.3) were used for receiving. A metal sheet was placed between the two antennas to minimize direct-coupling between the TX and RX antennas, which may swamp the returned echoes.

The following results were obtained from a "Small Grid" as the target in various configurations with deconvolution filter set to 1~2 GHz and Hanning window applied. They are separated into two groups; one group has no RF amplifier (discussed in section 5.3) attached but is attached with a higher gain setting for the back-end amplifier (discussed in section 4.26); the other group has the RF amplifier attached with a lower gain setting for the back-end amplifier. The down-range profiles without RF amplification have not been converted to metres using the formula presented in section 6.3.1 to provide a comparison with the down-range profile with RF amplification which has been converted to metres.

It should be noted that the "Small Grid" target is only visible up to a range of about 1 m without a RF amplifier. If D denotes the maximum dimension of the antenna aperture, and $\lambda$ is the wavelength of the highest frequency component (2.0 GHz), then the far-field distance $R_{far-field} \geq \frac{2D^2}{\lambda} = \frac{2(0.25)^2}{0.15} \geq 0.833m$. With the RF amplifier attached, the antennas are thus operating in their far-fields because targets are now visible up to 5 metres within the laboratory.

### 7.7.1 Performance Without RF Amplifier

Figure 7.4 shows the echo from the "Small Grid" target at 50cm. Figure 7.5 represents the target at 80cm. This experiment was done using bow-tie antenna shown in Figure 5.10. These targets are visible up to only 1 metre (sample number 1000) in range. Returned echoes from targets further than 1 metre away rapidly diminish below the noise floor.

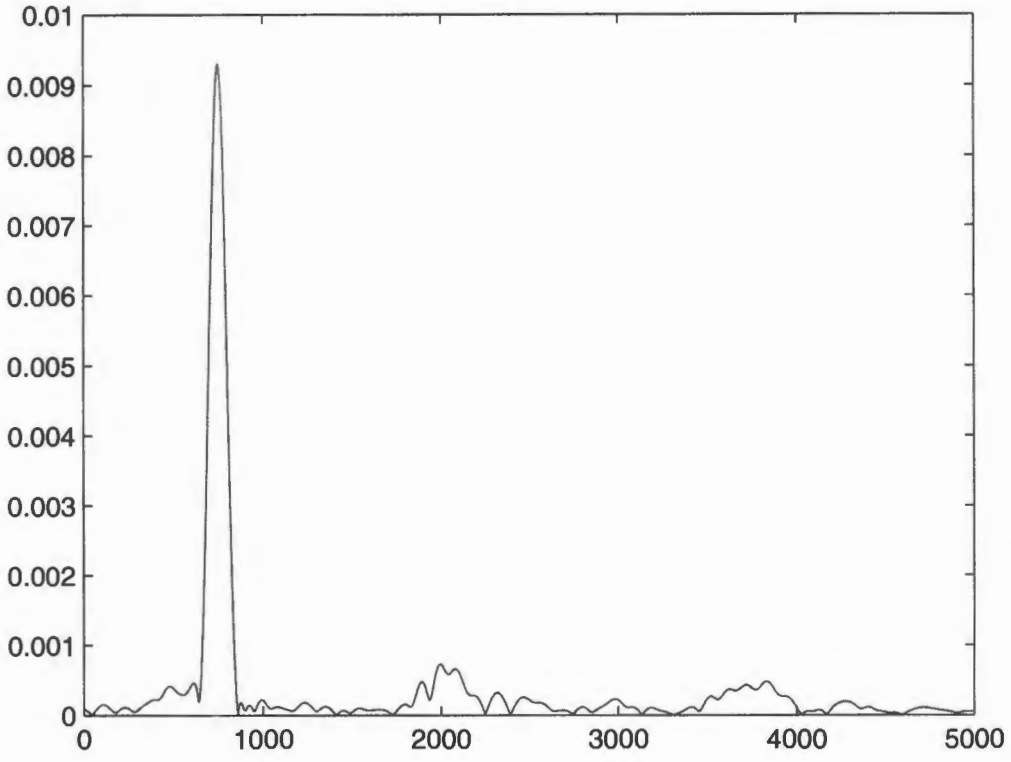


Figure 7.4: Target at 50cm without RF amplifier.X-axis: Sample (spans from -2.33m to 9.35m).Y-axis: Voltage (V).

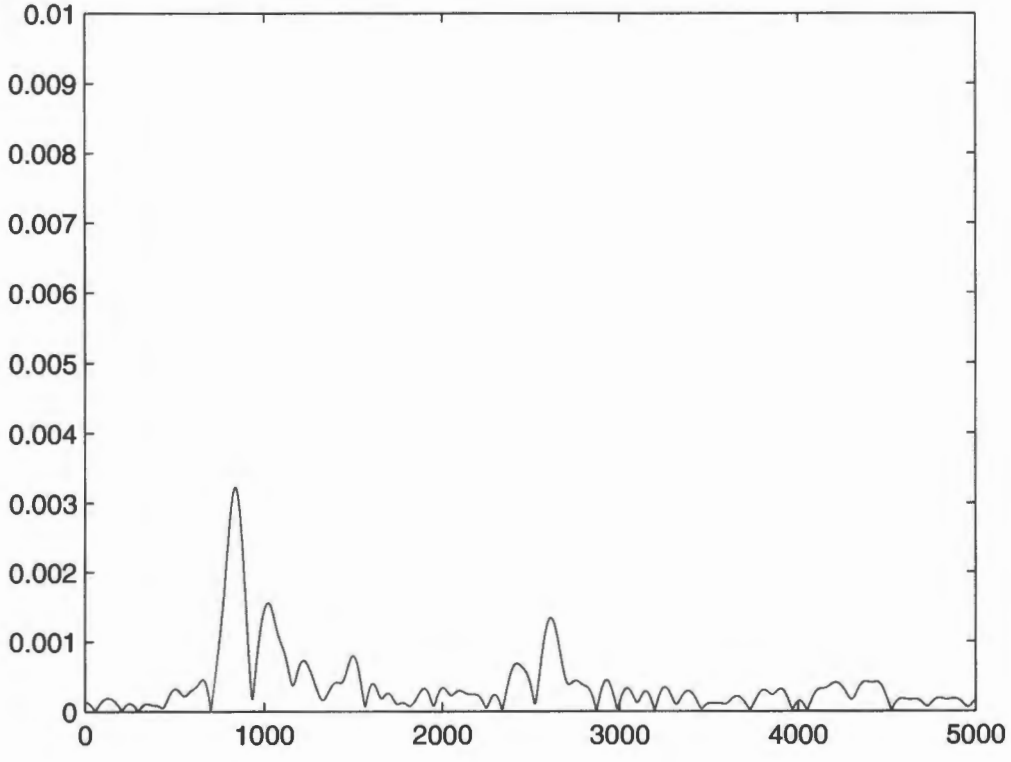


Figure 7.5: Target at 80cm without RF amplifier.X-axis: Sample (spans from -2.33m to 9.35m).Y-axis: Voltage (V).

### 7.7.2 Performance With RF Amplifier

We have much better results with the RF amplifier attached. Available range is estimated to be increased by 10 folds. The following figures are obtained using the twin bow-tie antennas with deconvolution filter set to 1 - 2 GHz range and Hanning window applied.

Figure 7.6 shows a scene without targets. Figure 7.7 shows the target at 1.0m, Figure 7.8 shows the target at 1.5m, Figure 7.9 shows it at 2.0m and Figure 7.10 shows the target at 2.5m, while a target at 3.0m is shown in Figure 7.11.

Multiple targets are shown in Figure 7.12 with the "Ball" target positioned at 1 metre and the "Small Grid" target positioned at 2.5 metres in the scene.

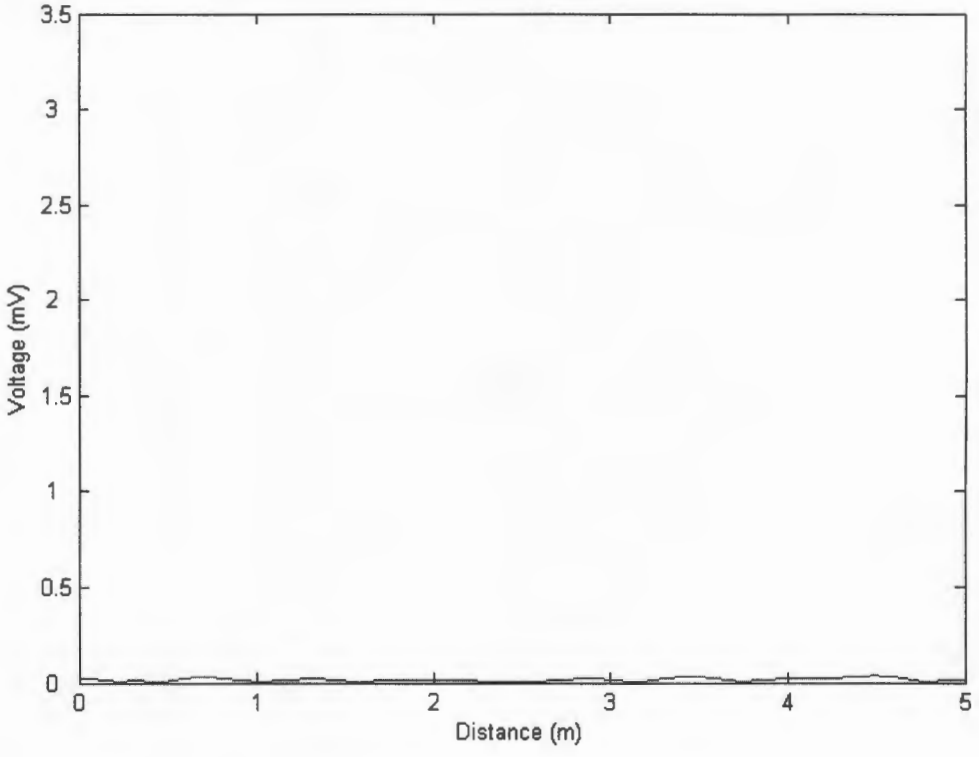


Figure 7.6: No Target with RF amplifier.

## 7.8 Detection through Obstacles

This sections represents results from detecting hidden targets being shielded by obstacles such as a partition or a cement wall. It is unfortunate that *"seeing-through-wall"* was only possible to pick up targets standing right next to the wall. Thus the results from were not recorded.

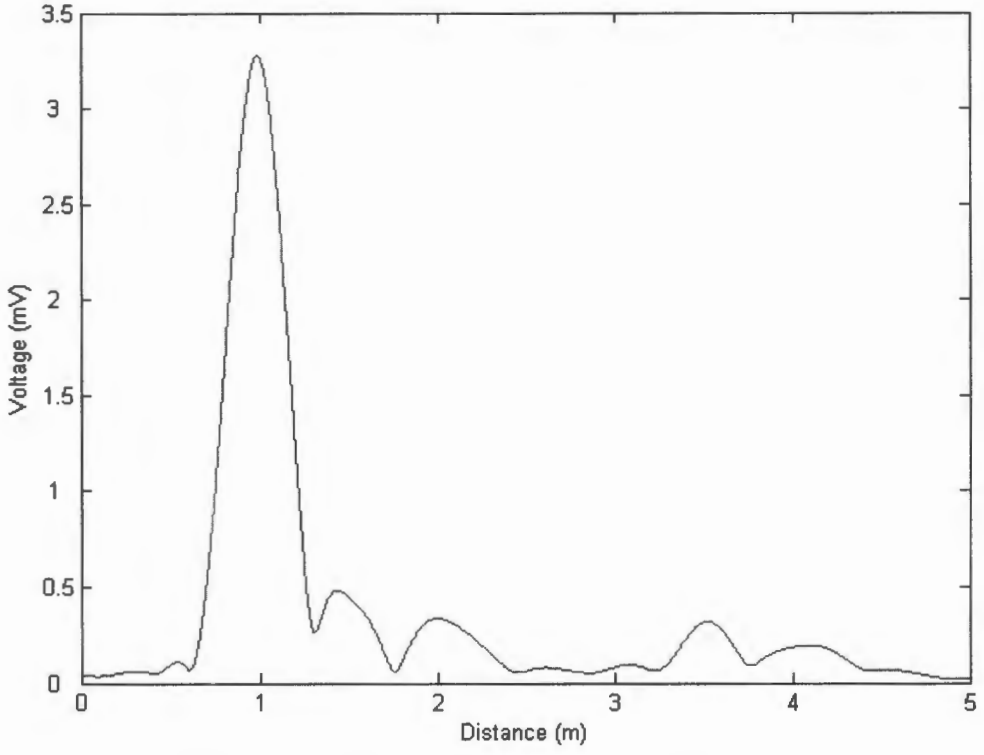


Figure 7.7: Target at 1.0m with RF amplifier.

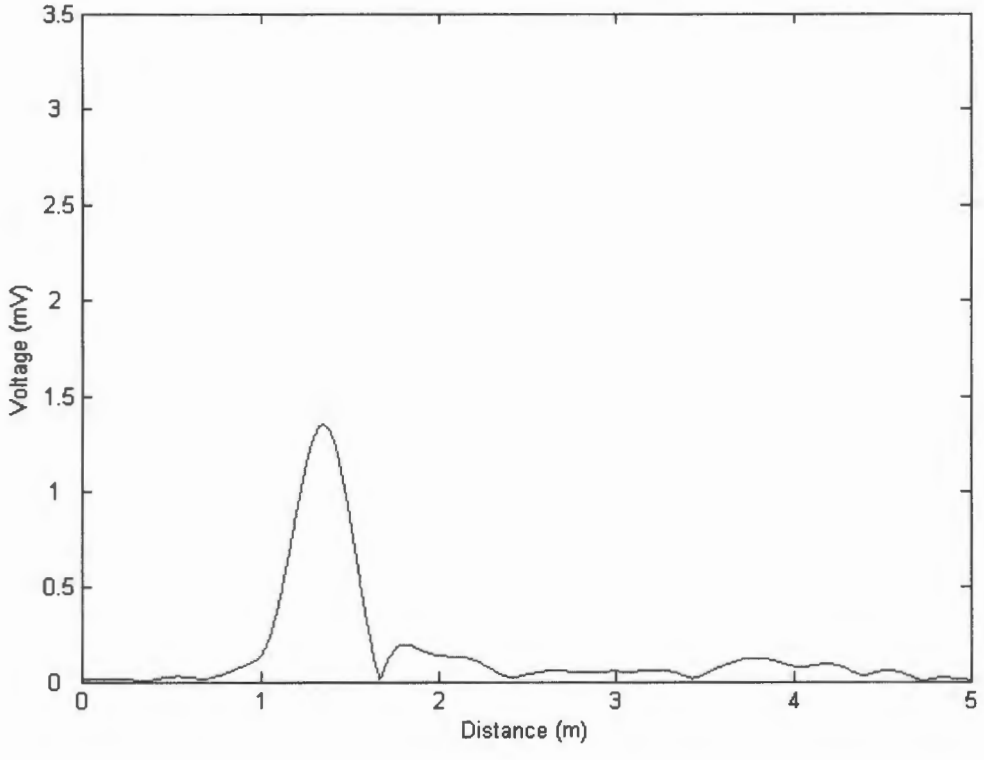


Figure 7.8: Target at 1.5m with RF amplifier.

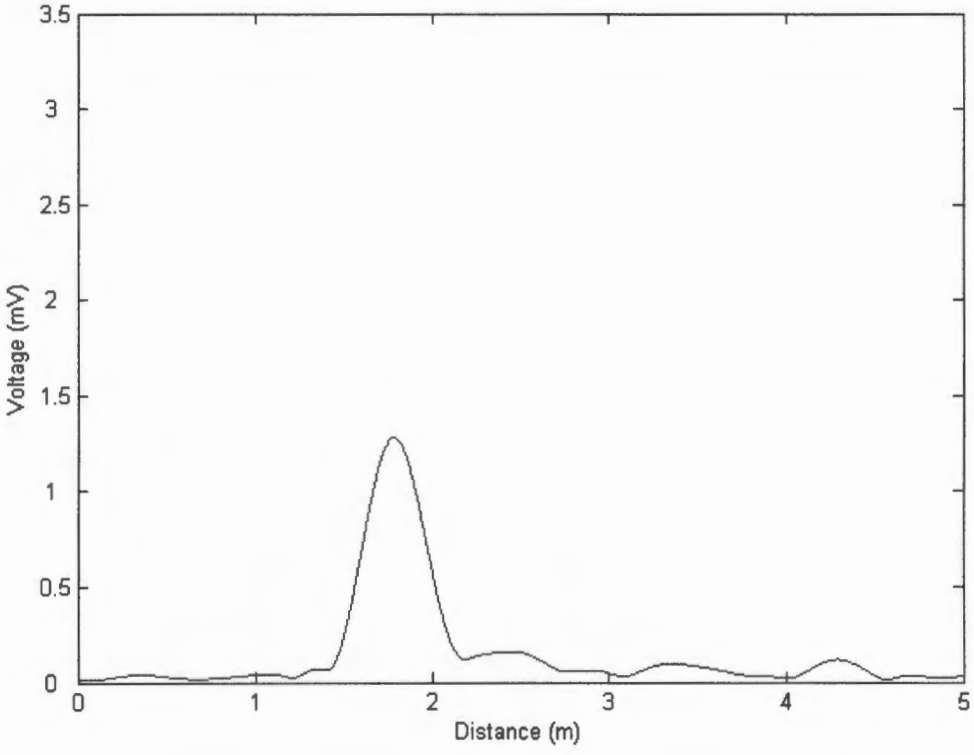


Figure 7.9: Target at 2.0m with RF amplifier.

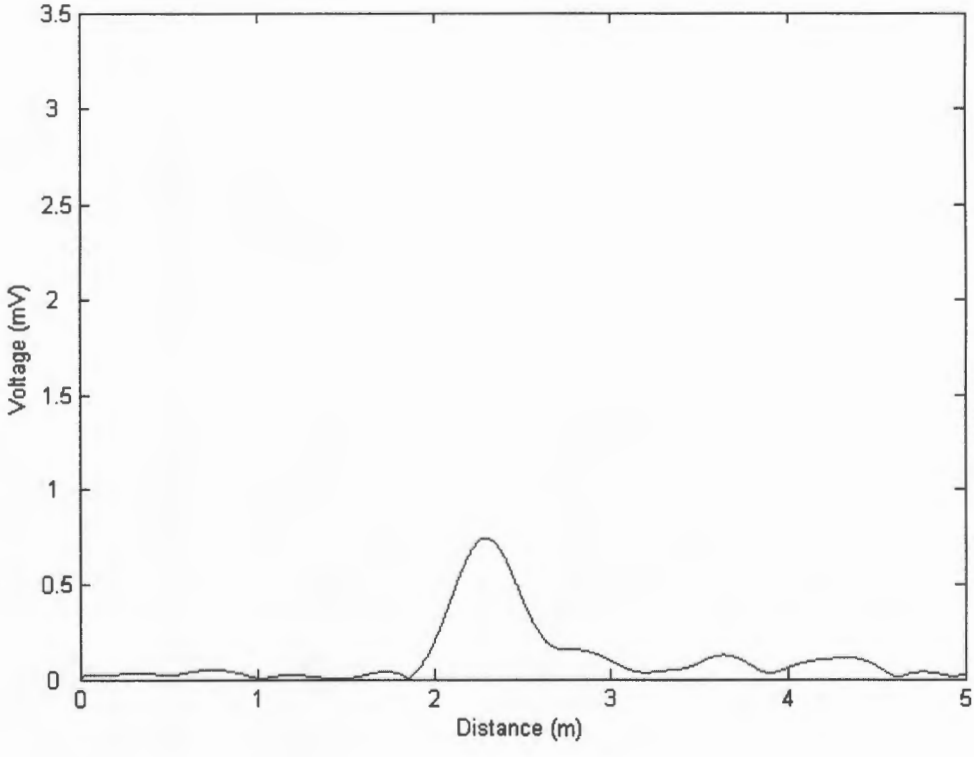


Figure 7.10: Target at 2.5m with RF amplifier.

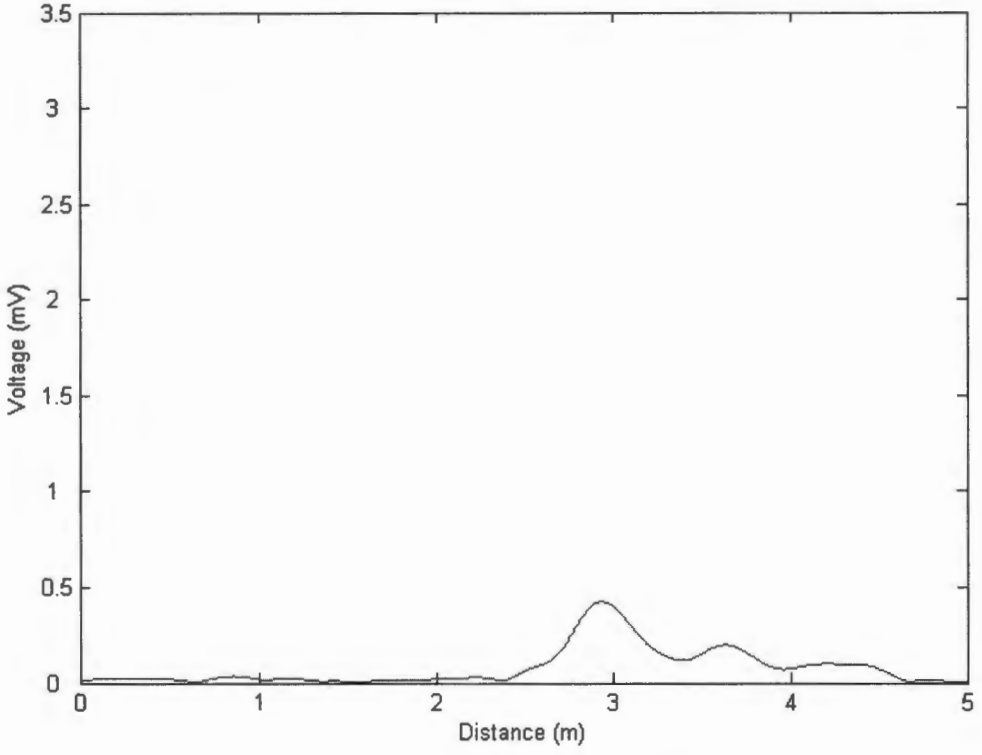


Figure 7.11: Target at 3.0m with RF amplifier.

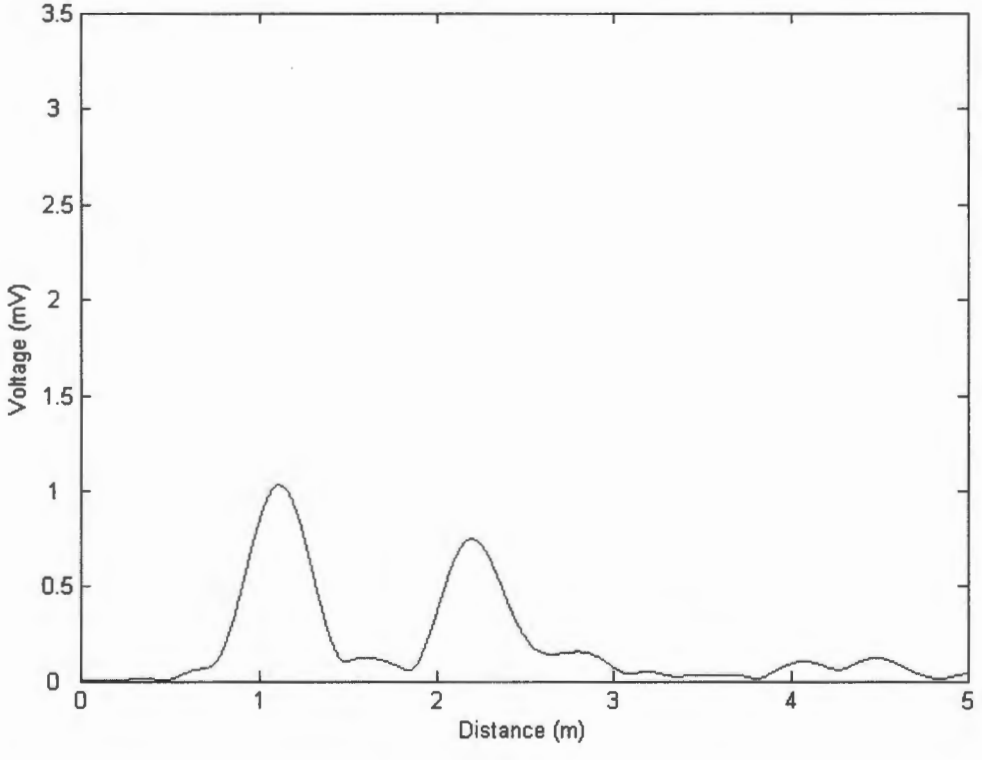


Figure 7.12: Targets at 1.0m and 2.5m with RF amplifier.

### 7.8.1 Detection through Wooden Partition

After point-target filter-snapshot is taken, a partition with dimensions 120cm (W) * 2cm (B) * 180cm (H) was placed 1.0m in front of the antenna, shown in Figure 7.13. Afterwards, a background snapshot was taken again with the partition in it thus includes the effect of the partition. Since now the partition is part of the background, it won't be shown on the down-range profile anymore.

The following down-range profiles were taken with a "Small Grid" as the target in the scene. Figure 7.14 shows a target 50cm behind the partition, which is 1.5m from the antennas. Figure 7.15, 7.16, and 7.17 show the target at 2.0m, 2.5m, and 3.0m.

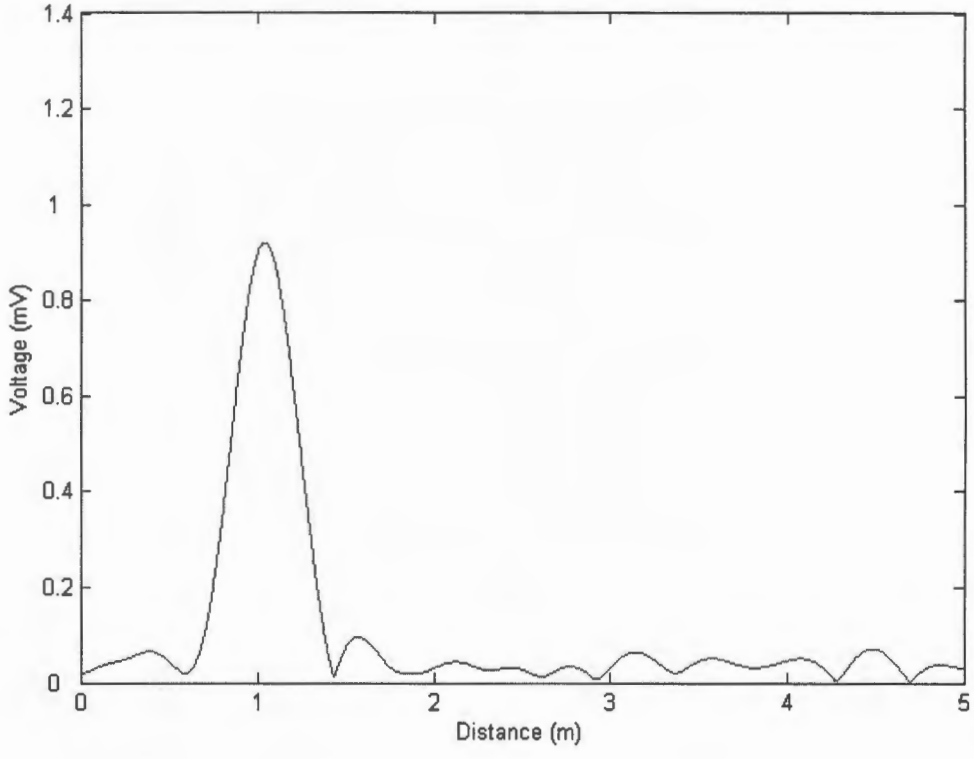


Figure 7.13: Partition at 1.0m.

The signal levels from these targets has been decreased due to the partition placed in the scene. By comparing peak values from down-range profiles in section 7.7.2 at different ranges and peak values shown in the down-range profiles in this section, the decrease percentage is tabulated in Table 7.2.

| Range (m) | Peak Volt w/o Partition $v_1$ (mV) | Peak Volt w/ Partition $v_2$ (mV) | Ratio $\frac{v_2}{v_1}$ (%) |
|---|---|---|---|
| 1.5 | 1.35 | 1.26 | 93.1 |
| 2.0 | 1.28 | 0.801 | 62.5 |
| 2.5 | 0.747 | 0.704 | 94.3 |
| 3.0 | 0.425 | 0.338 | 79.5 |

Table 7.2: Decrease due to the placement of the partition.

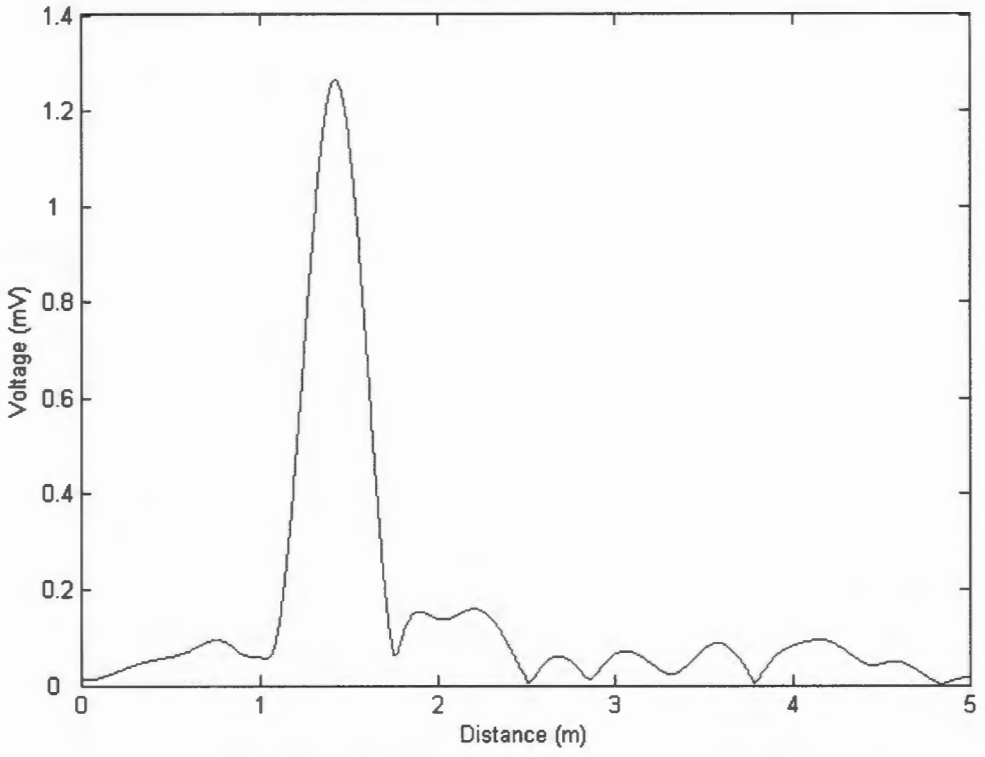


Figure 7.14: Target at 1.5m. (The partition located at 1.0m is not visible after background subtraction.)

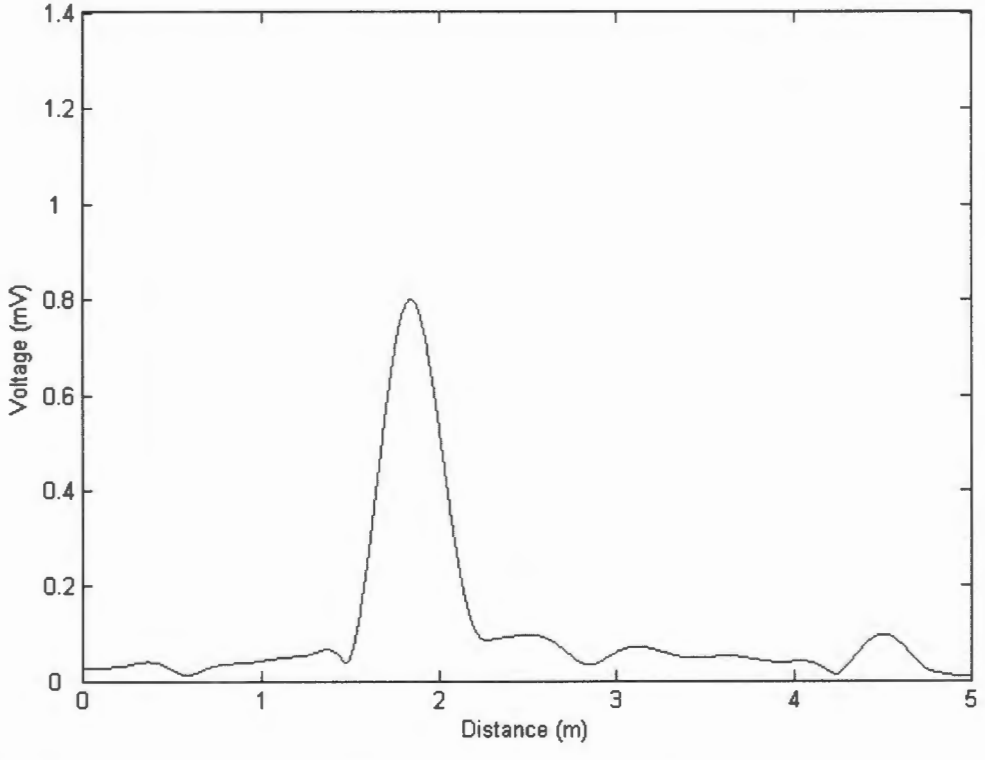


Figure 7.15: Target at 2.0m. (The partition located at 1.0m is not visible after background subtraction.)

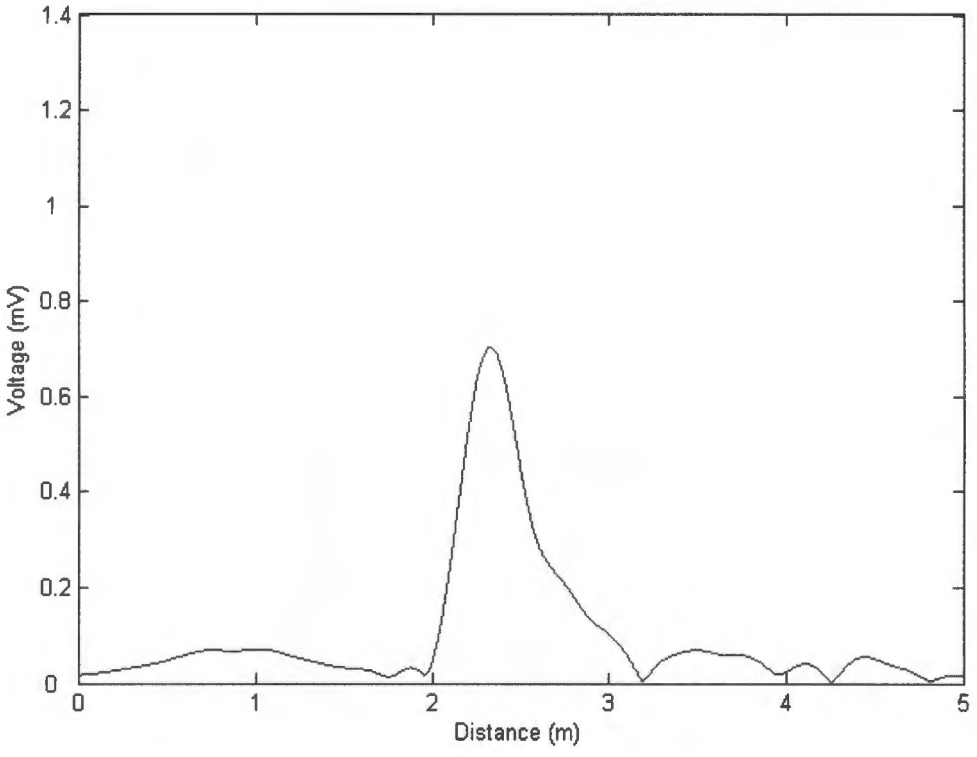


Figure 7.16: Target at 2.5m. (The partition located at 1.0m is not visible after background subtraction.)

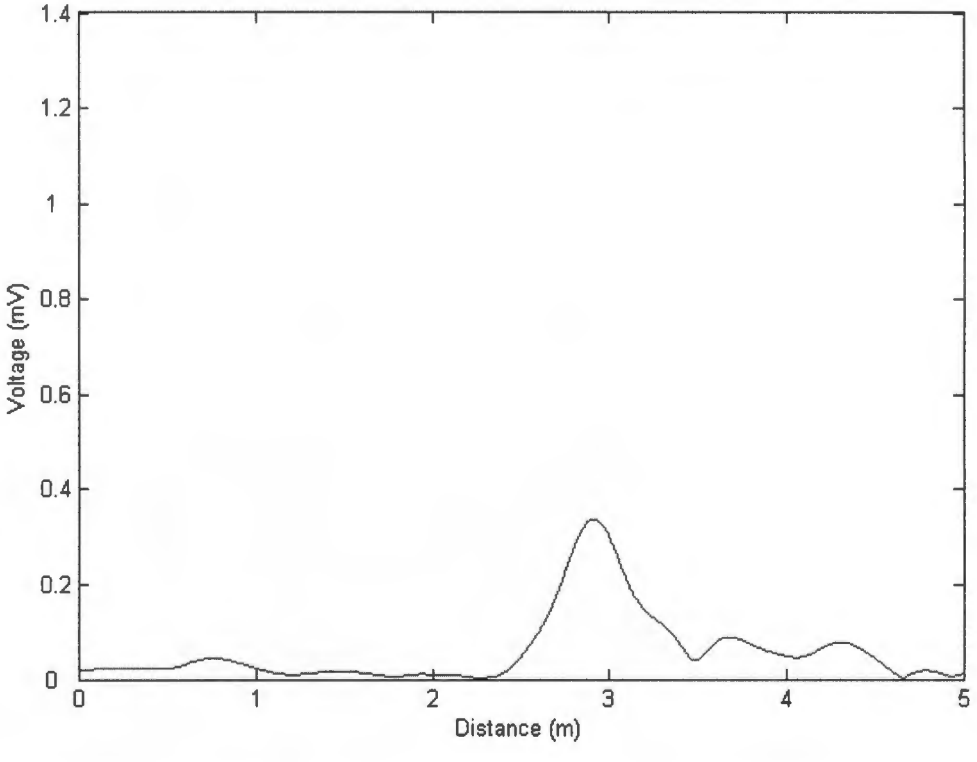


Figure 7.17: Target at 3.0m. (The partition located at 1.0m is not visible after background subtraction.)

This decrease is due to the attenuation introduced by the partition. The ratio is not a constant value due to inaccurate measurements.

### 7.8.2 Detection through Cement Wall

To achieve through-wall detection, a procedure similar to section 7.8.1 was carried out, the only difference being that instead of placing a wooden partition in front of the antennas, the antennas were mounted against a cement wall 9" (23cm) thick to detect movements in the adjacent room. In this instance the "Large Grid" target was used. It was observed that through wall attenuation was significantly higher than for the previously described case of the wooden partition. Targets were only visible next to the 9" wall. It is expected that with increased transmitted power, a useful range of several metres should be possible. The non portability of the present prototype prevented further tests on different walls.

## 7.9 Noise Performance

There are different sources of the noise in the system:

1. Thermal noise from the scene.
2. Thermal noise induced by the front-end RF amplifier.
3. Thermal noise induced by the post-sampler amplifier.
4. Residual background clutter due to drifts in the timing circuit.
5. A/D quantization error.

With no target in the scene, 10 down-range profiles were captured and their highest RMS value is 4.2807$\mu$V which is the highest noise power from the combination of all the above sources. Using measurements presented in section 7.7.2, the complete-system's worst signal-to-noise ratios can be estimated at different ranges with targets at those ranges. Table 7.3 tabulates results from ranges of 1.0, 1.5, 2.0, 2.5, 3.0 metres.

| Range (m) | Noise $n$ ($\mu$V) | Signal $v$ (mV) | SNR=$10log_{10}\frac{v^2}{n^2}$ (dB) |
|---|---|---|---|
| 1.0 | 4.28 | 3.28 | 57.7 |
| 1.5 | 4.28 | 1.35 | 50.0 |
| 2.0 | 4.28 | 1.28 | 49.5 |
| 2.5 | 4.28 | 0.747 | 44.8 |
| 3.0 | 4.28 | 0.425 | 39.9 |

Table 7.3: Signal-to-Noise ratio at different ranges.

Item 4 is mainly because of the capacitance variation due to temperature change of the MV104 varicap diode discussed in section 4.4. Its diode capacitance temperature coefficient is 280ppm/°C, thus if the ambient temperature changes in the range of ±5°C ($\Delta c = 10$°C) during the course of the experiment, then the delay generated by the delay line may drift up to 0.28%, i.e. 14 samples, or 0.22ns, or 3cm. This and the fact that the background snapshot's magnitude is significantly larger than those of the returned echoes (comparing Figure 6.3 and 6.5) results in residual background clutter in the down-range profiles.

## 7.10 Achievable Maximum Sweeping Rate and Maximum Speed Detectable

The maximum sweeping rate achievable $f_{max}$ is related to various factors:

- Nyquist criterion - the highest frequency component $f_H$ of the band of interest determines the size of range bin cell of the system is $R_\phi = \frac{c}{2f_H}$.
- Some limitations are imposed by the operational conditions, e.g. maximum unambiguous range $R_{max}$, pulse-repetition-frequency $PRF$, maximum/desirable detectable range $R_\delta$, minimum number of range bins $N$ according to Nyquist theorem.
- Some limitations are imposed by the circuitry (component-bounded), e.g. largest of the various time constants mentioned in Chapter 4 $\Gamma = \max\{\tau_1, \tau_2, \cdots\}$. They are active charge time $\tau_{Charge} = 10ms$, and passive discharge time $\tau_{Discharge} = 1ms$ of the fast sampler-averager mentioned in section 4.4, and cut-off frequency $f_c = 160Hz$ of the post-sampler amplifier mentioned in section 4.5.
- Some limitations are imposed by the hardware design, e.g. maximum delay-line range achievable.
- Some limitations are bounded by the hardware modules that interconnects the operational blocks of the system, i.e. NI-DAQ's maximum samples/second $S_{max}$, 12-bit maximum resolution, and hardware drivers.
- Some limitations are imposed by the software (programming-bounded), e.g. maximum refresh rate of the display loop $\sigma_{max}$ combined with the blocking call to capture data.

A typical scenario is as follows:

- The highest frequency component $f_H = 2.0GHz \Rightarrow R_\phi = \frac{c}{2f_H} = 7.5cm$ per range bin.

- $f_{PRF} = 2.0MHz \Rightarrow R_{max} = \frac{ct_{PRI}}{2} = \frac{c}{2} * \frac{1}{f_{PRF}} = 75m.$
- Maximum detectable range $R_\delta = 5m \Rightarrow N = \frac{R_\delta}{R_\phi} = 67$ range bins.

Since $\tau_{Charge} > \tau_{Discharge}$, using the worst case estimate, we would have to assume that at each range bin's position, the single-ended integrating samplers need at least $\Gamma = \tau_{Charge} = 10ms$ to reach $\approx 63\%$ of the steady state; for $N = 67$ range bins, it needs $\Gamma * N = 0.5s$ per sweep. This means DC voltages at the output terminals of the fast sampler-average are changing at a maximum rate of 67 levels per 0.5 second which is equivalent to say that $f_{DC} = 134Hz$. Since $f_{DC} \leq f_c$, the maximum sweeping rate $f_{max} = 2Hz$ in this case. If the target is moving, the maximum speed it travels at without introducing aliasing can be determined by calculating $f_{max} * R_\phi = 0.15m/s$.

If all conditions stand, except the desired detectable range is now $2.5m$, then the number of range bins are halved. One quickly concludes that the maximum sweeping rate $f_{max}$ is now $4Hz$ without examining all limitations. In this case, because $f_c = 160Hz$, the DC voltage can only change at a rate up to 160 levels per second without being distorted, the maximum sweeping rate is $3.2Hz$ imposed by the low-pass filters deployed at the input terminals of the post-sampler amplifier. Thus the maximum speed detectable in this case is $0.24m/s$.

# Chapter 8

# Conclusions and Future Work

This dissertation presented the design and implementation of a UWB Short-Range radar with result showing its performance for short range object detection. It has also provided a literature survey for UWB radar technology, discussion of the signal processing techniques utilized, and design of the graphical user interface.

Judging from the outcomes of the experiments conducted, UWB-pulse technology is a promising candidate for short-range radar applications because of its simplicity, low-cost and good performance. It is also evidential that a miniature circuit design is possible because of the low component count, and the use of digital hardware. Furthermore, it has the advantage of having a low probability of interception and detection if the master clock is jittered.

Future work should include

- implementation of a portable battery powered version for use with a laptop.
- improvement of detection range and range resolution:
  - the transmitter stage could be improved to provide increased peak power, and a narrower pulse.
  - the existing front-end RF amplifier should be replaced by broader bandwidth, low noise, high gain amplifier designed for pulse amplification (having a flatter response across the band of interest.
- development of a multi-channel receiver to allow experimentation with an antenna array.
- development of suitable broadband antennas, and particularly to be used in a broadband array.
- development of software/algorithms to produce 2-D and 3-D images from array data.
- testing of array-based imaging capability in applications like through wall imaging.

# Appendix A

# Software Source Code

The following is an excerpt from the MATLAB source code responsible for the displaying loop. It triggers simultaneous I/O of the NI-DAQ card to capture the data and process the captured data accordingly to display the down-range profiles in real-time.

Program A.1: localShowData.m

```
% --- Executes while startButton is activated.
function localShowData(hObject,event)
handles = get(hObject,'UserData');
putdata(handles.ao, [handles.y']);
start(handles.ai);
start(handles.ao);
trigger(handles.ao);
data = getdata(handles.ai);
Q = round(400/25);
L = round(str2double(get(handles.edit2,'String'))/Q);
M = round(str2double(get(handles.edit3,'String'))/Q);

Nx = length(data);
data(Nx+1:2*Nx) = 0;
handles.background(Nx+1:2*Nx) = 0;
handles.filter(Nx+1:2*Nx) = 0;
Nx = length(data);
L = 2 * L;
M = 2 * M;

V_Max = str2double(get(handles.V_Max_Value,'String'));
V_Min = str2double(get(handles.V_Min_Value,'String'));
contents = get(handles.modeMenu,'String');
switch contents{get(handles.modeMenu,'Value')}
    case 'Raw'
        data = data;
        plot(handles.profile1, data);
        V = axis(handles.profile1); axis(handles.profile1, [V(1) Nx
            /2 V_Min V_Max]);
        plot(handles.profile2, abs(fft(data)));
        V = axis(handles.profile2); axis(handles.profile2, [round(L
            -20) round(M+20) 0 V(4)]);
        % V = axis(handles.profile2); axis(handles.profile2, [V(1)
            Nx/2 0 V(4)]);

    case 'Background Snapshot'
        data = handles.background;
        plot(handles.profile1, data);
        V = axis(handles.profile1); axis(handles.profile1, [V(1) Nx
            /2 V_Min V_Max]);
```

```
37          plot(handles.profile2, abs(fft(data)));
38          V = axis(handles.profile2); axis(handles.profile2, [round(L
                -20) round(M+20) 0 V(4)]);
39          % V = axis(handles.profile2); axis(handles.profile2, [V(1)
                Nx/2 V(3) V(4)]);
40
41      case 'Difference'
42          data = data - handles.background;
43          plot(handles.profile1, data);
44          V = axis(handles.profile1); axis(handles.profile1, [V(1) Nx
                /2 V_Min V_Max]);
45          plot(handles.profile2, abs(fft(data)));
46          V = axis(handles.profile2); axis(handles.profile2, [round(L
                -20) round(M+20) 0 V(4)]);
47          % V = axis(handles.profile2); axis(handles.profile2, [V(1)
                Nx/2/5 V(3) V(4)]);
48
49      case 'Filter Snapshot'
50          data = handles.filter;
51          plot(handles.profile1, data);
52          V = axis(handles.profile1); axis(handles.profile1, [V(1) Nx
                /2 V_Min V_Max]);
53          plot(handles.profile2, abs(fft(data)));
54          V = axis(handles.profile2); axis(handles.profile2, [V(1) Nx
                /2 V(3) V(4)]);
55
56      case 'Matched'
57          data = data - handles.background;
58          DATA = fft(data);
59          FILTER = fft(handles.filter);
60          DATA(1:L) = 0;
61          DATA(M+1:Nx)= 0;
62          FILTER(1:L) = 0;
63          FILTER(M+1:Nx)= 0;
64          FILTER=FILTER/sum(sqrt(abs(FILTER).^2));
65          wBox = get(handles.windowBox,'String');
66          switch wBox{get(handles.windowBox,'Value')}
67              case 'Hanning'
68                  DATA(L+1:M) = DATA(L+1:M).*hann(M-L);
69              case 'Hamming'
70                  DATA(L+1:M) = DATA(L+1:M).*hamming(M-L);
71              case 'Blackman'
72                  DATA(L+1:M) = DATA(L+1:M).*blackman(M-L);
73          end
74          data = ifft(DATA.*conj(FILTER));
75          data = circshift(data, handles.Fstart);
76          plot(handles.profile1, abs(data));
77          V = axis(handles.profile1); axis(handles.profile1, [V(1) Nx
                /2 V_Min V_Max]);
78          plot(handles.profile2, abs(fft(data)));
79          V = axis(handles.profile2); axis(handles.profile2, [round(L
                -20) round(M+20) 0 V(4)]);
80          data = abs(data);
81
82      case 'Deconvolved'
83          data = data - handles.background;
84          DATA = fft(data);
85          FILTER = fft(handles.filter);
86          FILTER = 1./FILTER;
87          DATA(1:L) = 0;
88          DATA(M+1:Nx)= 0;
89          FILTER(1:L) = 0;
90          FILTER(M+1:Nx)= 0;
91          FILTER=FILTER/sum(sqrt(abs(FILTER).^2));
92          wBox = get(handles.windowBox,'String');
```

```
93          switch wBox{get(handles.windowBox,'Value')}
94              case 'Hanning'
95                  DATA(L+1:M) = DATA(L+1:M).*hann(M-L);
96              case 'Hamming'
97                  DATA(L+1:M) = DATA(L+1:M).*hamming(M-L);
98              case 'Blackman'
99                  DATA(L+1:M) = DATA(L+1:M).*blackman(M-L);
100         end
101         data = ifft(DATA.*FILTER);
102         data = circshift(data, handles.Fstart);
103         plot(handles.profile1, abs(data));
104         V = axis(handles.profile1); axis(handles.profile1, [V(1) Nx
                /2 V_Min V_Max]);
105         plot(handles.profile2, abs(fft(data)));
106         V = axis(handles.profile2); axis(handles.profile2, [round(L
                -20) round(M+20) 0 V(4)]);
107         data = abs(data);
108     case 'Envelope'
109         data = data - handles.background;
110         DATA = fft(data);
111         DATA(Nx/2+1:Nx) = 0;
112         wBox = get(handles.windowBox,'String');
113         switch wBox{get(handles.windowBox,'Value')}
114             case 'Hanning'
115                 DATA(L+1:M) = DATA(L+1:M).*hann(M-L);
116             case 'Hamming'
117                 DATA(L+1:M) = DATA(L+1:M).*hamming(M-L);
118             case 'Blackman'
119                 DATA(L+1:M) = DATA(L+1:M).*blackman(M-L);
120         end
121         data = ifft(DATA);
122
123         plot(handles.profile1, abs(data));
124         V = axis(handles.profile1); axis(handles.profile1, [V(1) Nx
                /2 V_Min V_Max]);
125         plot(handles.profile2, abs(fft(data)));
126         V = axis(handles.profile2); axis(handles.profile2, [round(L
                -20) round(M+20) 0 V(4)]);
127         % V = axis(handles.profile2); axis(handles.profile2, [V(1)
                Nx/2 V(3) V(4)]);
128         data = abs(data);
129 end
130
131 cheese = get(handles.say_cheese,'Value');
132 if (cheese == 1)
133     set(handles.say_cheese,'Value',0);
134     AxesRect = get(handles.profile1,'position');
135     figure;
136     plot(data);
137     V = axis(); axis([V(1) Nx/2 V(3) V(4)]);
138 end
```

# Bibliography


[1] Micropower impulse radar. *Science & Technology Review*, pages 16–27, January/February 1996.

[2] Analog Devices, Inc. *AD620 Low Cost, Low Power, Instrumentation Amplifier*, rev. e edition, 1999.

[3] L. Astanin and A. Kostylev. *Ultrawideband Radar Measurements: Analysis and Processing (Radar, Sonar, Navigation and Avionics Series)*. Institution of Electrical Engineers, 1997.

[4] T. W. Barrett. Performance prediction and modeling. In J. D. Taylor, editor, *INTRODUCTION TO ULTRA-WIDEBAND RADAR SYSTEMS*, chapter 12, pages 609–656. CRC Press, Inc, 1995.

[5] M. Birch. Development of a cavity backed bowtie antenna with dielectric matching for ground penetrating radar. Master's thesis, University of Stellenbosch, September 2001.

[6] T. Carlberg. Analysis of uwb (ultra wideband) for indoor geolocation. Master's thesis, Chalmers University of Technology, 2000.

[7] Y.-M. A. Chang and A. J. Wilkinson. Investigation of uwb-pulse technology for short-range radar applications. Technical report, University of Cape Town, September 2005.

[8] J. Collins. Hospital gets ultra-wideband rfid. *RFID Journal*, August 2004.

[9] Ellies. *Grid Aerial.*

[10] Ellies. *Grid Aerial Red / Yellow.*

[11] Ellies. *Small Grid Aerial.*

[12] FCC. First report and order: In the matter of revision of part 15 of the commission's rules regarding ultra-wideband transmission systems. Technical Report 02-48, April 2002.

[13] B. C. Flores and J. Reberto Vasquez. Compression of wideband returns from overspread targets. In J. D. Taylor, editor, *ULTRA-WIDEBAND RADAR TECHNOLOGY*, chapter 5, pages 135–153. CRC Press LLC, 2001.

[14] P. R. Foster, J. D. Halsey, and M. G. M. Hussain. Ultra-wideband antenna technology. In J. D. Taylor, editor, *INTRODUCTION TO ULTRA-WIDEBAND RADAR SYSTEMS*, chapter 5, pages 145–286. CRC Press, Inc, 1995.

[15] L. Fullerton. Time domain radio transmission system. US Patent, 1990. US Patent 4979186.

[16] A.-L. Germond, E. Pottier, and J. Saillard. Bistatic radar polarimetry theory. In J. D. Taylor, editor, *ULTRA-WIDEBAND RADAR TECHNOLOGY*, chapter 14, pages 379–414. CRC Press LLC, 2001.

[17] J. F. M. Gerrits, A. A. Hutter, J. Ayadi, and J. R. farserotu. Modelling and simulation of a dipole antenna for uwb applications using equivalent spice circuits. In *IEEE IWUWBS*, 2003.

[18] G. S. Gill. Fourier series-based waveform generation and signal processing in uwb radar. In J. D. Taylor, editor, *ULTRA-WIDEBAND RADAR TECHNOLOGY*, chapter 10, pages 291–302. CRC Press LLC, 2001.

[19] G. S. Gill. High-resolution step-frequency radar. In J. D. Taylor, editor, *ULTRA-WIDEBAND RADAR TECHNOLOGY*, chapter 11, pages 303–328. CRC Press LLC, 2001.

[20] H. F. Harmuth. Transmitter signature and target signature of radar signals. In J. D. Taylor, editor, *INTRODUCTION TO ULTRA-WIDEBAND RADAR SYSTEMS*, chapter 8, pages 435–456. CRC Press, Inc, 1995.

[21] J. Harold F. Engler. Technical issues in ultra-wideband radar systems. In J. D. Taylor, editor, *INTRODUCTION TO ULTRA-WIDEBAND RADAR SYSTEMS*, chapter 2, pages 11–50. CRC Press, Inc, 1995.

[22] I. I. Immoreev. Improved signal detection in uwb radars. In J. D. Taylor, editor, *ULTRA-WIDEBAND RADAR TECHNOLOGY*, chapter 2, pages 21–46. CRC Press LLC, 2001.

[23] I. I. Immoreev. Main features of uwb radars and differences from common narrowband radars. In J. D. Taylor, editor, *ULTRA-WIDEBAND RADAR TECHNOLOGY*, chapter 1, pages 1–19. CRC Press LLC, 2001.

[24] I. I. Immoreev and D. V. Fedotov. Ultra wideband radar systems: Advantages and disadvantages. In *IEEE Conference on Ultra Wideband Systems and Technologies*. IEEE, 2002.

[25] R. B. James and J. B. Mendola. Ultra-wideband technology for intelligent transport systems. In J. D. Taylor, editor, *ULTRA-WIDEBAND RADAR TECHNOLOGY*, chapter 7, pages 165–179. CRC Press LLC, 2001.

[26] A. F. Kardo-Sysoev. New power semiconductor devices for generation of nano- and subnanosecond pulses. In J. D. Taylor, editor, *ULTRA-WIDEBAND RADAR TECHNOLOGY*, chapter 9, pages 205–290. CRC Press LLC, 2001.

[27] S. Kingsley and S. Quegan. *UNDERSTANDING RADAR SYSTEMS*. SciTech Publishing, Inc., 1999.

[28] LTC. *SwitcherCAD III*. Linear Technology Corporation, 2005.

[29] V. Z. Marmarelis, D. Sheby, E. C. Kisenwether, and T. A. Erdley. High-order signal processing for ultra-wideband radar signals. In J. D. Taylor, editor, *INTRODUCTION TO ULTRA-WIDEBAND RADAR SYSTEMS*, chapter 11, pages 579–608. CRC Press, Inc, 1995.

[30] T. McEwan. Uwb radar motion sensor. US Patent, 1994. US Patent 5361070.

[31] N. J. Mohamed. High-resolution ultra-wideband radars. In J. D. Taylor, editor, *ULTRA-WIDEBAND RADAR TECHNOLOGY*, chapter 3, pages 47–74. CRC Press LLC, 2001.

[32] J. Mosquera and M. Isasa. Uwb resistively loaded sensor design. In *IGARSS*, volume 7, pages 4232 – 4234. IEEE, July 2003.

[33] R. M. Narayanan, Y. Xu, P. D. Hoffmeyer, and J. O. Curtis. Design, performance, and applicaitons of a coherent uwb random noise radar. In J. D. Taylor, editor, *ULTRA-WIDEBAND RADAR TECHNOLOGY*, chapter 8, pages 181–203. CRC Press LLC, 2001.

[34] W. C. Nunnally, R. N. Edwards, and D. V. Giri. Direct radiating systems. In J. D. Taylor, editor, *INTRODUCTION TO ULTRA-WIDEBAND RADAR SYSTEMS*, chapter 6, pages 287–324. CRC Press, Inc, 1995.

[35] D. Platts, O. S. F. Zucker, and I. A. McIntyre. Transmitters. In J. D. Taylor, editor, *INTRODUCTION TO ULTRA-WIDEBAND RADAR SYSTEMS*, chapter 4, pages 109–144. CRC Press, Inc, 1995.

[36] M. Rangaswamy and T. K. Sarkar. Analytical techniques for ultra-wideband signals. In J. D. Tylor, editor, *INTRODUCTION TO ULTRA-WIDEBAND RADAR SYSTEMS*, chapter 3, pages 51–108. CRC Press, Inc, 1995.

[37] R. Roussel-Dupre' and T. W. Barrett. Propagation and energy transfer. In J. D. Taylor, editor, *INTRODUCTION TO ULTRA-WIDEBAND RADAR SYSTEMS*, chapter 7, pages 325–434. CRC Press, Inc, 1995.

[38] J. Sachs, M. Rossberg, P. Rauschenbach, P. Peyerl, and J. Friedrich. Integrated uwb radar circuit for base band applications from dc to 5 GHz. In *German Radar Symposium GRS*, pages 231–236, Berlin, Germany, October 2000.

[39] T. Sakamoto and T. Sato. An estimation algorithm of target location and scattered waveforms for uwb pulse radar systems. *IEICE Transactions on Communications*, E87-B(6):(in press), 2004.

[40] T. Sakamoto and T. Sato. A target shape estimation algorithm for pulse radar systems based on boundary scattering transform. *IEICE Transactions on Communications*, E87-B(5):1357–1365, 2004.

[41] H. G. Schantz. A brief history of uwb antennas. In *IEEE UWBST*, 2003.

[42] H. G. Schantz. Introduction to uwb antennas. In *IEEE UWBST*, 2003.

[43] H. G. Schantz. Uwb magnetic antennas. In *IEEE APS/URSI*, 2003.

[44] C. E. Shannon. A mathematical theory of communication. *Bell System Technical Journal*, 27:379–423,623–656, July, October 1948.

[45] L. N. Shuuya. Design and construction of a twin bowtie antenna for the frequency range 1-2 gigahertz. October 2004.

[46] K. Siwiak. Ultra-wide band radio: Introducing a new technology. *IEEE VTS 53rd*, 2, 2001.

[47] E. M. Staderini. Everything you always wanted to know about uwb radar: a practical introduction to the ultra wideband technology. *OSEE (Online Symposium for Electronics Engineers)*, December 2001.

[48] F. G. Stremler. *Introduction to Communication Systems*. Prentice Hall, 3rd edition, 1990.

[49] J. D. Taylor, editor. *Introduction to Ultra-Wideband Radar Systems*. CRC Press LLC, 1995.

[50] J. D. Taylor. Ultra-wideband radar overview. In J. D. Taylor, editor, *INTRODUCTION TO ULTRA-WIDEBAND RADAR SYSTEMS*, chapter 1, pages 1–10. CRC Press, Inc, 1995.

[51] J. D. Taylor. Ultra-wideband radar capactity demonstrations. In J. D. Taylor, editor, *ULTRA-WIDEBAND RADAR TECHNOLOGY*, chapter 13, pages 343–377. CRC Press LLC, 2001.

[52] J. D. Taylor. Ultra-wideband radar receivers. In J. D. Taylor, editor, *ULTRA-WIDEBAND RADAR TECHNOLOGY*, chapter 4, pages 75–133. CRC Press LLC, 2001.

[53] J. D. Taylor, editor. *Ultra-wideband Radar Technology*. CRC Press LLC, 2001.

[54] J. D. Taylor and E. C. Kisenwether. Ultra-wideband radar receivers. In J. D. Taylor, editor, *INTRODUCTION TO ULTRA-WIDEBAND RADAR SYSTEMS*, chapter 10, pages 491–578. CRC Press, Inc, 1995.

[55] J. D. Taylor and T. E. McEwan. The micropower impulse radar. In J. D. Taylor, editor, *ULTRA-WIDEBAND RADAR TECHNOLOGY*, chapter 6, pages 155–164. CRC Press LLC, 2001.

[56] Time Domain Corporation. *RadarVision2i: Introducing the Second Generation Through-Wall Motion Detection Radar for Enhanced Tactical Entry.*

[57] L. Ulander, H. Hellsten, and J. D. Taylor. The carabas ii vhf synthetic aperture radar. In J. D. Taylor, editor, *ULTRA-WIDEBAND RADAR TECHNOLOGY*, chapter 12, pages 329–342. CRC Press LLC, 2001.

[58] M. L. VanBlaricum. Radar cross section and target scattering. In J. D. Taylor, editor, *INTRODUCTION TO ULTRA-WIDEBAND RADAR SYSTEMS*, chapter 9, pages 457–490. CRC Press, Inc, 1995.

[59] A. J. Wilkinson. Design, construction and performance of a microwave radiometer. November 1989.

[60] A. J. Wilkinson. Notes on radar signal processing: Fundamentals, June 2002.

[61] A. J. Wilkinson and Y.-M. A. Chang. Proposal: Investigation of uwb-pulse technology for short-range radar applications, February 2004.